

# Latest Progress on Photoabsorbent Materials for Multifunctional Semitransparent Organic Solar Cells

Gururaj P. Kini, SungJae Jeon, and Doo Kyung Moon\*

Semi-transparent organic solar cells (ST-OSCs) have revolutionized the field of photovoltaics (PVs) due to their unique abilities, such as transparency and color tunability, and have transformed normal power-harvesting OSC devices into multifunctional devices, such as building-integrated photovoltaics, agrivoltaics, floating photovoltaics, and wearable electronics. Very recently, ST-OSCs have seen remarkable progress, with a rapid increase in power conversion efficiency from below 7% to 12–14%, with an average visible transparency of 9–25%, especially due to the use of low bandgap semiconductors including polymer donors and non-fullerene acceptors that exhibit absorption in the near-infrared region as photoabsorbent materials. From this perspective, the latest developments in ST-OSCs stemming from the innovations in photovoltaic materials that delivered multifunctional ST-OSCs with top-of-the-line power conversion efficiencies are discussed to shed light on the structure-property relationship between molecular design and current challenges in this cutting-edge research field. Finally, personal perspectives, including research directions for the future use of ST-OSCs in multifunctional applications, are also proposed.

## 1. Introduction

Global demand for clean and sustainable energy has grown exponentially due to the rapid rate of urbanization and industrialization and changes in the lifestyle of people all over the world. Among the various renewable energy resources explored so far, solar energy has emerged as the most promising candidate to replace existing non-renewable fossil fuels because of its environmentally friendly nature, abundance and sustainability. Presently, silicon-based inorganic solar cells dominate the global photovoltaic (PV) market because of their high-power conversion efficiency (PCE) of over 25% and reasonable stability. However, intrinsic drawbacks of these materials, such as high production cost, low mechanical flexibility and bandgap

tunability, and unaesthetic nature have triggered a search for practical replacements.<sup>[1]</sup> The emergence of organic solar cells (OSCs) offers solutions to the above-mentioned issues. OSCs have various benefits: they are inexpensive, processable in solution, flexible, semi-transparent, lightweight, and suitable for large-scale roll-to-roll processing.<sup>[1–9]</sup> Moreover, they also produced noteworthy PCEs of up to 18% for single-junction and tandem devices because of synergistic progress in active layer components, device architecture, and morphology controlling that has been made over the last decade.<sup>[8,10–18]</sup>


Besides traditional solar cells for power generation, the development of resources to create more efficient living/working spaces is gaining popularity in both the scientific and industrial communities due to the diverse functionalities of such devices in self-powered buildings or electronic appliances. In particular, building-

integrated photovoltaics (BIPVs), which can utilize the large surface areas of windows, roofs, sidewalls and facades in modern urban environments to produce power-generating solar windows, and are considered one of the key business markets for future OSCs.<sup>[19–23]</sup> Typically, active layer materials in OSCs are comprised of thin films (thickness below 200 nm) due to the lower carrier mobility of these organic semiconducting materials compared to their traditional inorganic counterparts.<sup>[7]</sup> This unique property of OSCs inherently offers optical semi-transparency in these materials, leading to the revolution in PV technology by designing specially developed OSCs named “semitransparent organic solar cells” (ST-OSCs), which have both transparent electrodes in their device structure. ST-OSCs have a wide variety of applications, such as in BIPVs, car shelters, greenhouses,<sup>[24–27]</sup> automobile sunroof,<sup>[28]</sup> and wearable electronics,<sup>[29]</sup> thus turning normal OSCs into multifunctional power-harvesting units (Figure 1a-i). Furthermore, empowered by bandgap and optical engineering technologies, these ST-OSCs can also be used to produce colorful devices for aesthetically pleasing architectural applications,<sup>[27,30–34]</sup> heat insulation<sup>[35–38]</sup> and indoor functionality<sup>[39]</sup> via systematic tailoring of the active layer to absorb specific spectral ranges (ultraviolet (UV), visible, or near-infrared (NIR)) and light management methods.

A typical ST-OSC device configuration is presented in Figure 1j. It consists of a photoabsorbent blended layer of a p-type electron donor (ED) and an n-type electron acceptor (EA)

Dr. G. P. Kini, Dr. S. J. Jeon, Prof. D. K. Moon  
Nano and Information Materials (NIMs) Laboratory  
Department of Chemical Engineering  
Konkuk University  
120, Neungdong-ro, Gwangjin-gu, Seoul 05029, Korea  
E-mail: dkmoon@konkuk.ac.kr

Dr. S. J. Jeon  
Department of Academy of Applied Science and Technology  
Konkuk University  
120, Neungdong-ro, Gwangjin-gu, Seoul 05029, Korea

 The ORCID identification number(s) for the author(s) of this article can be found under <https://doi.org/10.1002/adfm.202007931>.

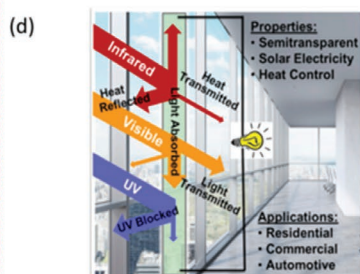
DOI: 10.1002/adfm.202007931

### Multifunctional applications of ST-OSCs

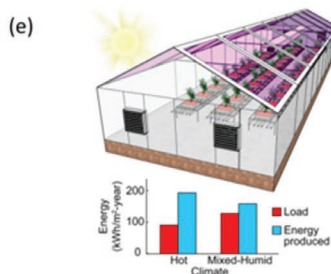
#### Building integrated photovoltaics (BIPVs)



#### Heat insulation



#### Agrivoltaics



#### Automobile sun-roof



#### Floating photovoltaics



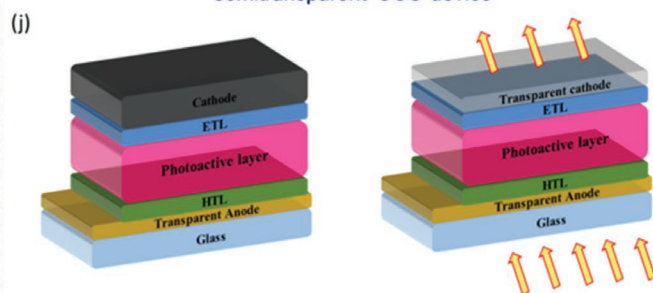
#### Wearable electronics



#### Flexible solar cells



#### Schematic of typical conventional and semitransparent-OSC device



#### AM 1.5 G solar emission spectrum

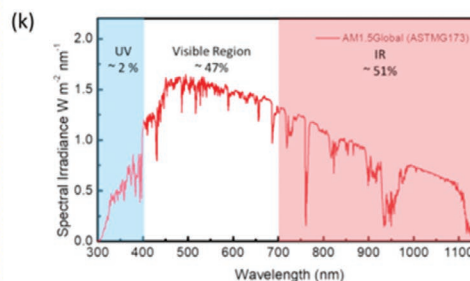


**Figure 1.** Potential applications of ST-OSCs: Building-integrated photovoltaics: a) Solaronix' multicolored transparent photovoltaic façade at the SwissTech convention center, EPFL, Switzerland. Photos courtesy of Solaronix, Switzerland, www.Solaronix.com; b) Skylight at the Lucia building at the University of Valladolid, Spain, allows for the natural lighting of the building while producing up to 5550 kWh per year. Photos courtesy of onyx solar, Ávila, Spain, www.onyx-solar.com and c) Artist design of the integration of flexible ST-OSCs in glass construction elements. Idea and image courtesy of ARMOR group, Nantes, France, www.armor-group.com; Heat insulation function: d) Schematic representation of ST-OSCs for power generation and heat-insulation application. Reproduced with permission.<sup>[38]</sup> Copyright 2018, Elsevier Inc.; Agrivoltaics: e) Illustration of ST-OSCs for the self-powered greenhouse to achieve net-zero energy greenhouses in warm and moderate climates. Reproduced with permission.<sup>[25]</sup> Copyright 2020, Elsevier Inc.; Sun-roof of automobiles: f) Schematic representation of ST-OSCs for the sun-roof windshield. adapted with permission.<sup>[28]</sup> Copyright 2020, Elsevier Inc; Floating photovoltaics: g) Representative image; ST-OSCs for wearable electronics: h) glass and watch and i) Flexible ST-OSCs; j) Device architecture of typical conventional and ST-OSCs and k) AM 1.5 Global solar emission spectrum and its energy proportion in different regions. Reproduced with permission.<sup>[41]</sup> Copyright 2020, Elsevier Inc.

which is sandwiched between a transparent bottom electrode (TBE) and a top electrode (TTE) and separated by a thin cathode and anode interfacial layer beneficial for effective charge separation and collection. The device architecture and material design of ST-OSCs differ slightly from those of well-developed OSCs in the following ways. First, in conventional OSCs, it is not possible to take advantage of the semi-transparency of the active layer material, since such devices are equipped with a non-transparent metal layer that serves as an electrode and helps to absorb more photons by doubling the optical path (acts as a mirror).<sup>[1]</sup> In contrast, in ST-OSCs, the metal layer is replaced with another transparent electrode, which enables good transmittance of incoming light and enables semitransparency. However, this causes an inevitable loss of short-circuit current density ( $J_{sc}$ ) and performance because only a small flux of the incident light is reflected by the BTE. Second, further changes in the device structure and/or active layer materials with enhanced absorption in the NIR region, are desirable as to effectively re-harvest photons that are lost in the absorption region from 370 to 740 nm in ST-OSC devices without affecting transmittance of visible light. Third, a trade-off between PCE and optical assessment factors, such as the average transmittance of the solar cells in the visible region (AVT), transparency color perception, corresponding color temperature (CCT) and color rendering index (CRI), is also essential to employ ST-OSCs for practical applications.<sup>[1]</sup> In principle, through synergistic modification of molecular design to synthesize active layer components and through device engineering (development of new TTEs with the appropriate work function and high conductivity and use of optical engineering technologies such as microcavities, photonic crystals, or antireflective device structures), the performance of ST-OSCs can be further improved.

In the early stages, the development of ST-OSCs was sluggish and they displayed inferior PCE values (<3%), mainly because of the use of wide bandgap (WBG, optical bandgap ( $E_g$ ) > 1.9 eV and  $E_g$  will be calculated from equation  $E_g = 1240/\lambda_{onset}$  eV, where  $\lambda_{onset}$  is UV–vis absorption onset of photovoltaic materials in thin film state) organic semiconductors (e.g., polymer donors (PDs) and fullerene acceptors (FAs)) as active layer materials, which can utilize photons only in the UV–visible region leading to difficulty in achieving a balance between PCE and AVT.<sup>[40]</sup> Later, as predicted from by Shockley–Queisser model, optical  $E_g$  around 1.36 eV (910 nm)–1.12 eV (1100 nm) is considered to be suitable to realize a higher tradeoff between PCE and AVT without affecting visible transparency.<sup>[42]</sup> Hence, synthesis and use of low or narrow bandgap (LBG or NBG,  $E_g < 1.6$  eV) PDs became a subject of interest; by employing these PDs in an active layer with FAs, PCEs were improved from 3% to 7%.<sup>[43–45]</sup> In 2017, NIR-absorbing non-fullerene or fused ring electron acceptors (NFAs or FREAs) created a new wave in OSCs.<sup>[46]</sup> Since then, significant efforts have been made to enhance the performance of ST-OSCs by incorporating both LBG PDs and NFAs or FREAs as the photoabsorbent layer, leading to remarkable PCEs of up to 14.1% in only 3 years via efficient extraction of photons in the NIR region.<sup>[31,47–50]</sup> Subsequently, it has become vital to gain insight into the role of these newly designed photoabsorbent materials in boosting the PCEs of ST-OSCs. Over the years, several review articles emphasizing various research trends in ST-OSCs, including the use of

transparent electrodes, device engineering, optical perceptions and free charge carrier generation and recombination losses, were reported.<sup>[1,7,42,51–53]</sup> However, to the best of our knowledge, there have been no articles that focus on the use of different photoabsorbent materials for ST-OSCs.

Given the remarkable advances in ST-OSCs, especially using LBG semiconductor materials as photoabsorbent layers, we believe it is time to review their developments. Thus, in this progress report, we focus on the development of photoabsorbent materials over the last 7 years that are designed to meet the requirements of solution-processable ST-OSCs. First, we discuss fullerene-based ST-OSCs including progress in the design of active layer components and their limitations through selected examples. Next, with an emphasis on modern NIR-absorbing FREAs with breakthrough performances, we summarize the design strategies for these FREAs, including the introduction of fused ring donor cores, increasing intramolecular charge transfer (ICT) via insertion of various electron-deficient acceptor units, etc. to provide insight into the structure-property relationship as well as compatibility between ED and EA materials. Then, the latest photovoltaic trends in various types of ST-OSCs realized using these photoabsorbent materials, such as ternary and designed for multifunctional applications, like agrivoltaics, heat-resistant devices, floating photovoltaics (FPVs), solar glasses and automobile sunroofs, are also discussed. Lastly, we provide guidelines for the synthesis of efficient photoabsorbent materials for ST-OSCs and briefly discuss some design strategies to inspire novel ideas that could push this fascinating field into the future.

## 2. Critical Parameters for ST-OSCs

In this section vital parameters that were comprehensively used to evaluate the overall performance of ST-OSCs were explained. Because of the diversified applications of the ST-OSCs, a globally accepted standard has yet to be developed.

### 2.1. Average Visible Transmittance (AVT)

The luminosity or visible transmittance emerges as the next vital factor, which is used to quantify the effectiveness of the ST-OSCs after the electric performance. It is generally estimated by taking the average of the transparency of the devices in the visible region (370–740 nm) based on the photonic response of the human eye. Although the transparency needed for integration of ST-OSCs in various applications is completely dependent on the working environment, a minimum AVT of over 25% in the visible light range is thought to be desirable for practical applications.<sup>[43,54–56]</sup> Besides, it should be noted that experimentally determined AVT may be completely different from the human eye perception due to the human eye response is spectrally reliant. As indicated in the previous reports,<sup>[41,57]</sup> AVT is expressed according to the Equation:

$$\frac{\int T(\lambda) F(\lambda) E(\lambda) d\lambda}{\int F(\lambda) E(\lambda) d\lambda} \quad (1)$$

where  $T$  is the transmission spectrum,  $F$  is incident light flux, and  $E$  is the human eye photonic response.

## 2.2. Transparency Color Perception

Likewise, color perception is an additional essential factor that ought to be considered in ST-OSC technology, which is dependent on the type of incident light, photoabsorbent layer and electrodes, and estimated using the 1931 $x\gamma$  chromaticity diagram of the International Commission on Illumination (CIE).<sup>[1,52,58–60]</sup> Before employing ST-OSCs for practical use, its color ( $x, y$ ) coordinates were generally estimated from the transmitted light of the device (articulated as the product of incident and transmission spectrum). Typically, D65 (0.3128, 0.3290) or AM 1.5G (0.3202, 0.3324) solar spectrum is commonly used as incident light source for estimation of color parameters of ST-OSCs. The ST-OSCs having good color neutrality, i.e., color coordinates close to white light (0.33, 0.33) are usually preferred for window applications, owing to their ability to preserve the natural light condition.

## 2.3. Color-Rendering Index (CRI) and Corresponding Color Temperature (CCT)

The human eye has a unique ability to compensate for variations in color caused by various lighting conditions. The CRI is also another indicator used to describe a neutral color degree, which reveals the capacity of a light source to expose the object color in transmitted light as compared to natural or reference light.<sup>[41–42,61–63]</sup> The detailed calculation of CRI from the transmitted light of ST-OSCs devices using the CIE standard can be found in previous reports.<sup>[1]</sup> Typically, CRI values can range between 0 to 100 and higher CRI values of ST-OSCs signifies that the system has superior color translation capacity.<sup>[45]</sup> A variety of approaches (use of photoactive materials with NIR-absorption,<sup>[43,60]</sup> introductions of extra light-coupling/reflecting layers,<sup>[59,64]</sup> modifying ETL layer<sup>[45]</sup> and tandem devices<sup>[61,65]</sup>) were reported to improve CRI in ST-OSCs. The human eye can modify white light recognition to practically any dark body radiator. The black body locus or Planckian locus is nothing but a black body emission trace measured as a function of a temperature in an exceedingly specific color space.<sup>[63]</sup> The reference light source can be any standard light having a specific CCT value, where CCT is defined as the temperature of a dark body radiator which having nearby chromaticity to that of the transmission spectrum.<sup>[1,61]</sup> Moreover, it is calculated by inserting calculated Planckian locus values and the CIE 1931 $x\gamma$  coordinates into the CIE 1960 UCS color space diagram.<sup>[1,52,63]</sup>

## 2.4. Quantum Utilization Efficiency (QUE)

It is well known that external quantum efficiency (EQE) is by and large used to depict the usage proficiency of incident photons in OSCs. However, in the case of ST-OSCs, photons in the visible region that pass-through the device are also valuable and contribute to enhancing the AVT. Hence, to give a superior assessment of the overall properties of ST-OSCs, new

terminology “quantum utilization efficiency” (QUE) was proposed, which is described as the sum of EQE and transmittance ( $T$ ).<sup>[66]</sup> The QUE is described by the Equation:

$$\text{QUE} = \text{EQE} + T \quad (2)$$

Meanwhile, it should be noted that the QUE value must be lower than 90% in the entire spectral region owing to the unavoidable photon and carrier loss in ST-OSCs (like non-radiative or intrinsic recombination, interfacial reflection in the device and parasitic absorption, etc.).

## 2.5. Light Utilization Efficiency (LUE)

To give a reasonable comparison between various ST-OSCs technologies and overall system efficiency (which include both photogenerated PCE and lighting efficiency), the term, “light utilization efficiency” (LUE = PCE  $\times$  AVT) was proposed.<sup>[57,67]</sup> Based on the report by Li et al.<sup>[67]</sup> and Forrest and co-workers,<sup>[68]</sup> despite the superior PCE > 9% of the recent ST-OSCs incorporating efficient new photovoltaic materials, most of these photovoltaic cells displayed AVT  $\approx$  30%, leading to LUE < 4.0%, suggesting a superior trade-off between PCE and AVT is desirable to further improve LUE in the devices.

## 2.6. Infrared-Rejection Rate (IRR)

The infrared-rejection rate (IRR) parameter is exclusively used in dual functions ST-OSCs, which having both power generation and heat insulation functionalities.<sup>[35–38]</sup> It is well known that a thin layer of heat-control window films (comprising of thin transparent metal (e.g., Ag or Al) film or other low-emissivity materials) is commonly applied to the interior or exterior of the widely used glass windows, which can significantly reflect long or short-wave IR energy solar radiation, in turn, improving the power efficiency of buildings.<sup>[38]</sup> Based on the same concept, multifunctional ST-OSCs with sophisticated device architecture were developed, which can transmit a portion of visible light and additionally, can assimilate or reflect UV and IR photons which are prone to heat generation if not being utilized for photon conversion. Thus, an objective parameter IRR function was introduced to evaluate how effectively heat prone IR photons were rejected in ST-OSCs and a higher value indicating superior heat dissipation ability. The IRR is estimated from the averaged transparency of a cell in the IR wavelength region (780–2500 nm). Usually, the development of photovoltaic materials with selective photo absorption properties in the IR region or by insertion of distributed Bragg reflector (DBR) is comprised of many layers of alternating materials having the ability to reflect low energy NIR and IR photons are used to develop ST-OSCs with high IRR rate.

## 3. Photoabsorbent Materials for ST-OSCs

Generally, the photoabsorbent layer of ST-OSCs is comprised of organic semiconducting conjugated small molecules or

polymers as ED and EA units. As shown in the proposed light distribution of the AM 1.5G solar spectrum (Figure 1k), around 51% of solar photon flux is found in the NIR region, which is greater than the 47% and 2% in the visible and UV regions, respectively. Therefore, the probable PCE value of an OSCs employing an active layer capable of harvesting NIR photons is believed to be comparable to or higher than that of its counterparts with UV and visible absorption. Thus, there are two critical necessities for the ideal active layer of an efficient ST-OSC: 1) high efficiency and 2) absorbance in the UV (<435 nm) and/or NIR region (>670 nm) and high AVT in the visible region.<sup>[42,57]</sup> Consequently, the ideal active layer must be comprised of photovoltaic materials, with the main absorption peak located in the IR or NIR region and have relatively weak absorbance in the visible region and this allows the active layer to effectually apprehend balance between PCE and visible transparency.

### 3.1. Fullerene-Based ST-OSCs

Over the last two decades, fullerene-based acceptors (FAs) have ruled OSC research.<sup>[69]</sup> As the main absorption region of FAs is below 400 nm, most ST-OSCs made during this time used LBG-PDs with broad absorption and good energy level alignment with FAs to efficiently utilize photons in the NIR region and leave behind the light in the visible region to achieve good transparency.

Typically, large  $\pi$ -conjugation is a basic prerequisite to enable LBD-PDs, which is achieved by the introduction of highly fused core in the polymer repeat units and/or improving the rate of polymerization. However, to further extend the absorption beyond 800–1000 nm, two methods are commonly suggested as shown in Figure 2a-i) Synthesizing the polymers with donor-acceptor (D–A) molecular design: In addition to lowering of the bandgap of PDs due to the hybridization of frontier molecular orbitals (highest occupied molecular orbital (HOMO) and lowest unoccupied molecular orbital (LUMO)) between D and A components, this method promotes delocalization of electrons along the polymer backbone via strong push-pull effect.<sup>[70]</sup> ii) Stabilization of structure by quinoidal resonance along the conjugated backbone since it can yield a lower  $E_g$  than aromatic structure.<sup>[42,70]</sup> The chemical structures of the state-of-the-art PDs used in fullerene-based ST-OSCs are shown in Figure 2b and their photovoltaic performances are given in Table 1.

In 2011, Colsmann et al. reported the first ST-OSCs made of PC<sub>71</sub>BM acceptor and LBG-PD, PSBTBT,<sup>[71]</sup> which exhibit broad absorption up to the IR region ( $E_g$  of 1.45 eV) and high hole mobility ( $\mu_h$ ) of  $3 \times 10^{-3} \text{ cm}^2 \text{ V}^{-1} \text{ s}^{-1}$ . They achieved an overall PCE of 2.8% with a notable transparency color perception near to that of white light.<sup>[60]</sup> Later, using a PBDTTT-C-T and PC<sub>71</sub>BM blend system, Jen and co-workers fabricated ST-OSCs with an inverted device configuration, ITO/ZnO/C<sub>60</sub>-SAM/PBDTTT-C-T:PC<sub>71</sub>BM/molybdenum oxide (MoO<sub>3</sub>)/Ag.<sup>[43]</sup> The structure of PBDTTT-C-T was based on alternate benzodithiophene (BDT) and alkyl carboxylate-substituted thieno-[3,4-*b*]thiophene (TT) units and had an  $E_g$  of 1.58 eV.<sup>[72]</sup> By effectively tuning the thickness of the reflective Ag electrode (6–60 nm),

the authors realized remarkable PCEs ranging from 4.25% to 7.56% with the corresponding AVT of 36–2% and CRI > 96 (Figure 2c). Thus, this was one of the earliest reports, which indicated easy tailoring of ST-OSC transparency via variation in electrode thickness.

In the next study, the same group employed an active layer comprised of PD, PIDT-PhanQ and PC<sub>71</sub>BM, to fabricate ST-OSCs.<sup>[58]</sup> The molecular structure of PIDT-PhanQ is consisting of alternate electron-rich indacenodithiophene (IDT) and electron-deficient quinoxaline units. The optimal devices, with bilayer hybrid cathode containing 50 nm ultrathin Ag film deposited on fullerene-containing surfactant as the interfacial layer, yielded the best PCE of 5.63% (AVT of  $\approx$ 13%) with neutral color perception. Then, in 2017, Wong et al. tested a variety of ST-OSCs based on various PDs and PC<sub>71</sub>BM using the blade coating method.<sup>[73]</sup> The optimized small-area devices (active area of 0.04 cm<sup>2</sup>) with PBDTTT-CT:PC<sub>71</sub>BM and PBDTTT-EFT:PC<sub>71</sub>BM-based blends showed neutral color perception with good CRI values of 95.4 and 87.1 and maximum PCE of 5.2% and 5.6%, respectively. Additionally, the authors fabricated large-area ST-OSC devices (active area of 10.8 cm<sup>2</sup>) with the blade coating method, where the devices based on the aforementioned blends produced PCE values of 3.8% and 5.3%, respectively.

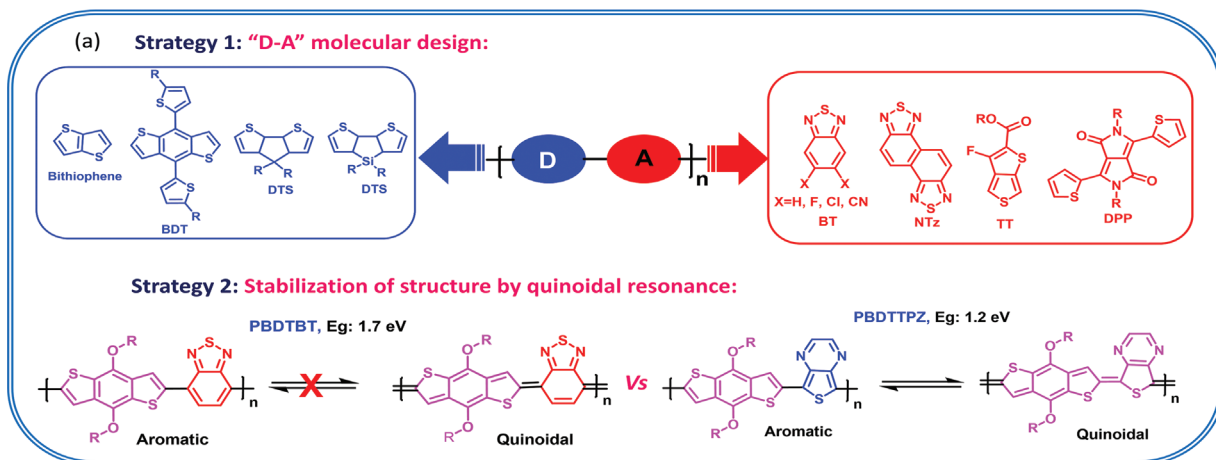
The other class of efficient LBG donor polymers includes PBDTT-DPP and PBDTT-SeDPP, which have a molecular structure composed of alternate strong electron-deficient diketopyrrolopyrrole (DPP) and weak electron-donating BDT units.<sup>[74–75]</sup> Both of these polymers exhibit main absorption peaks in the NIR regions ( $E_g$  < 1.5 eV), so they attracted the attention of the researchers for use in ST-OSCs. Chen et al. developed ST-OSCs with PBDTT-DPP:PC<sub>71</sub>BM-based active layers, which yielded a PCE of 4% and average transmittance (AT) of >61% at 400–650 nm.<sup>[74]</sup> Though PBDTT-DPP and PBDTT-SeDPP have similar backbone structures, the switching of thiophane with selenophene in PBDTT-SeDPP led to a further decrease in  $E_g$  from 1.46 to 1.38 eV due to the  $\approx$ 50 nm red-shifted absorption from 850 to 900 nm.<sup>[75]</sup> Indeed, a 4.5% PCE and a remarkable 58% AVT were realized using PBDTT-SeDPP:PC<sub>71</sub>BM-based ST-OSCs.

Chang et al. designed a novel PD, PCPDTFBT, with a fluorinated benzothiadiazole acceptor and cyclopenta[2,1-*b*:3,4-*b'*]dithiophene (CPDT) as a “D” unit, which had a broad NIR absorption (600–900 nm).<sup>[76]</sup> The authors mixed this novel PD with PC<sub>71</sub>BM and created ST-OSC devices with a PCE of 5.0% with low optical loss (AVT of 47.3%),<sup>[77]</sup> which is attributable to strong NIR absorption and poor absorbance of the PCPDTFBT:PC<sub>71</sub>BM blend in the visible region.

As a result of the impressive performance (PCE of 9.2%) of PM6:PC<sub>71</sub>BM-based opaque OSCs with thin layers ( $\approx$ 75 nm), Hou and co-workers tested its compatibility with ST-OSCs, although the main absorbance band of PM6 is located in the visible region (500–650 nm) with an  $E_g$  of 1.80 eV.<sup>[44]</sup> The optimized ST-OSCs with a device architecture of ITO/PFN/PM6:PC<sub>71</sub>BM/MoO<sub>3</sub>/Au (10 nm) afforded a PCE of 5.7% with an impressive AVT of  $\approx$ 67% and maximum transmittance ( $T_{\text{Max}}$ ) of 100% at 701 nm.

PTB7-Th is another well-known PD in the PTB class of polymers, with an alternate alkyl thienyl-substituted BDT donor

a) Molecular design strategies for low-bandgap polymer donors:



b) Chemical structure of photoabsorbent materials used in fullerene-based ST-OSCs

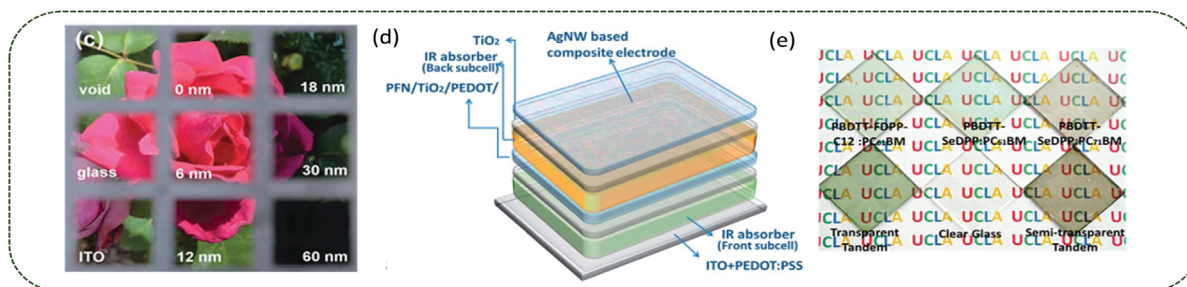
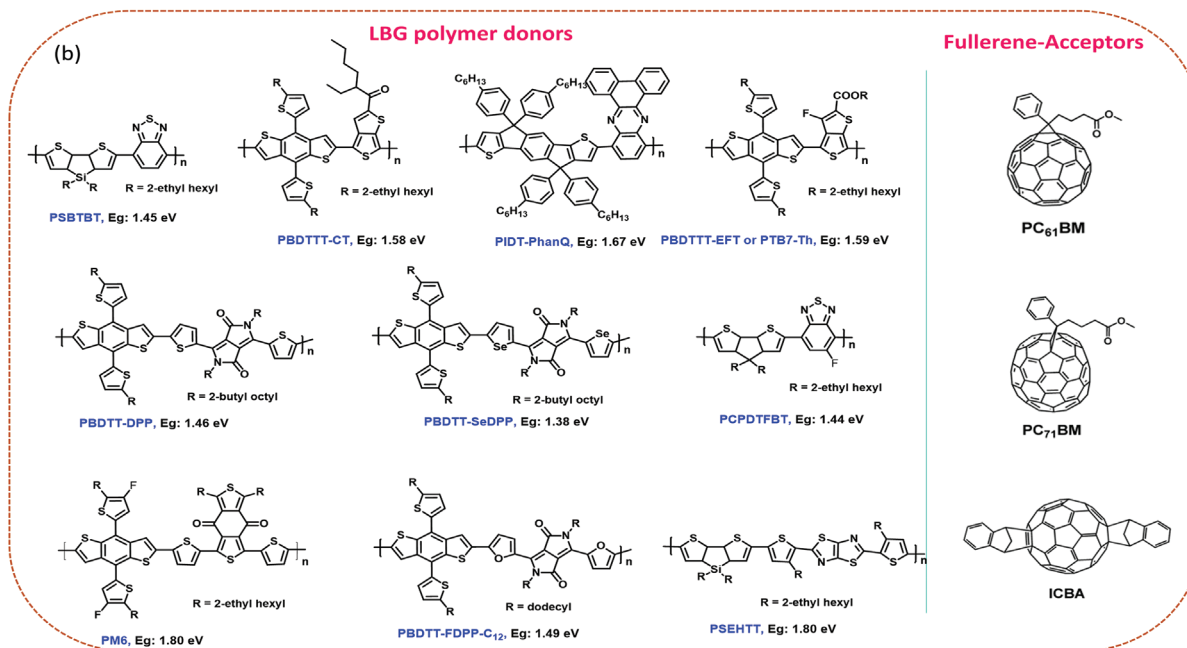


**Figure 2.** a) Molecular design strategies for synthesizing LBG-PDs; b) Chemical structure of photoabsorbent materials used in fullerene-based ST-OSCs; c) A photograph of a PBDTTT-C-T-based fullerene ST-OSCs with different Ag electrode thicknesses. Reproduced with permission.<sup>[43]</sup> Copyright 2012, the Royal Society of Chemistry and d) Schematic of a Tandem ST-OSC device and e) Photograph of the PBDTT-FDPP-C<sub>12</sub>:PC<sub>61</sub>BM, PBDTT-SeDPP:PC<sub>61</sub>BM, and PBDTT-SeDPP:PC<sub>71</sub>BM-based sub-cells and tandem devices with a different color. Reproduced with permission.<sup>[65]</sup> Copyright 2013, the Royal Society of Chemistry.

and fluorinated-TT as "A" units.<sup>[80]</sup> In addition to a narrow  $E_g$  of 1.59 eV with an absorption peak located at 780 nm, it also demonstrated a low HOMO of  $\approx 5.2$  eV, high- $\mu_h$  and excellent miscibility with FAs, resulting in excellent PCEs in OSCs.<sup>[80–81]</sup>

Using the synergic interface and optical engineering method, Shi et al. successfully employed a PTB7-Th:PC<sub>71</sub>BM blend to fabricate ST-OSCs, which delivered an impressive PCE of 6.78% with 20.71% AVT.<sup>[45]</sup> Effective light harvesting up to the

**Table 1.** Photovoltaic and optical parameters of fullerene-based ST-OSCs.

Blend	$V_{oc}$ [V]	$J_{sc}$ [mA cm <sup>-2</sup> ]	FF [%]	PCE [%]	AVT/AT [%] <sup>a)</sup>	CRI <sup>b)</sup> @ CCT <sup>c)</sup> /CIE (x, y) <sup>d)</sup>	Ref.
Fullerene-based single BHJ ST-OSCs							
PSBTBT:PC <sub>71</sub> BM	0.608	10.7	42	2.80		83 @ 5307 K/(0.3382, 0.3770)	[60]
PBDTTT-C-T:PC <sub>71</sub> BM	0.76	14.54	64	7.05	10.6	96.7 @ 8390 K/(0.2917, 0.3010)	[43]
PIDT-PhanQ:PC <sub>71</sub> BM	0.85	10.96	62	5.63	13.03	- @ -/(0.341, 0.342)	[58]
PBDTTT-CT:PC <sub>71</sub> BM	0.82	13.8	46.0	5.20	14.0	95.4 @ 8510/ (0.2858, 0.3125)	[73]
PBDTTT-EFT:PC <sub>71</sub> BM	0.84	11.0	61.0	5.60	10.0	87.1 @ 7013/ (0.3036, 0.3283)	[73]
PBDTT-DPP:PC <sub>71</sub> BM	0.77	9.30	56.2	4.02	61 (at 400–650 nm)	–	[74]
PBDTT-DPP:SePC <sub>71</sub> BM	0.72	11.5	55.0	4.50	58	–	[75]
PCPDTFBT:PC <sub>71</sub> BM	0.74	11.39	58.56	5.0	47.3 (at 380–700 nm)	–	[77]
PM6:PC <sub>71</sub> BM	0.96	9.4	63	5.7	67 (at 380–780 nm)	–	[44]
PTB7-Th:PC <sub>71</sub> BM	0.77	12.66	69.5	6.78	20.71	96.4 @ 6502 K/(0.314, 0.318)	[45]
Fullerene-based tandem ST-OSCs							
F, PBDTT-FDPP-C <sub>12</sub> :PC <sub>61</sub> BM R, PBDTT-SeDPP:PC <sub>61</sub> BM	1.47	8.4	59	7.3	30 (at 400–650 nm)		[65]
F, PSEHTT:IC <sub>60</sub> BA R, PBDTT-DPP:PC <sub>71</sub> BM	1.62	7.62	64.21	8.02	44.90 (at 300–950 nm)		[78]
F, PIDT-phanQ:PC <sub>61</sub> BM R, PIDT-phanQ:PC <sub>71</sub> BM	1.47	5.57	58.64	6.7	40.0 (at 380–700 nm)	97.2 @ 5622 K/(0.330, 0.339)	[79]

<sup>a)</sup>AVT = average of the transmittance of the solar cells in the visible region (370–740 nm) and AT = average of the transmittance of the solar cells in specific wavelength region; <sup>b)</sup>color rendering index (CRI); <sup>c)</sup>Corresponding color temperature (CCT); <sup>d)</sup>CIE (x, y) = color coordinates derived from CIE 1931 chromaticity diagram.

NIR region and light management due to optical engineering was the reason behind this high PCE.

Generally, the use of a thin layer of photoabsorbent materials together with the use of a transparent electrode causes an inevitable loss of  $J_{sc}$  and performance in ST-OSC devices because only a small flux of the incident light is absorbed by the active layer. Several device modification approaches have been developed to overcome these issues. Compared to single-junction solar cells, tandem solar cells in which two or more different sub-cells with complementary absorption profiles are stacked in series can more effectively harvest energy from the solar spectrum.<sup>[15,82–84]</sup> Hence, few groups used this device engineering approach to further boost the performance of FA-based ST-OSCs.

For example, Chen et al. reported tandem ST-OSCs based on two PDs, PBDTT-FDPP-C<sub>12</sub> ( $E_g$  of 1.49 eV) and PBDTT-SeDPP ( $E_g$  of 1.38 eV), which both have main absorption peaks located between ≈650 and 900 nm region of the IR spectrum, but with an ≈50 nm difference in the absorption maximum.<sup>[65]</sup> By using the stalks of PBDTT-FDPP-C<sub>12</sub>:PC<sub>61</sub>BM and PBDTT-SeDPP:PC<sub>71</sub>BM as front and rear cells, respectively, optimal tandem ST-OSCs delivered a notable PCE of 7.3% with an AT of 30% at 400–650 nm (Figure 2d,e).

Jang and co-workers developed efficient tandem ST-OSCs based on PSEHTT:IC<sub>60</sub>BA (front cell) and PBDTT-DPP:PC<sub>71</sub>BM (rear cell) sandwiched between a solution-processed graphene mesh as TTE and laminated Ag nanowires as BTE, and connected electrically in series with an interconnection layer

(PEDOT:PSS and TiO<sub>2</sub> as hole transport and electron transport layer, respectively).<sup>[78]</sup> The corresponding tandem ST-OSC was found to deliver a remarkable PCE of 8.02% with an AT of 44.9% from 300–950 nm. Moreover, these devices also showed good tunability of transmittance (ranging from 44.9% to 39.9%) via control of the thickness of the TiO<sub>2</sub> layer (5–20 nm).

Chang et al. fabricated ST-OSCs comprised of PIDT-phanQ:PC<sub>61</sub>BM (70 nm) and PIDT-phanQ:PC<sub>71</sub>BM (85 nm) as the front and rear cell, respectively, which exhibited a notable PCE of 6.7% and 40% AVT at 380 and 700 nm.<sup>[79]</sup> Furthermore, these devices also showed a very good CRI of 97, CCT of 5622 K and CIE color coordinates of (0.3297, 0.3387), suggesting their potential for power-generating window applications.

In summary, these examples clearly emphasize that the incorporation of LBG-PDs greatly contributed to the performance enhancement of fullerene-based ST-OSCs. However, intrinsic limitations of FAs, such as poor absorption in the visible and NIR region, limited chemical modification or energy level tailoring, and unoptimized device architecture, impeded the further progress toward practical applications of fullerene-based ST-OSCs. Alternatively, simultaneous optimization of the transparency, appearance and performance of tandem ST-OSCs is inherently challenging, and these devices are more difficult to fabricate and reproduce than binary bulk heterojunction (BHJ) ST-OSCs, hence only limited progress has been realized to date. Consequently, this paved the way for the development of ST-OSCs comprised of both NIR-absorbing “ED” and “EA” units with a simple fabrication of binary BHJ.

### 3.2. Non-Fullerene-Based ST-OSCs

The recent rapid progress of non-fullerene FREAs with NIR absorption offers new opportunities to accomplish a superior balance between the efficiency and transparency of ST-OSCs. In addition to superior optical absorption properties compared to their fullerene counterparts, the flexible molecular design of FREAs offers various advantages, such as easy tailoring of frontier energy levels, low synthetic cost, easy control over crystallinity, etc.<sup>[10,85–91]</sup> Moreover, the high co-polarity and strong intermolecular interaction ( $\pi$ - $\pi$  stacking) of FREAs helps to minimize rotational disorder and reorganization energy, thus facilitating superior charge mobility and low energy loss ( $E_{\text{loss}} = E_{\text{g}} - eV_{\text{OC}}$ , where  $V_{\text{OC}}$  is the open-circuit voltage).<sup>[10,85–89]</sup> Typically, most of these NFAs were developed based on an “A–D–A”/ “A–DA’D–A” or “A–( $\pi$ -spacer)–D–( $\pi$ -spacer)–A” type configuration, in which a central electron-donating fused-ring heterocyclic “D” or “DA’D” with outstretched side chain is connected to terminal end-capping “A” via vinyl linkage or  $\pi$ -spacer unit, which is then interconnected to “A” units by vinyl linkage (Figure 3a). By chemical modification of central “D” units/side chains,  $\pi$ -spacer and terminal “A” groups, the optoelectronic properties, molecular packing, charge-transport, and photovoltaic properties of resultant NFAs could be synergistically tailored.<sup>[91]</sup>

Typically, two main approaches are widely used to realize NIR absorption in these NFAs (Figure 3a). First, enhancing the number of fused-ring heterocyclic cores in the central “D” unit or “inserting a  $\pi$ -spacer” can enhance ICT, broaden absorption and elevate energy levels by effective delocalization of  $\pi$ -electron.<sup>[85–86,92–95]</sup> Moreover, this strategy also facilitates effective stacking and enhanced crystallinity, leading to enhanced charge carrier mobility. The second widely used approach to achieving NIR absorption in NFAs involves increasing the electron-pulling effect via incorporation of the appropriate terminal “A” units having different functional groups.<sup>[85–86,96]</sup> As indicated in several of the latest studies, these terminal “A” units not only influence photophysical properties and  $E_{\text{g}}$ , but also influence molecular orientation and morphology because of non-covalent interactions.<sup>[85–86,92–95]</sup> Recently, a number of these electron-deficient end groups have become available, and have been extensively used to modulate the properties of NFAs. Consequently, a variety of highly efficient NIR-absorbing NFAs with extended conjugation has been created by using either of these design approaches, which demonstrate superior compatibility in ST-OSCs (Figures 3b and 5), and their photovoltaic performances are summarized in Table 2.

In 2017, Zan and co-workers produced a milestone NFA, ITIC, based on a central rigid IDT core and end-capped with two 1,1-dicyanomethylene-3-indanone (DCI) units.<sup>[97]</sup> It has intense absorption in the  $\approx$ 600–800 nm region with an  $E_{\text{g}}$  of 1.59 eV and a LUMO of  $-3.83$  eV; hence, it is presumed to be a suitable candidate for enhancing PCE in ST-OSCs. By mixing ITIC with PD, PBDB-T with complementary absorption (500–700 nm) and well-aligned energy levels, Upama et al. realized PCEs exceeding 7% and 25% AVT in inverted ST-OSCs with  $\text{MoO}_3/\text{Ag}/\text{MoO}_3$  as a transparent anode.<sup>[56]</sup> Thus, effective light management via an appropriate selection of blend

components covering a broad absorption range from 500 to 800 nm together with optical engineering led to high PCE.

Wang et al. developed a new NFA, IHIC, where the central benzene-based IDT core in ITIC is swapped with thienothiophene (TT) to form a new central electron-donating hexacyclic dithienocyclopentathieno[3,2-*b*]thiophene (4T) units, to use in ST-OSCs.<sup>[98]</sup> Compared to IDT core, 4T exhibit more effective  $\pi$ -electron delocalization due to the lower resonance stabilization energy of TT versus benzene. Therefore, because of the strong ICT effect between the central 4T core and DCI units, IHIC exhibited NIR absorption with an ultra-low  $E_{\text{g}}$  of 1.38 eV and a high molar extinction coefficient of  $1.6 \times 10^5 \text{ m}^{-1} \text{ cm}^{-1}$ . Additionally, it also showed higher electron mobility ( $\mu_{\text{e}}$ ) of  $2.4 \times 10^{-3} \text{ cm}^2 \text{ V}^{-1} \text{ s}^{-1}$  owing to a highly co-planar backbone and enhanced intermolecular S–S interactions. Eventually, an ST-OSC device was prepared by mixing with complementary absorbing PTB7-Th with IHIC, which displayed extended absorption from  $\approx$ 600 to 900 nm and excellent charge transport properties with suppression of charge recombination, leading to a remarkable PCE of 9.77% with high transmittance (AVT of 36%) and superior stability with retention of  $\approx$ 97% of the initial PCE value even after 130 min under continuous light illumination.

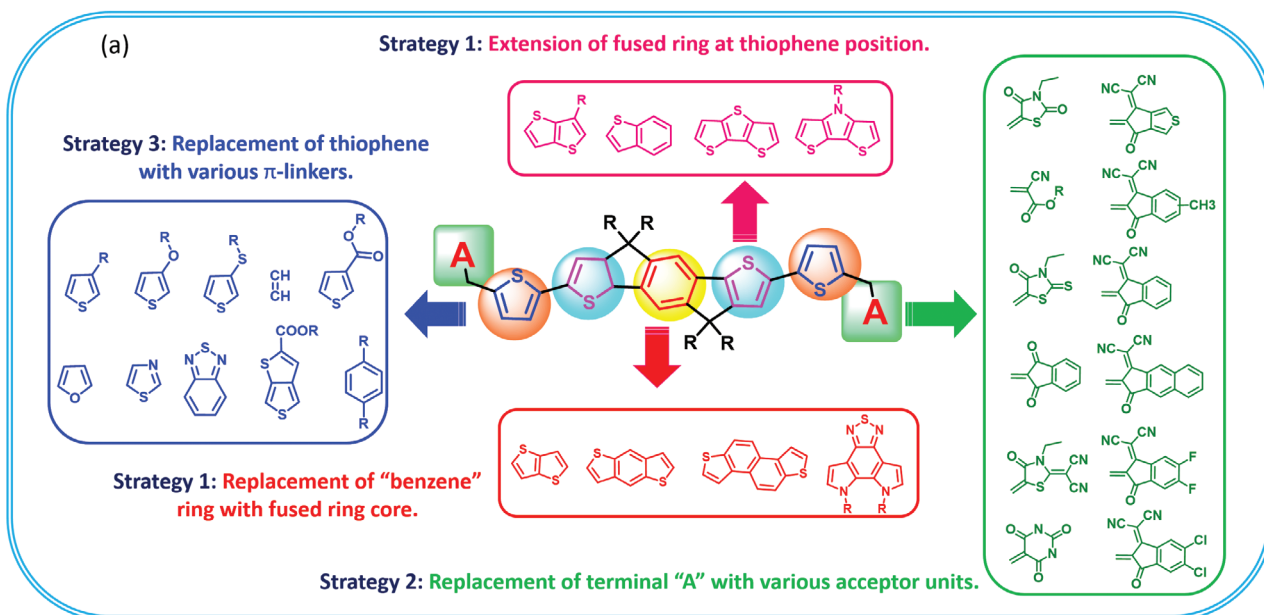
Motivated by this molecular strategy, the Jen group further enhanced the  $\pi$ -conjugation of the central electron-donating terthieno[3,2-*b*]thiophene (6T) “D” unit by introducing two more thienyl moieties, to form 6TIC.<sup>[94]</sup> As anticipated, given the higher electron-donating capability and lower reorganization energy of the 6T core and from the stronger ICT effect caused by combining 6T with DCI end groups, 6TIC displayed broad absorption in the NIR region (600–905 nm,  $E_{\text{g}} = 1.37$  eV). Moreover, by mixing with PTB7-Th, the PTB7-Th:6TIC blend also demonstrated favorable molecular packing, higher charge mobilities and lower  $E_{\text{loss}}$  ( $\approx$ 0.55 V), which can aid in improving PCE by effective NIR light-harvesting and efficient charge transport. Consequently, a PCE of 7.62% (AVT 23.3%) with a respectable  $J_{\text{SC}}$  ( $14.58 \text{ mA cm}^{-2}$ ) was shown by an ST-OSC based on these blends.

Sun et al. prepared C8-ITIC, an ITIC analog, in which the phenyl alkyl side chains of ITIC were switched with linear octyl side chains.<sup>[99]</sup> Relative to ITIC, C8-ITIC showed a lower  $E_{\text{g}}$  of 1.55 eV with  $\approx$ 30 nm red-shifted absorption, enhanced crystallinity and higher  $\mu_{\text{e}}$  due to improved intermolecular packing. The authors fabricated ST-OSCs with bilayer  $\text{MoO}_3/\text{Ag}$  and multilayer  $\text{MoO}_3/\text{Ag}/\text{MoO}_3$  electrodes, respectively and systematically evaluated the role of deposition rate and thickness of both the Ag and  $\text{MoO}_3$  layer on the optical and electrical properties of the devices. The optimal ST-OSCs comprising a complementary absorbing PFBDB-T donor and  $\text{MoO}_3/\text{Ag}/\text{MoO}_3$  electrode yielded the best PCE of 9.8%, AVT of 22% and CIE ( $x, y$ ) color coordinates of (0.24, 0.29) due to efficient NIR photon harvesting and sophisticated optical engineering (Figure 4a–c).

Incorporation of electron-withdrawing substituents, especially halogens, on the end-capping “A” units is one of the most fruitful and reliable methods of synthesizing NIR-absorbing NFAs by enhancing the electron-pulling effect.<sup>[86–87,96]</sup> Fluorine (F), the smallest electronegative atom (3.98 for F on the Pauling scale)<sup>[48]</sup> among the halogens, has been widely used to design efficient active layer materials for OSCs.<sup>[8,16,100–106]</sup> In addition to lowering the HOMO/LUMO energy levels, the insertion of F-substituents



a) Molecular design strategies for non-fullerene acceptors:



b) Chemical structure of NFAs used in ST-OSCs

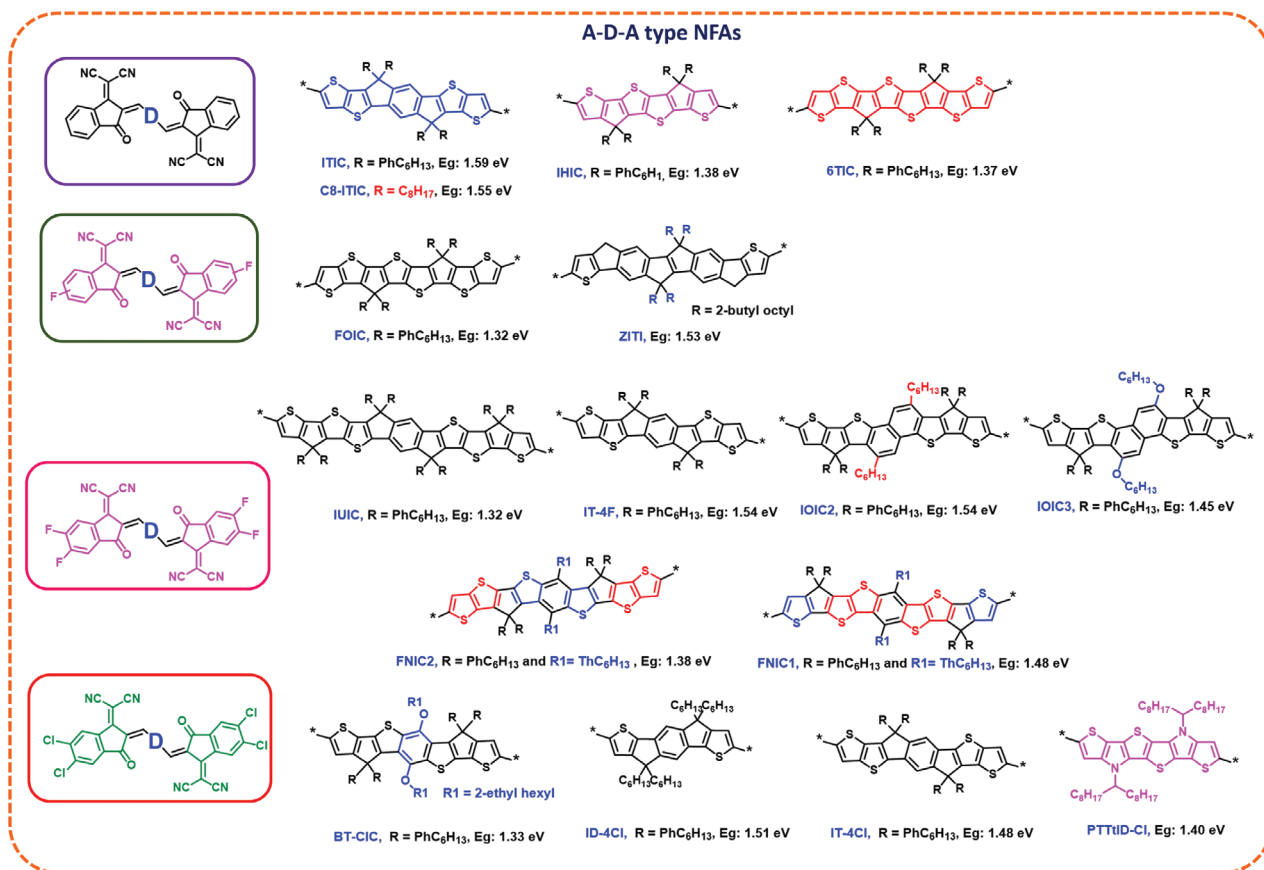


**Figure 3.** a) Molecular design strategies for synthesizing LBG-NFAs and b) the chemical structure of NFAs used in ST-OSCs.

significantly enhances ordered intermolecular packing and crystallinity through non-covalent intra/intermolecular interactions.<sup>[100,107–109]</sup> Moreover, the higher dipole moment of the C–F

bond also enhances the absorption range and reduces bandgaps in the NFAs through a stronger ICT effect.<sup>[97,110–112]</sup> Hence, many research groups synthesized various new NIR-absorbing NFA

**Table 2.** Photovoltaic and optical parameters of non-fullerene-based ST-OSCs.

Blend	$V_{oc}$ [V]	$J_{sc}$ [mA cm <sup>-2</sup> ]	FF [%]	PCE [%]	AVT/AT [%] <sup>a)</sup>	CRI <sup>b)</sup> @ CCT <sup>c)</sup> /CIE (x, y) <sup>d)</sup>	Ref.
PBDB-T:ITIC	0.88	13.8	59.08	7.30	25.2	44 @ - / (0.25, 0.27)	[56]
PTB7-Th:IHIC	0.754	19.01	68.1	9.77	36.0	86 @ 9689/(0.2730, 0.3097)	[98]
PTB7-Th:6TIC	0.823	14.58	63.50	7.62	23.3	–	[94]
PFBDB-T:C8-ITIC	0.92	15.51	70.00	9.80	22.0	- @ - / (0.24, 0.29)	[99]
PTB7-Th:FOIC	0.739	20.0	69.9	10.30	37.4	–	[113]
PDTP-DFBT:FOIC	0.71	10.90	52.0	4.2	52	90.9 @ 5700 K/ (0.3274, 0.3593)	[114]
PTB7-Th:IUIC	0.794	18.31	70.3	10.2	31	75 @ 16753 K/(0.2331, 0.2870)	[115]
PTB7-Th:ITIC4	0.680	13.2	71.6	6.42	28	85 @ 10918 K/(0.2649, 0.3204)	[115]
PBT-Cl:IT-4F	0.749	18.52	58.9	8.18	31.7	88 @ - / (0.240, 0.272)	[121]
PBN-S:IT-4F	0.884	16.78	66.4	9.83	32	92 @ - / (0.205, 0.231)	[118]
PTB7-Th:IOIC2	0.809	13.9	65.2	7.32	13.1	–	[122]
PTB7-Th:IOIC3	0.755	19.6	72.5	10.8	16.4	–	[122]
PTB7-Th:FNIC1	0.772	18.33	64.6	9.14	14.7	81 @ 13002/(0.2211, 0.3317)	[123]
PTB7-Th:FNIC2	0.728	21.87	72.6	11.6	13.6	83 @ 11639/(0.2310, 0.3408)	[123]
PTB7-Th:FNIC1	0.769	18.27	63.4	8.91	14.7 (at 350–750 nm)	–	[124]
PTB7-Th:FNIC2	0.727	21.42	71.6	11.1	13.9 (at 350–750 nm)	–	[124]
J101:ZITI	0.898	19.06	64.51	11.04	21.69 (at 400–650 nm)	–	[48]
PTB7-Th:BT-CIC	0.68	18.0	67.5	8.2	26	91 @ 7784 K/(0.29, 0.32)	[127]
PM-6-ID-4Cl	0.748	13.77	67.90	6.99		–	[130]
PBFTT:IT-4Cl	0.74	17.6	70.1	9.1	27.6	- @ 7923 K/(0.279, 0.362)	[119]
PTB7-Th:PTTtID-Cl	0.72	17.4	60.2	7.7	16.7	–	[131]
P3HT:IDT-2Br	0.84	6.23	61.5	3.22	50	–	[132]
PTB7-Th:ATT-2	0.712	18.53	59.0	7.74	37	94.1 @ 9113/(0.2805, 0.3076)	[133]
PBDTTT-ET:IEICO	0.81	16.3	0.67	9.0	17.7	- @ - / (0.205, 0.211)	[38]
PTB7-Th:IEICO-4F	0.718	20.59	64.0	9.48	23.7	- @ 11 053/(0.2650, 0.2996)	[120]
DPP2T:IEICO-4F	0.75	10.61	69.5	5.74	AT of 60 (at 400–600 nm)	- @ - / (0.3173, 0.3713)	[134]
PTB7-Th:IEICO-4F	0.67	19.6	65.3	8.5	21.5	59.87 @ 10 764/(0.259, 0.312)	[135]
PTB7-Th:ACS8	0.74	22.5	66.5	11.1	28.6	84 @ 11 528 / (0.2621, 0.2976)	[136]
PCE-10:A078	0.75	20.9	70.0	11.0	25.0	- @ - / @ 9021/(0.27, 0.39)	[68]
PTB7-Th:IEICO-4Cl	0.725	19.6	59.0	8.38	25.6	–	[30]
PTB7-Th:ITVfIC	0.742	17.54	63.11	8.21	26.40	- @ 7422/(0.29, 0.36)	[137]
PTB7-Th:DTG-IW	0.71	14.6	60.0	6.19	AT 50.4 (at 500–540 nm)	–	[138]
PM-6:Y6	0.854	23.01	72.27	14.20	8.9	- @ infinity/(0.2422, 0.2240)	[47]
PM-6:Y6	0.852	20.35	71.36	12.37	18.6	- @ 24383/(0.2551, 0.2506)	[47]
PBT1-C-2Cl:Y6	0.83	19.51	70.2	11.7	19.7	–	[49]
PBDB-T-2F:Y6	0.81	21.23	72.99	12.59	17.0	- @ - / (0.2287, 0.2213)	[50]
PBDB-T:Y14	0.793	22.48	71.06	12.67	23.69	–	[139]
PBDTZT-stat-DBTT-8:4TICO	0.69	12.9	53.3	4.7	20	–	[140]

<sup>a)</sup>AVT = average of the transmittance of the solar cells in the visible region (370–740 nm) or visual light transmittance (VT) and AT = average of the transmittance of the solar cells in specific wavelength region; <sup>b)</sup>color rendering index (CRI) and; <sup>c)</sup>Corresponding color temperature (CCT); <sup>d)</sup>CIE (x, y) = color coordinates derived from CIE 1931 chromaticity diagram.

units via integration of a different number of F-substituents on the terminal “A” units in the A-D-A molecular design and the one used to fabricate ST-OSCs are shown in Figure 3b.

For example, Li et al. replaced the two DCI terminal groups in 6TIC with monofluorinated-DCI (F-DCI) units with stronger electron-withdrawing ability to form FOIC.<sup>[113]</sup> For comparison with the corresponding ITIC analog, ITIC3, which is based on an IDT core and contains the same F-DCI end groups, was also prepared. Because of the strong electronegativity of F and enhanced ICT effect caused by the central 6T core and electron-deficient F-DCI unit, FOIC exhibits deep HOMO and LUMO energy levels, red-shifted absorption ( $\approx 100$  nm), a smaller  $E_g$  of 1.32 eV and a higher absorption coefficient ( $2 \times 10^5 \text{ M}^{-1} \text{ cm}^{-1}$ ) than ITIC3. Additionally, favorable molecular orientation and high crystallinity led to higher  $\mu_e$ . Consequently, the corresponding ST-OSCs prepared by blending with PTB7-Th donor demonstrated enhanced  $J_{SC} = 20.0 \text{ mA cm}^{-2}$ ,  $V_{OC} = 0.739 \text{ V}$ , and FF (fill factor) = 69.9%, and then-record PCE values for ST-OSCs, i.e., 10.3%, with an excellent AVT of 37.4%. This was the first report in which PCEs beyond 10% were achieved for ST-OSCs. Later, by incorporating new ultra-LBG donor PDTP-DFBT, which has an absorption peak in the 600–900 nm range ( $E_g = 1.38 \text{ eV}$ ), Sun and co-workers developed ST-OSCs by pairing with a FOIC acceptor.<sup>[114]</sup> Though ST-OSCs based on the PDTP-DFBT:FOIC blend yielded high transmittance in the visible region ( $\approx 52$ – $62\%$ ) with CRI values  $> 90$ , but they displayed poor PCEs of 3.5–4.2% due to poor NIR light-harvesting and unbalanced charge mobilities.

Zan and co-workers introduced a fused-undecacyclic (11-ring core) “IU” donor core and synthesized one of the largest NFA core, IUIC, by flanking IU with two terminal difluorinated-DCI (2F-DCI) cores as an “A” unit.<sup>[115]</sup> As anticipated, stronger ITC effect between electron-donating IU core having large  $\pi$ -conjugation and terminal 2F-DCI units led to high lying LUMO energy levels ( $-3.87 \text{ eV}$ ), a stronger absorption co-efficient of  $3 \times 10^5 \text{ M}^{-1} \text{ cm}^{-1}$  with panchromatic absorption ( $E_g = 1.41 \text{ eV}$ ), and a higher  $\mu_e$  of  $1.1 \times 10^{-3} \text{ cm}^2 \text{ V}^{-1} \text{ s}^{-1}$  in IUIC, which is useful to achieve higher  $J_{SC}$  values by further extending absorption range. So, ST-OSCs with PTB7-Th:IUIC displayed an impressive PCE of 10.2% with an AVT of 31%, outperforming reference devices based on PTB7-Th:ITIC4 (PCE = 6.42% and AVT = 28%) studied in parallel. These results suggest that the introduction of larger fused ring units could be useful means to extend the spectral absorption range in NFAs.

Like ITIC, tetra fluorinated ITIC (IT-4F) is a commonly studied versatile NFA unit, which has been used to produce numerous highly efficient NF-OSCs in combination with various appropriate PDs.<sup>[110,116–117]</sup> Due to the presence of two F-substituents on each DCI unit, IT-4F demonstrated lower frontier energy levels, stronger absorption-co-efficient and higher crystallinity, which led to enhanced  $\mu_e$  in comparison with ITIC. Moreover, the main absorption peak of IT-4F is located in the range of 650 to 800 nm ( $E_g = 1.54 \text{ eV}$ ), and it has a good transparency window in the visible region (400–600 nm), which suggests that IT-4F could be an ideal choice for the fabrication of ST-OSCs in combination with an appropriate PD unit.<sup>[110]</sup> Indeed, Li and co-workers used a blend of newly synthesized PD, PBT-Cl and IT-4F acceptor as a photo-harvesting layer to fabricate ST-OSCs with non-halogenated *m*-xylene as

a processing solvent.<sup>[121]</sup> Through delicately tailoring the blend ratio of the active layer components and the thickness of the transparent Ag electrodes, the authors achieved a maximum PCE of 8.18% and a high AVT of 31.7% for ST-OSCs with the device structure of ITO/PEDOT:PSS/PBT-Cl:IT-4F/perylene diimide functionalized with amino N-oxide (PDINO)/Au (1 nm)/Ag (20 nm). Following this success, the same group fabricated ST-OSCs based on PBN-S as a donor and ITIC-4F with the device structure of ITO/PEDOT:PSS/PBN-S:IT-4F (1:1, wt/wt)/ZnO/Au (1 nm)/Ag (20 nm).<sup>[118]</sup> The PBN-S:IT-4F-based blend showed strong absorption in the 600–800 nm region, higher and balanced charge carrier mobilities and superior morphology with favorable molecular orientation. As a result, the optimal ST-OSC devices afforded a maximum PCE of 9.83% and AVT of 32% (Figure 4d–f).

Zhu et al. prepared two new NFAs based on a central naphtho[1,2-*b*:5,6-*b'*]dithiophene (NDT) donor core and adjacent 2F-DCI end groups by drafting different alkyl side chains, namely, IOIC3 (with an alkoxy side chain attached to NDT) and IOIC2 (with an alkyl side chain attached to NDT), to evaluate the effect of different alkyl side chains in the NFAs.<sup>[122]</sup> Relative to IOIC2, IOIC3 showed elevated HOMO and deepened LUMO, attributable to the  $\pi$ -conjugative effect and  $\sigma$ -inductive effect of the oxygen atoms, which subsequently resulted in  $\approx 50$  nm red-shifted absorption with NBG (IOIC3 and IOIC2 had an  $E_g$  of 1.45 and 1.54 eV, respectively). Additionally, a grazing-incidence wide-angle X-ray scattering (GIWAXS) study revealed that, despite the “face-on” molecular orientation of both NFAs in a pristine state, IOIC3 shows stronger  $\pi$ - $\pi$  stacking than IOIC2, thereby leading to a superior  $\mu_e$  of  $1.5 \times 10^{-3} \text{ cm}^2 \text{ V}^{-1} \text{ s}^{-1}$ . The authors fabricated ST-OSCs based on an ITO/ZnO/active layer/MoO<sub>3</sub>/Au (1 nm)/Ag (20 nm) device structure and PTB7-Th as an ED. PTB7-Th:IOIC3-based devices achieved a remarkable PCE of 10.8% (AVT = 16.4%), which is considerably higher than the values displayed by their PTB7-Th:IOIC2 counterpart (PCE/AVT = 7.32/13.1%). So, strong NIR absorption, high EQE values of  $>70\%$  ranging from 550 to 800 nm, and “face-on” molecular orientation with higher charge carrier mobilities were the basis of the superior PCE in ST-OSCs based on PTB7-Th:IOIC3 blended films.

In another case study, Zhan and co-workers reported two new NBG-NFAs, FNIC1, and FNIC2, which have the same terminal 2F-DCI end groups and side chains, but an isomeric 9-membered central donor unit.<sup>[123]</sup> They studied the influence of the isomeric effect of NFAs on the performance of the corresponding OSCs. Due to the subtle changes in molecular structure, FNIC2 showed enhanced absorption (the  $E_g$  of FNIC1 and FNIC2 were 1.48 and 1.38 eV, respectively), larger electron affinity, and higher crystallinity and  $\mu_e$  relative to FNIC1. Thus, ST-OSCs based on the PTB7-Th:FNIC2 blended system displayed maximum PCE values ranging between 9.51–11.6%, with different AVT values (20.3% to 13.6%) depending on the thickness of the electrode. On the other hand, PTB7-Th:FNIC1-based devices displayed a maximum PCE of 9.14% with an AVT of 14.7%. In a subsequent study, the same group tested the influence of film depth-dependent crystallinity of both of these blended films on the optoelectronic properties of ST-OSCs by using the different solvent additives and the inverted device architecture of ITO/ZnO/PTB7-Th:FNIC1 or FNIC2

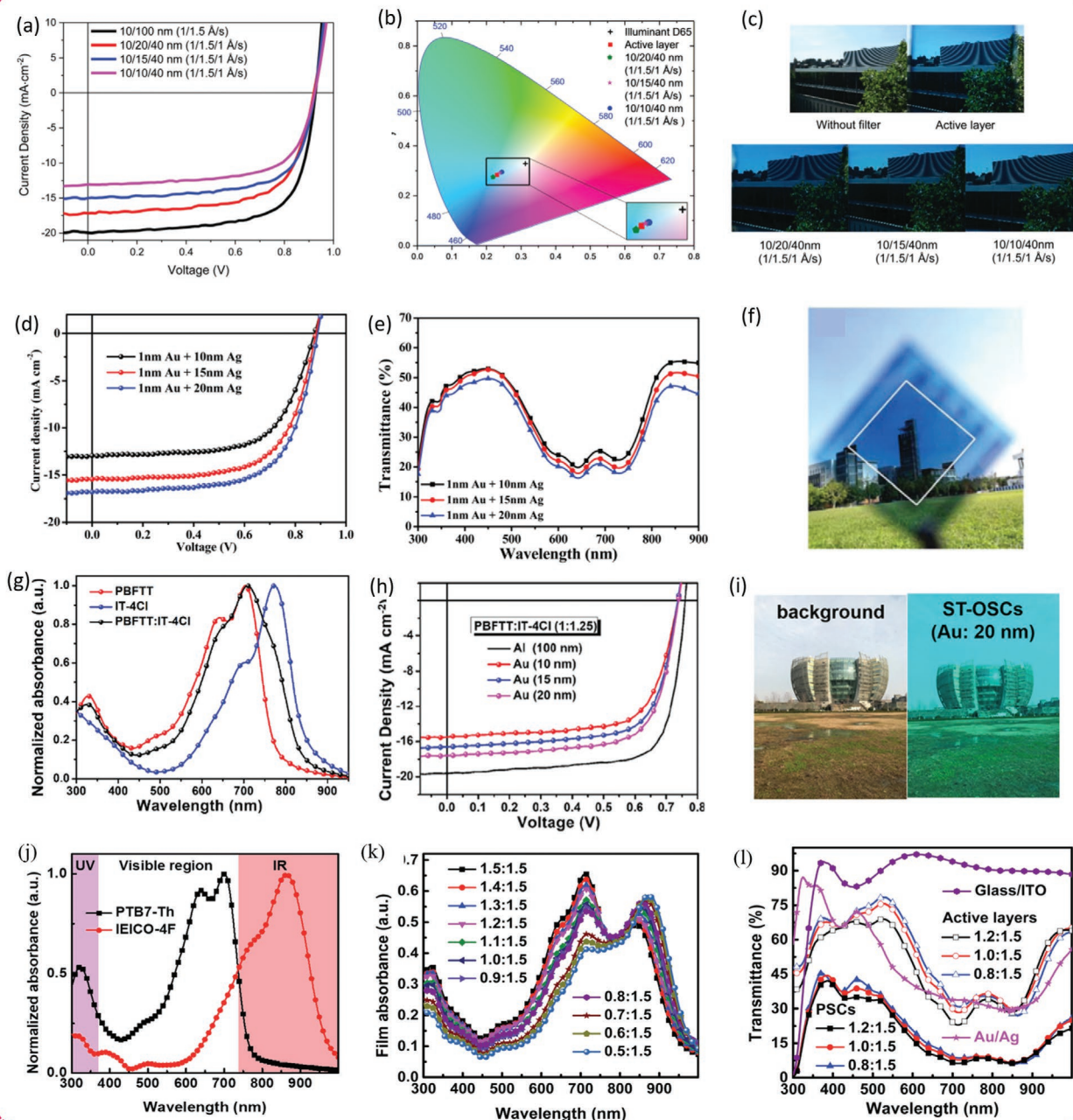


**Figure 4.** a)  $J$ - $V$  characteristics of ST-OSCs based on PFBDB-T:C8-ITIC-based active layer and multilayer  $\text{MoO}_3/\text{Ag}/\text{MoO}_3$  electrode with different thickness; b) Color coordinates and c) Images of corresponding optimized ST-OSCs. Reproduced with permission.<sup>[99]</sup> Copyright 2019, the Royal Society of Chemistry; d)  $J$ - $V$  characteristics of ST-OSCs based on PBN-S:IT-4F with different Ag thicknesses; e) Corresponding transmission spectra and f) Outdoor image through the ST-OSCs. Reproduced with permission.<sup>[118]</sup> Copyright 2019, the Royal Society of Chemistry; g) Normalized absorption spectra of PBFTT, IT-4Cl, and PBFTT:IT-4Cl films h)  $J$ - $V$  curves and i) Photographs of the without/ optimal ST-OSCs based on PBFTT:IT-4Cl with 20 nm thick Au layer. Reproduced with permission.<sup>[119]</sup> Copyright 2019, Owner Societies; j) Normalized absorption spectra of neat PTB7-Th and IEICO-4F films; k) absorption spectra of blend films with different PTB7-Th:IEICO-4F blend ratios and l) transmission spectra of the PTB7-Th:IEICO-4F-based ST-OSCs with device architecture of glass/ITO substrate, 1 nm Au/11 nm Ag ultrathin electrode, active layers with buffer layers. Reproduced with permission.<sup>[120]</sup> Copyright 2019, the Royal Society of Chemistry.

(100 nm)/ $\text{MoO}_3$  (5 nm)/Ag (15 nm), and realized PCEs of 2.93–8.91% with AVT of 11.1% to 14.7% and 7.98% to 11.1% with AVT of 11.7% to 13.9%, respectively at 350–750 nm for PTB7-Th:FNIC1 and PTB7-Th:FNIC2-based blends.<sup>[124]</sup>

Following the same trend, Min and co-workers recently reported the first ST-OSCs with record-high PCEs over 11.0% and AVTs of 21.69% (at 400–650 nm) created by blending a new chlorinated PD, J101 and ZITI acceptor with the device

architecture of ITO/PEDOT:PSS/J101:ZITI/Ag (15 nm).<sup>[48]</sup> The structure of ZITI consists of a new rigid octacyclic dithienocyclopentaindendene core as the central “D” unit and terminal F-DCI units.<sup>[125]</sup> The main absorption of ZITI film is located at 700 to 810 nm with a corresponding  $E_g$  of 1.53 eV, which is complementary to J101, so the device covers a broad absorption. Additionally, the optimized J101:ZITI blend also demonstrated well-matched energy level alignment, optimal morphology and efficient charge transport with lower recombination loss, thereby justifying the high PCEs. Interestingly, these high PCE values despite the limited transparency of the window in the J101:ZITI system in the visible region, suggesting optimizing the thickness of the active layer is highly crucial for achieving a balance between PCE and AVT.

Like fluorination, chlorination of DCI units has also been extensively explored in NFA design because of inherent advantages of chlorine (Cl) atoms, such as higher electron acceptability due to the presence of empty 3d orbitals and the higher dipole moment of the C–Cl bond, which broadens absorption by inducing a stronger ICT effect.<sup>[30,96,126–128]</sup> Furthermore, the synthesis of chlorinated units is more facile and much cheaper when compared to the synthesis of their fluorinated counterparts, signifying the enormous potential for commercialization of OSCs.<sup>[92,96,126,129]</sup> Based on this molecular design approach, Forrest and co-workers further explored the possibility of employing a newly synthesized NIR-absorbing NFA, BT-CIC, composed of a central electron-donating BDT core flanked by two adjacent dichlorinated-DCI (2Cl-DCI) units, for use in ST-OSCs.<sup>[127]</sup> Indeed, insertion of two Cl substituents 5,6-positions of DCI units significantly favored down-shifting of the HOMO/LUMO energy levels, leading to stronger and red-shifted absorption ranging from 600–930 nm with a narrow  $E_g$  (1.33 eV) in BT-CIC. By blending with PTB7-Th and tailoring the thickness of the Ag (10–20 nm) cathode, the authors successfully realized a transparency window in the visible region, which led to the creation of efficient ST-OSCs with high PCEs of 7.1–8.2% and AVTs of 43–26%. Furthermore, ST-OSCs with 10 nm thick Ag showed color coordinates of (0.29, 0.32) with corresponding CRI = 91 and CCT = 7784 K, close to standard daylight, indicating that the color of the light passing through these ST-OSCs is not much different from natural light, though it has a slightly bluish tint. Thus, a combination of factors, such as effective NIR harvesting of the solar spectrum, well-ordered molecular packing, and the low resistance of Ag led to this impressive performance.

Li et al. reported a new NIR absorbing NFA unit, ID-4Cl, by inserting 2Cl-DCI units as terminal “A” units in the IDIC acceptor core.<sup>[130]</sup> Because of the stronger ICT effect between the central “D” unit and the 2Cl-DCI units, ID-4Cl showed the main absorption in the NIR region (500–900 nm) with a reduced  $E_g$  of 1.51 eV. The authors fabricated both small-area and large-area ST-OSCs (active layer of 4 mm and 1 cm<sup>2</sup>, respectively) by using a device architecture of ITO/PEDOT:PSS/PM-6-ID-4Cl/PDINO/Au (15 nm), and optimized devices displayed the highest PCEs of 6.99% and 1.1%, respectively.

Recently, Li and co-workers fabricated ST-OSCs featuring trifluorinated PBFTT as a donor and LBG tetrachlorinated IT-4Cl ( $E_g$  = 1.43 eV) as an acceptor to achieve a remarkable PCE of 9.1% with an AVT of 27.6% and optical perception for ST-OSCs

using a 20 nm thick Au as cathode; this is the new record for as-cast ST-OSCs without any post-treatment (Figure 4g–i).<sup>[119]</sup> Because of the halogen effect, both of these active layer materials showed stronger molar absorptivity enhanced crystallinity and carrier mobility. Also, PBFTT and IT-Cl exhibited complementary absorption profiles in the NIR region and leaving behind a transparency window in the visible region. Thus, well-matched energy levels, a broad photo absorbance region with high EQE values from 600 to 830 nm and optimal morphology led to these excellent performances. Also, to test the compatibility of the PBFTT:IT-4Cl system with large-area roll-to-roll processes, the authors fabricated ST-OSCs with an active area of 1.00 cm<sup>2</sup> and realized a notable PCE of over 7% with a high AVT (27.6%).

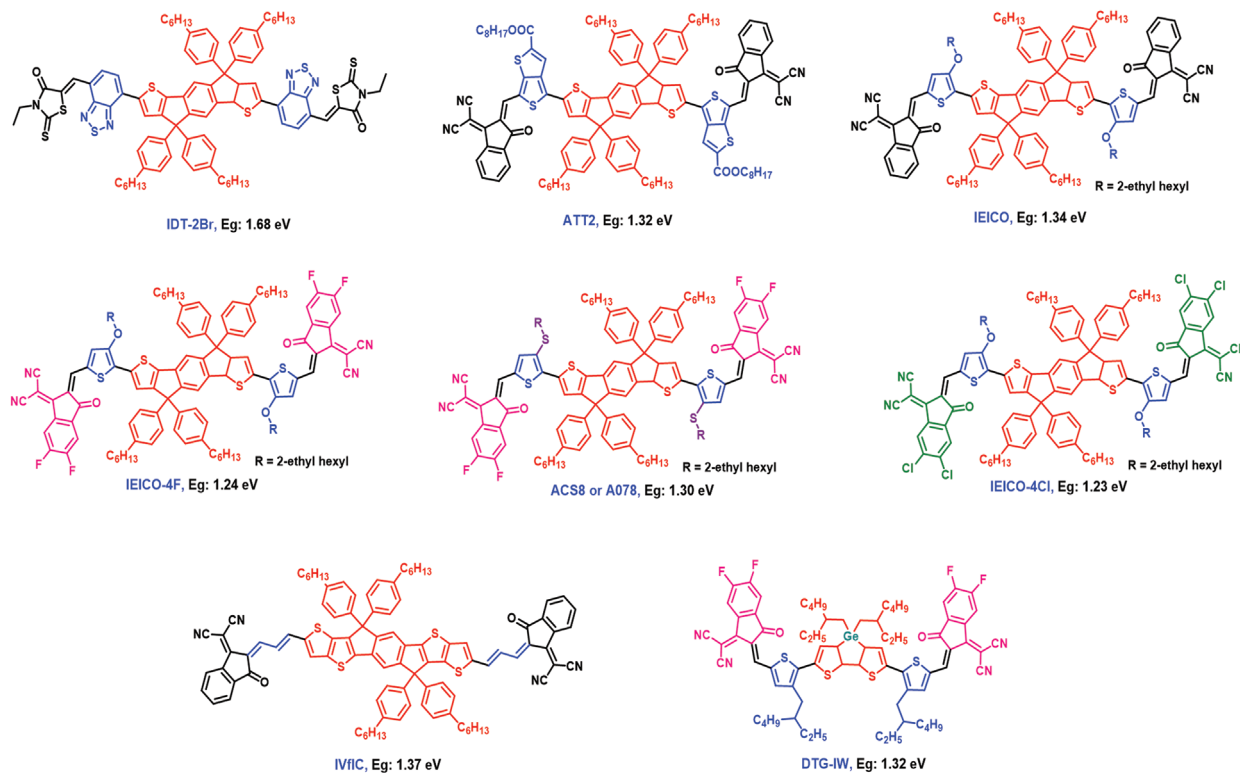
Wang et al. reported a new NFA, PTTtID-Cl, with hexacyclic pyrrole-based DTPTt as a central donor and 2Cl-DCI as peripheral end groups.<sup>[131]</sup> Due to the delocalization of nitrogen lone pair along the backbone, DTPTt exhibits stronger electron-donating ability and extended  $\pi$ -conjugation. Moreover, originating from the attachment of only one alkyl sidechain on the sp<sup>2</sup>-hybridized N atom, PTTtID-Cl also shows stronger intermolecular interactions. Consequently, PTTtID-Cl displayed extended NIR absorption from 700 to 1000 nm due to the stronger ICT effect with 2Cl-DCI units and minimized steric repulsion along the backbone. When mixed with PTB7-Th, ST-OSCs based on the PTB7-Th:PTTtID-Cl blend with an inverted device structure of ITO/ZnO/PTB7-Th:PTTtID-Cl/MoO<sub>3</sub>/Ag (20 nm) produced a PCE of 7.7% with an AVT of 16.7%. Moreover, the authors also fabricated various colorful ST-OSCs by implementing the Ag/ITO/Ag microcavity structure which is discussed in section 5.1.

Introduction of a  $\pi$ -spacer in the “A–D–A” molecular design to form “A– $\pi$ –D– $\pi$ –A”-type NFAs is also extensively used method to extend  $\pi$ -conjugation and tuning of photochemical properties and solubility via introduction of heteroatom or drafting of appropriate soluble alkyl chains on these units.<sup>[30,38,86,120,133]</sup> Moreover, these  $\pi$ -spacer units can also have additional benefits, such as increasing charge transport by improving coplanarity and solid-state packing via non-covalent intramolecular confirmation locks and lower synthetic complexity when compared to highly conjugated fused ring cores.<sup>[30,141–144]</sup> Commonly, electron-rich units such as thiophene, selenophene, or benzene derivatives with various substitutions or electron-deficient units such as benzothiadiazole (BT)/ester-substituted TT/thiazole are commonly used as these  $\pi$ -spacers. **Figure 5** shows the structures of such “A– $\pi$ –D– $\pi$ –A”-type NFAs which have been used to fabricate ST-OSCs.

In 2015, Wu et al. reported an IDT-2BR acceptor with central IDT and terminal ethyl -rhodanine end groups interconnected by a BT-spacer.<sup>[145]</sup> This acceptor has an absorption in the 300–750 nm region with a medium  $E_g$  of 1.68 eV. It was the very first NFA unit used to prepare ST-OSC devices. Wang et al. used this IDT-2BR to fabricate ST-OSCs by blending with a P3HT donor.<sup>[132]</sup> These devices displayed a low PCE of 3.22%, mainly due to the strong absorption of the blend in the visible region.

Under the premise of effectively exploiting the NIR region and transmitting visible light, Liu et al. synthesized ATT-2, in which a TT acceptor unit is flanked between central IDT and

### A-( $\pi$ )-D-( $\pi$ )-A type NFAs with different $\pi$ -spacers



### A-DA'D-A-type (Y-class) NFAs

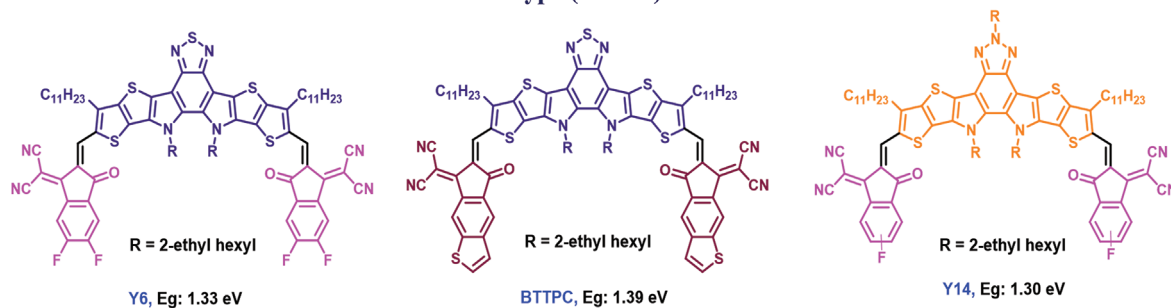


**Figure 5.** Molecular structure of “A-( $\pi$ )-D-( $\pi$ )-A” and “A-DA'D-A” type NFAs used in ST-OSCs.

terminal DCI end groups. Owing to the stronger ICT effect, ATT-2 exhibits higher absorptivity and enhanced absorption up to 600–940 nm ( $E_g = 1.32$  eV).<sup>[133]</sup> Combined with PTB7-Th, the authors successfully pushed the absorption of the active layer blend up into the NIR region; hence, PTB7-Th:ATT-2-based ST-OSCs devices achieved PCEs as high as 7.74% with AVTs of 37% using an ultrathin Ag (20 nm) electrode. Moreover, these devices had good CIE color coordinates of (0.2805, 0.3076), a CCT of 9113 K, and a respectable CRI of 94.1, emphasizing that these devices can transmit color accurately.

Hou and co-workers reported IEICO by switching the alkyl-substituted thiophene spacer in IEIC with an alkoxy-thiophene unit.<sup>[38]</sup> Owing to the noncovalent S...O interaction between

the central IDTT and adjacent alkoxy-substituted thiophene spacer, the authors achieved high coplanarity and extended  $\pi$ -conjugation, which ensuing strong NIR absorption with an absorption edge in the thin film state located at  $\approx 925$  nm ( $E_g = 1.34$  eV). Meanwhile, because of the introduction of alkoxy-thiophene, IEICO showed slightly higher HOMO and similar LUMO values than IEIC. Combining these unique properties of IEICO with complementary absorbing PBDTTT-ET, Sun et al. fabricated ST-OSCs which yielded the best PCE of 9%, with a high  $J_{sc}$  of  $16.3$  mA cm<sup>-2</sup> and AVT of 17% via efficient NIR photon harvesting.<sup>[38]</sup> To maximize heat insulation without affecting optical or power generation characteristics, the authors further introduced four-layer DBR materials on the

Ag electrode, resulting in selective improvement of transmittance in the visible region while maintaining high reflectance at NIR wavelengths. These ST-OSC devices generated PCEs of over 7%, with an AVT and IRR of 26.2% and 80.6%, respectively.

In a follow-up study, the same group further optimized the structure of IEICO by substituting DIC end groups with stronger electron-withdrawing 2F-DIC units to obtain an IEICO-4F acceptor unit.<sup>[102]</sup> Because of the synergistic effects of extended  $\pi$ -conjugation length and the stronger ICT effect rendered by the insertion of 2F-DIC units, IEICO-4F had an extremely narrow  $E_g$  of 1.24 eV, with absorption onset located at 1000 nm in the NIR region (0.1 eV lower than IEICO) for effective NIR light-harvesting. Consequently, Hu et al. produced ST-OSC devices that mix IEICO-4F with PTB7-Th (1.2:1.5, wt/wt) showed an impressive  $J_{sc}$  of 20.59 mA cm<sup>-2</sup> and PCE of  $\approx$ 9.5%, with an AVT of 23.7% using a smart strategy by reducing WBG-PD content in the active layer.<sup>[120]</sup> The neat PTB7-Th has the main absorption peak located at 700 nm, which is complementary to the NIR-absorbing IEICO-4F (Figure 4j). Therefore, by lowering the PTB7-Th content in the IEICO-4F:PTB7-Th blend, the authors simultaneously decreased photon harvesting in the visible region and improved NIR photo-harvesting, which aided in realizing the superior balance between PCE and AVT (Figure 4k,l). Lee et al. also reported ST-OSCs based on DPP-based donor DPP2T and IEICO-4F.<sup>[134]</sup> These devices showed high transmittance (AT reaching  $\approx$ 60% at 400–600 nm) but a poor PCE of 5.7% due to the uncomplimentary absorption profiles of DPP2T and IEICO-4F, which hampered a trade-off between PCE and AVT.

Generally, in BHI ST-OSCs, which consist of a blend comprising medium bandgap (MBG) polymer as a “D” unit and NIR-absorbing “A” units, the increase in blend thickness will often decrease the trade-off between PCE and transmission due to enhanced absorption by the “D” unit in the visible region. To overcome this issue, Song et al. selectively varied the thickness of each component in the PTB7-Th:IEICO-4F blend by fabricating the ST-OSCs devices with bilayer architecture (Figure 6a) and systematically evaluated their effects on photovoltaic parameters of ST-OSCs.<sup>[135]</sup> Interestingly, by increasing the thickness of only IEICO-4F (50–80 nm) with NIR absorption (vs fixed 60 nm of PTB7-Th), the authors improved the PCE of ST-OSCs from 7.9% to 8.4% with a slight decrease AVT from 21.3% to 20.4%, which is higher than parent binary BHI devices based on the same blend system (maximum PCE of 8.1% and AVT of 21.1% for 110 nm) compared parallelly (Figure 6b,c). Though this method has simplified device optimization, it must be noted that the appropriate selection of different solvents for dissolving each component of the blend is crucial to prevent washing-off the “D” unit during deposition.

Recently, Chen et al. replaced the alkoxy-thiophene linker in IEICO-4F with alkylthio- thiophene to get ACS8.<sup>[136]</sup> Due to the strong aggregation of alkylthio-alkyl chains in the solid state, ACS8 possesses absorption in the NIR region with an  $E_g$  of 1.3 eV (0.6 eV higher than IEICO-4F). Moreover, resulting from favorable molecular orientation with compact  $\pi$ - $\pi$  stacking, ACS8 also showed good  $\mu_e$  of  $2.65 \times 10^{-4}$  cm<sup>2</sup> V<sup>-1</sup> s<sup>-1</sup> (vs  $1.14 \times 10^{-4}$  cm<sup>2</sup> V<sup>-1</sup> s<sup>-1</sup> of IEICO-4F). Hence, high PCE values (9.4–11.1%) with different AVTs (43.2–28.6%) was achieved for PTB7-Th:ACS8-based ST-OSC device with a device structure of ITO/ZnO/PFN/active layer/MoO<sub>3</sub>/Au/Ag and by modifying

the Ag thickness. Likewise, Forrest and co-workers independently also reported ACS8 (named as A078).<sup>[68]</sup> To understand the effect of alkylthio-alkyl side chains, the authors compared the absorption spectra of A078 (with partially fused core) with its fully fused counterpart SBT-FIC. Surprisingly, A078 showed much remarkable bathochromic shift with compact molecular packing than SBT-FIC, thus signifying that noncovalent S $\cdots$ S interactions can facilitate the planarization and rigidification of  $\pi$ -conjugated structure, leading to narrowing of  $E_g$ . They exploited the compatibility of ACS8 with ST-OSCs due to its visible transparency window. The best ST-OSCs devices with ITO/ZnO /PCE-10:A078 (95 nm)/MoO<sub>3</sub> (20 nm)/Ag (16 nm) realized the PCE of 11.0% with 25% AVT and LUE of 2.8%. Later, to solve the discrepancy between PCE and AVT, the authors deposited a 4-layered outcoupling (OC) coating on the Ag anode followed by bilayer anti-reflective coating on the glass substrate. Impressively, these optical engineering methods yielded around 80% AVT enhancement from 25.0% to 45.7% with a slight drop in the PCE to 10.8%, and record-high LUE values of  $\approx$ 5% for ST-OSCs.

In another instance, Hou and co-workers constructed a series of ST-OSCs based on an ultralow bandgap IEICO-4Cl acceptor (with  $\lambda$  onset of 1010 nm and  $E_g = 1.23$  eV) and different PDs (J52, PBDB-T, and PTB7-Th).<sup>[30]</sup> The main absorption band and a peak of IEICO-4Cl are located at 750–950 and 802 nm, respectively, which is out of the visible region, hence useful for the fabrication of ST-OSCs. Thus, the authors fabricated three colorful devices by mixing IEICO-4Cl with different donor polymers with different absorption profiles. Among these green colored PTB7-Th:IEICO-4Cl blend produced the best PCE of 8.38% with an AVT of 25.6%.

To further improve the performance of ST-OSCs by tuning of light absorption, Huang et al. synthesized an ST-OSCs based on the blend system of PTB7-Th and a NIR-absorbing ITVfIC acceptor ( $E_g = 1.37$  eV), which exhibited an AVT of 73.46% in the absorption region of 400–600 nm with an active layer thickness of 100 nm.<sup>[137]</sup> Unlike traditional NFAs, the structure of ITVfIC has an additional vinyl linker as a  $\pi$ -spacer between the central IDT core and terminal F-DCI units. The absorption profile of the PTB7-Th:ITVfIC blend lies in the maximum photon flux density region of the solar spectrum (600–900 nm), and is thus beneficial for the fabrication of ST-OSCs. Therefore, optimized as-cast ST-OSCs with a device structure of ITO/PEDOT:PSS/PTB7-Th:ITVfIC (100 nm)/PDINO/Ag (15 nm) delivered a good PCE of 8.21% and an AVT of 26.40%. Besides, the authors investigated the preliminary thermal stability of these ST-OSC devices by exposing the devices to 200 °C for 2 h. The devices retained 91% of their original PCE values, thus emphasizing their potential value for real-world applications.

Yang and co-workers reported two new isomeric NBG-NFAs based on a germanium (Ge)-fused heterocyclic dithienogermole central donor and terminal 2F-DCI units interconnected by a 2-ethyl hexyl substituted thiophene unit with a different orientation of alkyl chains position, i.e., DTG-IW (inward facing) and DTG-IW (outward facing).<sup>[138]</sup> Though both of these NFAs had similar  $E_g$  values of  $\approx$ 1.3 eV, the GIWAXS study revealed that DTG-IW contains highly confined “face-on” crystallites in the solid state, which might be useful for boosting charge separation and transport in the corresponding devices. Optimized

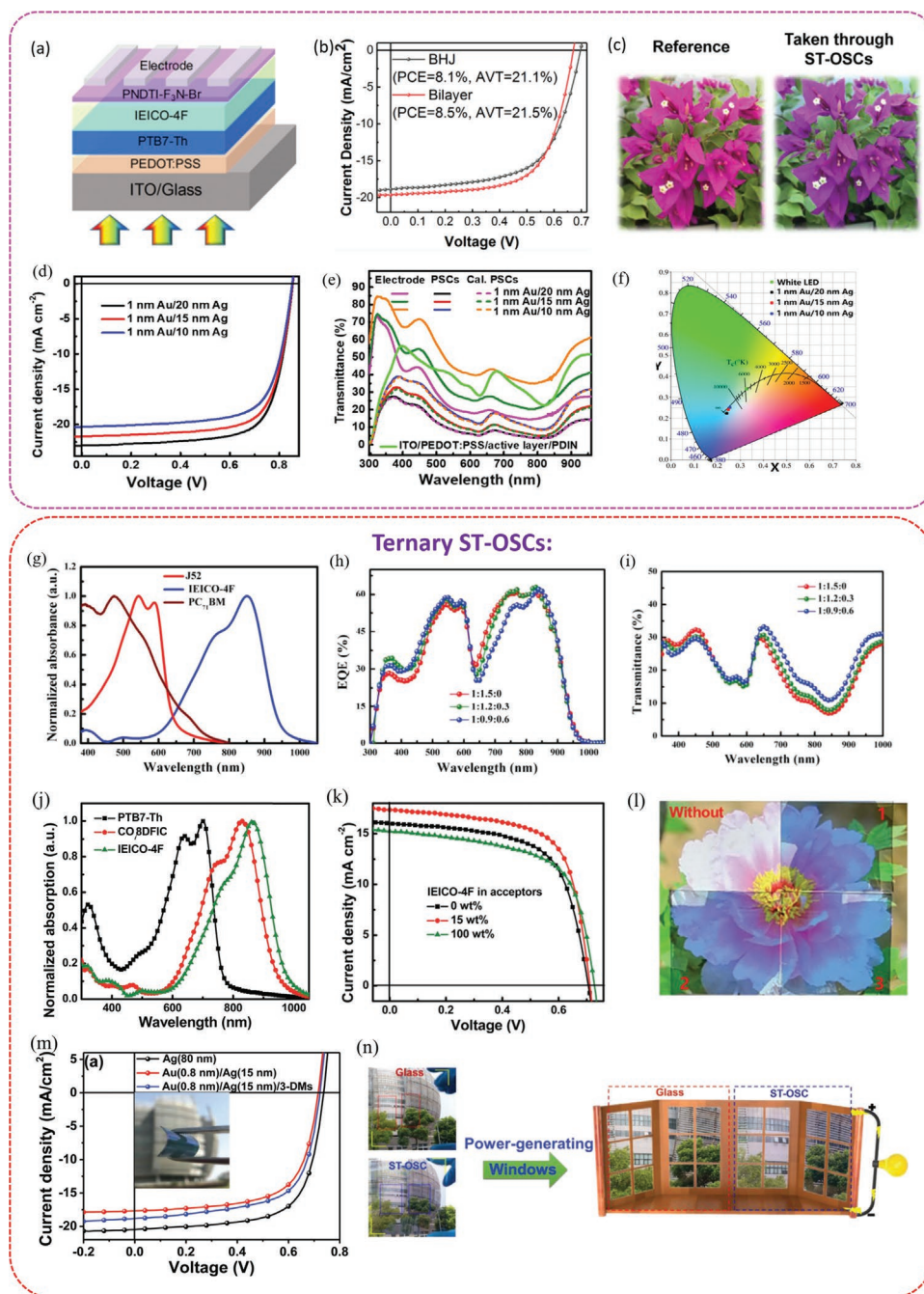


**Figure 6.** a) Schematic diagram of PTB7-Th:IEICO-4F-based ST-OSCs based on fabricated by sequential bilayer technique; b)  $J$ - $V$  curves of optimized ST-OSCs fabricated with BHJ and bilayer techniques; and c) Photographs of the flowers without and with bilayer ST-OSCs. Reproduced with permission.<sup>[135]</sup> Copyright 2020, American Chemical Society; PM6:Y6-based ST-OSCs with PCE over 12%: d)  $J$ - $V$  curves; e) Transmission spectra; f) Representation of the corresponding color coordinates on the CIE chromaticity diagram; Reproduced with permission.<sup>[47]</sup> Copyright 2020, Elsevier Inc.; Ternary ST-OSCs: g) Normalized absorption spectra of neat J52, IEICO-4F, and PC<sub>71</sub>BM; h) EQE and i) Transmission spectra of the various J52:IEICO-4F:PC<sub>71</sub>BM-based ST-OSCs with different blend ratio. Reproduced with permission.<sup>[26]</sup> Copyright 2018, Wiley-VCH.; j) Normalized absorption spectra of neat films of PTB7-Th, CO<sub>8</sub>DFIC, and IEICO-4F; k)  $J$ - $V$  curves of ternary ST-OSCs with different amount of IEICO-4F as the third component in PTB7-Th:CO<sub>8</sub>DFIC blend with 15 nm of Ag as the electrode and l) Images of flower partially covered by with 1) PTB7-Th:CO<sub>8</sub>DFIC (binary); 2) PTB7-Th:CO<sub>8</sub>DFIC:IEICO-4F (ternary) and 3) PTB7-Th:IEICO-4F (binary) as the active layers. Reproduced with permission.<sup>[146]</sup> Copyright 2018, the Royal Society of Chemistry and PBDB-T:PTB7-Th:IHIC-based ternary flexible devices: m)  $J$ - $V$  curves with different top electrodes (Inset: side view of flexible ST-OSC with 3-DMs) and n) Digital photographs of doctor-blade coating J71:PTB7-Th:IHIC-based ternary ST-OSCs and glass counterparts. Right: Used as glass applied to the windows. Reproduced with permission.<sup>[147]</sup> Copyright 2019, Wiley-VCH.



ST-OSCs based on PTB7-Th:DTG-IW blends (green-tinted color) and semitransparent Ag/Sb<sub>2</sub>O<sub>3</sub>/Ag electrodes delivered the best PCE of 6.19% and AVT of 50.4% at 500–540 nm.

Since Zou and co-workers designed and developed the “Y-series” NFAs based on fused benzothiadiazole with “A-DA’D-A”-type molecular design, in 2019,<sup>[104]</sup> a new revolution has been created amongst the OSC research community because OSCs such type of Y6 acceptor core devices broke the PCE threshold barrier, 15% when blended with PM6 donor.<sup>[104]</sup> Relative to parent A-D-A type NFAs, the new Y6 acceptor core with a central fused ring (dithienothiophene[3,2-*b*]-pyrrolobenzothiadiazole) with a benzothiadiazole (BT) and terminal 2F-DIC end groups possesses several structural superiorities. In particular, the inclusion of an electron-deficient benzothiadiazole (BT) unit in the central fused core can further enhance D-A interactions, leading to higher  $\mu_e$  and molecular aggregations. Moreover, a pyrrole-bridging unit with a high electron-donating nature can act as a “D” unit for this  $\pi$ -conjugated system yields the narrow  $E_g$  of 1.33 eV due to the upshift of the HOMO energy level. Also, the presence of alkyl chains on the pyrrole core restricts the severe aggregation because of their steric effect, thus allowing the facile control over solubility and molecular ordering. Consequently, Y6 core has been evolved as one of the most successful electron acceptors for OSCs owing to the strong electron affinity, good molecular aggregation, high  $\mu_e$  and NIR-absorption properties, and PCEs up to 15–18% have been realized by continuous innovation in the molecular design of Y6 and other Y-class NFAs.<sup>[10,13,18,104,148–150]</sup> Hu et al. were the first to synthesize ST-OSCs by employing Y6 as an EA core and complementary absorbing PM6 as an ED unit owing to the excellent AVT of 50.5% of this blend system with a thickness of 100 nm.<sup>[47]</sup> Hence, the authors fabricated ST-OSCs based on a conventional device structure with 1 nm Au and Ag (20 nm) as the cathode. These devices set a world record for ST-OSC PCE value, i.e., 14.2%, with corresponding photovoltaic parameters of high  $J_{SC} = 23.01 \text{ mA cm}^{-2}$ ,  $V_{OC} = 0.854 \text{ V}$ , FF = 72.27%, and AVT of 8.9% (Figure 6d–f). As the performance of ST-OSCs was always evaluated by the superior trade-off between PCE and AVT, they further optimized the thickness of the Ag electrode to improve the balance between these two parameters. Hence, a device with a 10 nm Ag electrode demonstrated an impressive PCE of 12.37% along with an enhanced AVT of 18.6%. Furthermore, the photon utilization efficiency of these ST devices was estimated by measuring the QUE. Notably, these devices showed maximum QUE values only up to 82%, signifying that the PCEs of these devices could be further improved by refining these values, either by more effective photon harvesting and/or minimization of carrier losses. Through a fibril network strategy, Sun and co-workers attempted to simultaneously realize high PCE and AVT in ST-OSCs by employing WBG, PBT1-C-2Cl, and Y6 as “ED” and “EA” units.<sup>[49]</sup> They found that PBT1-C-2Cl has a unique ability to transform itself into fibrillar nanostructures and thus the addition of a small amount of PBT1-C-2Cl drastically leading to enhanced  $\mu_h$  in the blend by forming charge pathways, along with the enhancement of visible transmittance. Besides, Y6 can ensure NIR light-harvesting to enhance the  $J_{SC}$  of the devices. Thus, optimized ST-OSCs based on the inverted structure of ITO/ZnO/PBT1-C-2Cl:Y6 (1:1, wt/wt)/MoO<sub>3</sub> (3 nm)/Au (12 nm)

established a remarkable PCE of 11.7% with an AVT of 19.7%. Furthermore, by reducing the PBT1-C-2Cl polymer donor content, which mainly absorbs light in the visible region, they also produced an excellent AVT of 40.1% with a slight drop in the PCE to 9.1% for the PBT1-C-2Cl:Y6 (0.25:1, wt/wt) blend. Later, Ge and collaborators developed flexible ST-OSCs by replacing ITO with poly(3,4-ethylenedioxythiophene):modified polystyrene sulfonate (PEDOT:PSS) (served as the flexible TE) and PBDB-T-2F:Y6 acted as the photoabsorbent layers.<sup>[50]</sup> These devices produced PCEs over 12% with AVTs of 17% because of the favorable photophysical properties of the modified PEDOT:PSS layer in the visible region and the strong photosensitivity of the PBDB-T-2F:Y6 blend in the NIR region. Also, these devices showed excellent mechanical stability against bending and folding, retaining >80% of the initial PCE after 1000 bending cycles, suggesting their potential for flexible photovoltaics.

Luo et al. reported a new NIR absorbing NFA, namely Y14 with fused dithienothiophene[3,2-*b*]-pyrrolobenzotriazole as “D” core and terminal two 2F-DCI units.<sup>[139]</sup> Y14 displayed an extended absorption range from  $\approx 600$  to 920 nm with a narrow  $E_g$  of 1.3 eV and high  $\mu_e$  because of the relatively planar backbone with strong  $\pi$ -conjugation, thereby facilitating effective delocalization of  $\pi$ -electrons. Moreover, the presence of alkyl chains in the central donor core further improves the solubility and helps in overcoming the excessive self-aggregation of Y14. The authors fabricated inverted ST-OSCs with a device structure of ITO/SnO<sub>2</sub>/active layer/MoO<sub>3</sub>/Ag and recorded a PCE of 12.67% with AVT of 23.69% using PBDB-T:Y14 blend.

Pascual-San-Jose et al. reported the scalable fabrication of ST modules featuring PD, PBDB-T-2F:Y6 and NIR absorbing 4TICO acceptor using a large-scale-compatible laser-patterning method.<sup>[140]</sup> The ST-OSC devices were fabricated in the air with an eco-friendly solvent using the blade coating method and no evaporation steps, where these blends showed PCEs as high as 4.7% with 20% AVT. The authors also produced ST-OSC modules using laser-patterning, resulting in PCEs of 4% (active area, 1 cm<sup>2</sup>) with over 30% human perception transmittance and geometrical FF values of >90%, along with the narrowing of the interconnection length of the module to 300  $\mu\text{m}$ . Besides, the optimized geometry of the modules and the quality of interconnection between the cells of these devices were evaluated using advanced co-local optoelectronic imaging techniques. Thus, these results offer valuable technical knowledge for the preparation of large-scale ST-OSC modules with low manufacturing costs.

Overall, the narrowing of the  $E_g$  (via either expanding the central fused-ring core or incorporation of strong electron-withdrawing end groups) is presently the easiest approach to be incorporated to effectively harvest NIR photon of the solar spectrum without losing visible transparency. On the other hand, finding suitable ED with complementary absorption, and more comparable and well-matched energy levels to minimize the driving force and preferably reduce the loss of radiative recombination during absorption is another effective way to enhance PCEs by exploiting the trade-off between  $J_{SC}$  and  $V_{OC}$ . Thus, every recent achievement in high-productive single-junction binary ST-OSCs has been set off by the fast

advancement of NIR-absorbing NFAs and these materials also have been used in the fabrication of highly efficient ternary ST-OSCs and multifunctional ST-OSCs as discussed below in the next sections.

#### 4. Ternary ST-OSCs

To broaden photon harvesting range and optimize morphology of active layer, a ternary blend strategy also has been extensively explored by adding a third component into the binary blend, which yielding excellent PCEs in recent years.<sup>[16–17,151–158]</sup> The main function of the guest component is to broaden the photoresponse range and manipulate morphology, thereby leading to enhanced performance by improving  $J_{sc}$  and FF in the corresponding devices. Thus, compounds with complementary absorption and cascade energy levels alignment with the host D-A components are preferred as a third component.<sup>[151–157,159]</sup> Meanwhile, these materials should not hamper visible transmittance (AVT) and color perception; this is an additional requirement applicable to the use of these materials in ternary

ST-OSCs. Recently, many research groups achieved impressive photovoltaic performance using ternary ST-OSCs, as summarized in **Table 3**.

By inserting PC<sub>71</sub>BM as a third component in the J52:IEICO-4F host system, Cao and co-workers presented wavelength-selective ternary ST-OSCs, which are useful for the promotion of plant growth in greenhouses.<sup>[26]</sup> The normalized absorption profiles of pristine J52, IEICO-4F, and PC<sub>71</sub>BM were shown in Figure 6g. The absorption peaks of the PC<sub>71</sub>BM is located at  $\approx 480$  nm, resulting in complementary with J52:IEICO-4F blend. Therefore, the authors systematically optimized the photo harvesting abilities and transmittance of the blend films for ST-OSCs by tailoring the concentration blend components (Figure 6h,i). Consequently, a high PCE of 7.75% 19.9% AVT and a defined crop growth factor of 24.8% were realized for optimal ternary ST-OSCs based on a J52:IEICO-4F:PC<sub>71</sub>BM (1:0.9:0.6 wt/wt) blend due to the minimized trap-assisted charge recombination, enhanced charge extraction and improved Voc caused by the addition of PC<sub>71</sub>BM in the host blend.

Sun and co-workers fabricated ternary ST-OSCs involving WBG-PD, PBT1-S ( $E_g = 2.1$  eV) as the third component in the

**Table 3.** Photovoltaic and optical parameters of ST-OSCs based on ternary structures and various colorful ST-OSCs with aesthetic appeals.

Blend	V <sub>oc</sub> [V]	J <sub>sc</sub> [mA cm <sup>-2</sup> ]	FF [%]	PCE [%]	AVT [%] <sup>a)</sup>	CRI <sup>b)</sup> @ CCT/ CIE (x, y) <sup>c)</sup>	Ref.
Ternary ST-OSCs					AVT <sup>a)</sup> /TMax <sup>b)</sup> [%]	CRI <sup>c)</sup> @ CCT <sup>d)</sup> /CIE (x, y) <sup>e)</sup>	
J52:IEICO-4F:PC <sub>71</sub> BM	0.685	16.90	66.9	7.75	19.9	-(0.317, 0.283)	[26]
PTB7-Th:PBT1-S:PC <sub>71</sub> BM	0.83	15.6	70.8	9.2	20	- @ 7366 K (0.2976, 0.3283)	[160]
PCE10:ICBA:Y8	0.738	20.66	68.61	10.46	26.56		[161]
PTB7-Th:COi8DFIC: IEICO-4F	0.712	17.35	66.65	8.23	20.78		[146]
PTB7-Th:BDTThIT-4F:IEICO-4F	0.728	19.21	67.2	9.40	24.6		[162]
PBDB-TF:Y6:BTTPC	0.86	20.63	0.74	13.1	22.4		[35]
J71:PTB7-Th:IHIC	0.76	21.08	58.05	9.37	21.4		[147]
PBDB-T:PTB7-Th:IHIC	0.73	18.37	65.78	8.76	20.6		[147]
ST-OSCs for aesthetic applications							
J52:IEICO-4Cl	0.673	17.2	55.1	6.37	35.1		[30]
PBDB-T:IEICO-4Cl	0.724	15.4	56.0	6.24	35.7		[30]
PTB7-Th:IEICO-4Cl	0.725	19.6	59.0	8.38	25.6		[30]
PTB7-Th:IEICO-4F	0.713	19.52	62.76	8.74	25.08	89.1 @ -/(0.3024, 0.3531)	[31]
PBDB-T:IEICO-4F	0.711	17.85	52.30	6.64	26.50	94.4 @ -/(0.2628, 0.2941)	[31]
PBDB-T-2F:ITIC-4F	0.789	19.74	71.92	11.20	26.22	97.5 @ -/(0.2555, 0.2666)	[31]
PBDB-T-2F:Y6	0.825	21.56	72.41	12.88	25.60	97.6 @ -/(0.2436, 0.2518)	[31]
PTB7-Th:IEICO-4F	0.707	20.27	67.4	9.66	34.2		[27]
PTB7-Th:FOIC	0.756	17.82	65.2	8.86	31.0		[27]
PTB7-Th:F8IC	0.687	18.97	66.7	8.69	34.3		[27]
PM6:Y6	0.85	22.6	76.0	14.60	T <sub>Max</sub> of 21.8 @ 529 nm	-(0.209, 0.475)	[34]
PM6:N3:PC <sub>71</sub> BM	0.865	22.83	76.29	15.07	T <sub>Max</sub> of 25.79	99.31 @ -/(0.16, 0.02)	[33]
PTB7-Th:PC <sub>71</sub> BM	0.787	17.05	66.6	8.93	T <sub>Max</sub> of 25.7 @ 592 nm		[32]
PTB7-Th:PTTtID-Cl:IT-4F	0.80	17.2	63.1	8.7	T <sub>Max</sub> of 26.4 @ 459 nm		[131]

<sup>a)</sup>AVT = average of the transmittance of the solar cells in the visible region (370–740 nm); <sup>b)</sup>T<sub>Max</sub> = maximum transmittance; <sup>c)</sup>color rendering index (CRI); <sup>d)</sup>Corresponding color temperature (CCT); <sup>e)</sup>and CIE (x, y) = color coordinates derived from CIE 1931 chromaticity diagram.

PTB7-Th:PC<sub>71</sub>BM blend.<sup>[160]</sup> The optimized ternary devices with a device structure of ITO/PEDOT:PSS/PTB7-Th:PBT1-S:PC<sub>71</sub>BM (0.9:0.1:1.5, wt/wt)/ZrAcac/Ag (15 nm) displayed an excellent PCE of 9.2% with an AVT of 20%, which represents a better performance than seen in the host PTB7-Th:PC<sub>71</sub>BM binary devices (PCE and AVT of 8.0% and 20.8%, respectively). The enhancement in PCE value was credited to improved light absorption, favorable morphology and higher carrier mobility enabled by PBT1-S, resulting a higher  $J_{sc}$  and FF.

Zhu et al. introduced indene-C<sub>60</sub>bisadduct (ICBA) as the third component to enhance the performance of the PCE10:Y8 blend system.<sup>[161]</sup> ICBA has complementary absorption and a well-aligned energy level that match the PCE10:Y8 blend. The optimal ternary ST-OSC devices with PCE10:ICBA:Y8 (1:0.3:1.2 wt/wt) delivered impressive PCE and AVT values of 10.46% and 26.56%, respectively, which is ≈9% higher than the values of the parent PCE10:Y8 blend system (9.57%). Along with a high  $J_{sc}$  of 20.66 mA cm<sup>-2</sup> and an increase in  $V_{oc}$  from 0.71 to 0.738 V due to the broad absorption region and higher LUMO energy level of ICBA, the ternary devices also displayed improved FF due to the amorphous nature of ICBA, thereby explaining the enhanced PCEs. Moreover, the authors also realized promising PCE values of 9.52% for ternary ST-OSCs devices fabricated using the blade coating method, which further emphasizes the compatibility of this blend system for large-area fabrication technology.

Unlike the commonly used strategy of employing a fullerene derivative as the third component, Zhang and co-workers introduced a complementary absorbing NIR acceptor, IEICO-4F, as the third component in the PTB7-Th:COi8DFIC blend (Figure 6j).<sup>[146]</sup> The authors fabricated a series of ternary ST-OSCs by optimizing the composition of the active layer and the thickness of the Ag electrode to achieve the best trade-off between transparency and performance. Thus, IEICO-4F enabled effective light-harvesting, favorable molecular arrangement, and morphology in the ternary blend, which in turn led to a promising PCE of 8.23% (AVT of 20.78%) in ternary ST-OSCs (Figure 6k,l). Likewise, Hu et al. used ultra-LBG IEICO-4F as a third component to tune the absorption and morphology of the PTB7-Th:BDTThIT-4F system.<sup>[162]</sup> The optimized ST-OSCs with a device structure of ITO/PEDOT:PSS/PTB7-Th:BDTThIT-4F:IEICO-4F (1.0:0.5:0.5, wt/wt)/PDIN/Au (1 nm)/Ag (10 nm) delivered a promising PCE of 9.40% with an AVT of 24.6% through improved photo-absorption and good charge transportability.

Recently, Li and co-workers developed highly efficient ternary ST-OSCs by inducting the newly synthesized BTTPC acceptor core into the PBDB-TF:Y6 blend system.<sup>[35]</sup> The structure of BTTPC shares a similar backbone with the Y6 acceptor core, but terminal DIC "A" units in Y6 were changed to benzo[b]thiophene in BTTPC. This change enabled further extension of conjugation and the reduction of the  $E_g$  (1.39 eV), without lowering the LUMO.<sup>[149]</sup> In addition to cascade energy level alignment favoring efficient charge transport, the introduction of a small amount of BTTPC (10 w%) into PBDB-TF:Y6 blend also resulted in enhanced  $\mu_h$  and minimized recombination due to the favorable morphology and molecular packing. As a result, BDB-TF:Y6:BTTPC based ternary ST-OSCs produced a remarkable PCE of 13.1% with AVT of

22.4%, IRR of 77% and significantly high  $J_{sc}$  of 20.63 mA cm<sup>-2</sup> because of effective photon utilization in the NIR region. Additionally, the authors fabricated multifunctional ST-OSCs having heat-reflecting capability by using optical engineering (discussed in Section 5.3).

Zhang et al. incorporated a NIR-absorbing IHIC acceptor with complementary absorption and favorable energy levels into an active layer containing two MBG PDs (J71:PTB7-Th or PBDB-T:PTB7-Th) to produce efficient ternary flexible ST-OSCs.<sup>[147]</sup> Indeed, the addition of IHIC helped to realize the flattened transmission in the visible region and enhancing the  $J_{sc}$  by effectively harvesting NIR photons (via its extended absorption range) in the ternary blends of J71:PTB7-Th:IHIC and PBDB-T:PTB7-Th:IHIC, which is useful for achieving a superior balance between PCE and AVT. Furthermore, the authors achieved superior color-rendering capacity and neutral color perception owing to the incorporation of 3-dielectric mirrors (3-DMs) with controlled reflected wavelength via optical engineering. Consequently, various colorful ST-OSCs with notable PCEs of ≈8.33–9.37%, AVTs over 20% and neutral color perception have been reported. Further, the authors successively tested the versatility of the same strategy on flexible substrates by replacing the ITO with a flexible transparent electrode poly(ethylene terephthalate) (PET)/Ag-mesh/PH1000). Remarkably, these flexible ST-OSCs devices based on J71:PTB7-Th:IHIC blend with 3-DM structure produced promising PCE of 8.76% with high AVT (20.6%) and CRI value (95) (Figure 6m). Moreover, the practical applicability of these ternary ST-OSCs with 3-DMs also evaluated by synthesizing large-area devices (10 cm × 10 cm) using doctor-blade coating and then fitting them on a glass window as shown in Figure 6n. Along with preserving the optical properties, these large-area devices also showed similar morphology, transmittance and color perception, when compared to devices coated by a spin-coating method. Overall, this study unveiled the versatile adaptability of ternary photoactive layer and DMs strategy for fabrication of ST-OSCs using different photovoltaic blend systems, various substrate types, and importantly large-area devices.

## 5. Multifunctional ST-OSCs

### 5.1. Colorful ST-OSCs

BIPV remains the first and most important choice as the main application of ST-OSCs. A BIPV acts as an integral part of a building; it can utilize a portion of sunlight to power harvesting-related activities and transmit the remaining light to brighten the interior of the building, thus enabling productive usage of renewable solar energy on vast areas, such as exterior walls or windows, fences, and parking roofs.<sup>[19–23]</sup> Hence, most of the above-discussed examples were designed to target BIPV applications. Though neutral-colored ST-OSCs are preferred for the see-through window applications, colorful ST-OSCs can be used in various other applications where aesthetics is preferred. In general, the color of an ST-OSCs is mainly dependent on the bandgap and absorption spectrum of photoabsorbent materials, therefore, the final color is easily tuned by modulating the bandgap using a facile molecular engineering approach or

through optical engineering in the device architecture. Hou and co-workers were the first to report various colorful ST-OSCs by simple chemical management of photoactive materials.<sup>[30]</sup> The authors successfully modulated light absorption spectrum and color (purple, blue, and green) by combing IEICO-4Cl acceptor with three different PDs (J52, PBDB-T, and PTB7-Th, respectively) with different  $E_g$ . As a result, ST-OSCs based on J52:IEICO-4Cl, PBDB-T:IEICO-4Cl, and PTB7-Th:IEICO-4Cl blended films yielded maximum PCEs of 6.37%, 6.24%, and 8.38%, respectively, with AVTs ranging from 33.5% to 35.7% (Figure 7a–c). Likewise, Bai et al. also used the same approach to produce various colorful ST-OSCs based on various combinations of PDs and NIR-absorbing NFAs (Figure 7d–f).<sup>[31]</sup> Using finite-difference time-domain (FDTD) and optical transfer matrix formalism (TMF) simulation methods, the authors successfully resolved the inconsistency between PCE and AVT, leading to high-efficiency of 4.45% to 12.88% with an AVTs of >25% in ST-OSCs with a semitransparent ultrathin SnO<sub>2</sub> cathode buffer layer between the active layer and Ag electrode. Among the various ST devices, those based on a PBDB-T-2F:Y6 blend (blue colored) produced excellent PCE (12.88%), 25.60% AVT and a CRI of 97.6. Also, Yang and co-workers reported a series of flexible ST-OSCs that employed poly(ethylene terephthalate)/Ag mesh/PEDOT:PSS (PH 1000)/ZnO as a flexible substrate and different donor and NFAs combinations, in which the final color relied on the bandgap of the active layer components.<sup>[27]</sup> Facilitated by strong NIR absorption and higher transmission in the IR and visible regions, optimized ST-OSC devices based on PTB7-Th:IEICO-4F, PTB7-Th:FOIC, and PTB7-Th:F8IC produced impressive PCEs of 9.66%, 8.86%, and 8.69%, respectively, with an AVT in all cases of over 30%. Moreover, the authors also tested these ST-OSCs for greenhouse applications, which are discussed in Section 5.2.

Other than tailoring a bandgap of photoactive materials, device optimization using optical management structure (photonic or microcavity structure)<sup>[53,163]</sup> was also a widely used method to adjust the colors in ST-OSCs using a fixed photoactive layer. As a couple of reviews already reported complete details of integration of such optical methods in ST-OSCs,<sup>[42,52–53]</sup> we discuss a few selected examples as below. Li et al. employed a device structure with a high-quality Fabry–Pérot (F–P) resonant microcavity embedded in electrodes.<sup>[34]</sup> Enabled by the optimized optical simulation, the resulted ST-OSCs based on the structure of glass/ITO/PEDOT:PSS/PM6:Y6/Bis-FIMG/Ag/TeO<sub>2</sub>/Ag displayed excellent color-tunability and produced a remarkable PCEs/ $T_{\text{Max}}$  of 14.04/31.0%, 14.60/21.8%, and 14.28/25.2%, respectively for blue, green and red devices. Overall, this study offers a new dimension to access ST-OSCs with vivid color using the single active layer materials.

To strike a balance between transparency and color purity, Tang and co-workers introduced a new Al:Ag/LiF/N,N'-bis(naphthalen-1-yl)-N,N'-bis(phenyl)benzidine (NPB)/carbon fluoride-based spectrally selective electrode (SSE) in ST-OSCs, which facilitated the effective transmission of selected light with a narrow bandwidth (Figure 7g).<sup>[33]</sup> Thus, the authors tuned the colors in ST-OSCs by varying the light coupling stacks in these SSEs. Compared to control devices with Al:Ag electrode (PCE of 13.69%), various colored ST-OSCs (violet to red) fabricated with a structure ITO/PEDOT:PSS/PM6:N3:PC<sub>71</sub>BM/PDINO/SSEs

demonstrated a superior PCE of 15.07% with  $T_{\text{Max}}$  29.70% and excellent color purity of 98.63% owing to the improved light absorption caused by enhanced reflection at opaque wavebands of SSEs (Figure 7h,i). Besides, these devices also demonstrated improved long-term stability attributed to the high light-reflecting and moisture resistance abilities of these SSEs.

Zhong et al. reported a new type of microcavity structure involving hybrid Au/Ag electrode and tungsten trioxide (WO<sub>3</sub>) as a mirror and spacer layer, respectively to afford colorful ST-OSCs with high  $T_{\text{Max}}$  (Figure 7j).<sup>[32]</sup> Promisingly, the authors could successfully tailor the color, transmittance and electrical performances of resulted ST-OSCs by simply varying the thickness of the WO<sub>3</sub> layer (Figure 7k,l). The optimized ST-OSCs fabricated with PTB7-Th:PC<sub>71</sub>BM as an active layer using this microcavity structure achieved the best PCE over 9% with  $T_{\text{Max}}$  > 25% at 592 nm.

To widen the scope of application of PTB7-Th:PTTtID-Cl-based ST-OSCs, Wang et al. also fabricated various ternary OSCs by introducing IT-4F as a third component and using Ag/ITO/Ag microcavities on top of the devices.<sup>[131]</sup> The authors fabricated various colorful devices by controlling the thickness of the ITO layer (blue (42 nm), green (68 nm), and red (94 nm)) using the microcavity structure and compared them with parent devices with the configuration of ITO/ZnO/active layers (~100 nm)/MoO<sub>3</sub> (5 nm)/Ag (20 nm). However, parent devices afforded the maximum PCE of 10.3% with the  $T_{\text{Max}}$  of 20.5% at 401 nm than other colorful devices on the same blend having microcavity structure (best PCE of 8.7% and  $T_{\text{Max}}$  of 26.4% at 401 nm). These results indicate that the fabrication of ST-OSCs with microcavity electrodes or narrow-bandwidth reflective filters has clear advantages in terms of obtaining the various colorful devices with the same active layer and improving the stability of devices.

## 5.2. ST-OSCs for Agrivoltaics

Recently, greenhouse-based agriculture has emerged as a viable method of sustainable agriculture. They offer high crop production with the minimum amount of water and without depending on the state of the outside environment. However, based on the external temperature, greenhouses require a significant amount of energy (by heating or cooling the space) to maintain an environment that is favorable for plant growth.<sup>[24–25]</sup> Hence, the “self-powered greenhouse” or “agrivoltaics” concept was developed to combine commercial agriculture and power generation as shown in schematic Figure 8a.<sup>[24–27]</sup>

Cao and co-workers presented a preliminary study on the use of ST-OSCs for self-powered greenhouses.<sup>[26]</sup> The authors proved that the transmission spectra of ternary ST-OSC devices based on a J52:IEICO-4F:PC<sub>71</sub>BM (1:0.9:0.6) blend is well-matched with the absorption wavelength of plant chlorophyll pigments, signifying that these blends are suitable candidates for agrivoltaics (Figure 8b). Thus, these results provided valuable initial guidance for the design of multifunctional ST-OSCs targeted toward self-powered greenhouse applications.

Due to the high PCE >10 and good transparency (AVT > 30% in the 400–700 nm region) of the PTB7-Th:IEICO-4F blend system, which is typically in the range required for plant growth (10–50%), Yang and co-workers further evaluated the

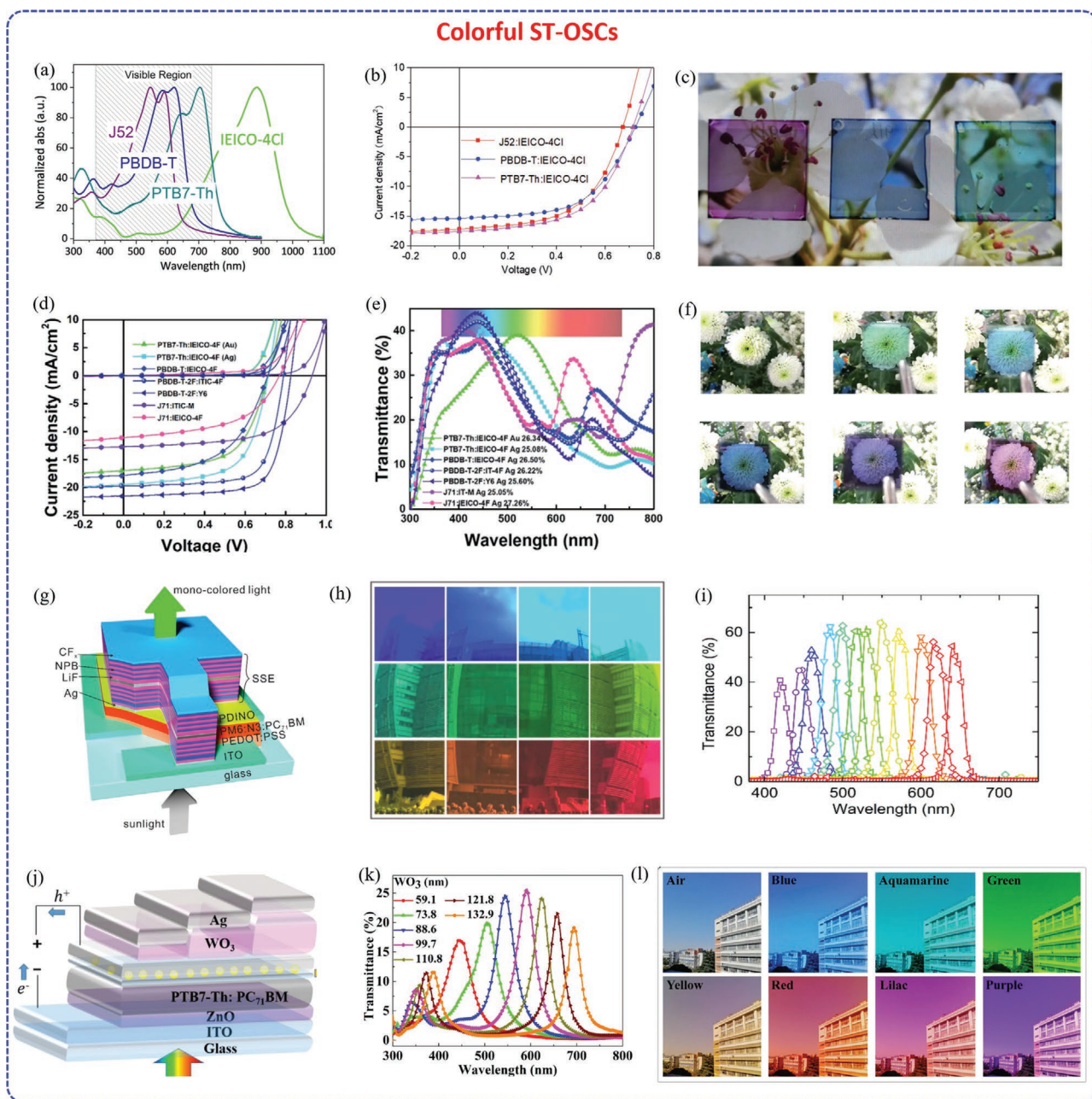


**Figure 7.** Colorful ST-OSCs: a) Normalized absorption spectra of IEICO-4Cl, J52, PBDB-T, and PTB7-Th:IEICO-4Cl in film state. Reproduced with permission.<sup>[164]</sup> Copyright 2020, American Chemical Society; b) J–V curve and c) photograph of three ST-OSCs (from left to right: J52:IEICO-4Cl, PBDB-T:IEICO-4Cl, and PTB7-Th:IEICO-4Cl, respectively). Reproduced with permission.<sup>[30]</sup> Copyright 2017, Wiley-VCH; Colorful ST-OSCs with different blend systems: d) J–V curves; e) Transmission spectra and f) Photograph of flowers seen through these ST-OSCs. Reproduced with permission.<sup>[31]</sup> Copyright 2019, the Royal Society of Chemistry; g) Schematic representation of the device architecture with an SSE; h) Montage photographs of a building taken through various SSEs. The photographs are arranged from left to right and top to bottom according to the ascending of transmission wavelengths and i) Corresponding transmission spectra of the ST-OSCs devices based on SSE. Reproduced with permission.<sup>[33]</sup> Copyright 2020, American Chemical Society and j) Schematic of hybrid-electrode-mirror microcavity-based ST-OSC devices with PTB7-Th:PC<sub>71</sub>BM as the active layer; k) Corresponding transmittance spectra of the colorful semitransparent devices and l) Digital photographs of buildings captured through the devices with various colors. Reproduced with permission.<sup>[32]</sup> Copyright 2019, American Chemical Society.

compatibility of these blends with agricultural applications by exploiting the unabsorbed visible light from ST-OSCs for plant growth (Figure 8c).<sup>[27]</sup> As shown in Figure 8d, the authors performed the side by side comparison of plant growth under normal sunlight and ST-OSCs. Inspiringly, the growth of mung

beans under normal sunlight and light transmitted by ST-OSCs based on the PTB7-Th:IEICO-4F blend produced almost the same results, indicating the great potential of such devices for the creation of self-powered greenhouses. Similarly, Ge and co-workers examined the potential of flexible ST-OSCs based

on the PBDB-T-2F:Y6 system with PCEs over 10% and 21% AVT for agrivoltaics by recreating greenhouse-like conditions (Figure 8e–g).<sup>[50]</sup> Like the previous study, the authors monitored the growth of the mung plants for 9 days under three different conditions, i.e., dark, natural sunlight, and sunlight passed through the flexible ST-OSCs and monitored distinct changes in terms of color, height, and branch sturdiness of the plant were observed based on the lighting condition (Figure 8h). Remarkably, plants were grown under the ST-OSCs and natural light was dark green and had similarly sturdy branches and hypertrophic leaves, suggesting that the ST-OSCs had no marked effect on photosynthesis under these conditions. On other hand, plants grown in the dark were light green and had slender stems and smaller leaves due to the chlorophyll deficiency caused by the inability to photosynthesize in the dark. In summary, these results provide valuable guidance for the design of ST-OSCs specifically for greenhouse photovoltaics, which have promising potentials in self-powered greenhouse agrivoltaics.

### 5.3. ST-OSCs for Heat-Control Functions

Methods of saving energy, such as passive radiative cooling, are essential to optimize the energy efficiency of buildings, which is often affected by continuous heating and cooling of buildings.<sup>[35–38]</sup> Modern design efforts have focused on the development of smart windows, which can simultaneously offer both power generation and heat insulation functions without affecting window transparency (Figure 9a). To achieve UV protection and heat rejection, ST-OSCs must not only have good visible transmission, but they must also absorb or reflect NIR and IR photons (especially in the 780–2500 nm wavelength region if they are not being utilized for photon harvesting).<sup>[35–38]</sup>

Sun et al. successfully developed dual-functional ST-OSC devices with good PCEs of over 7% and an AVT and IRR of 26.2% and 80.6%, respectively, by employing PBDTTF-ET:IEICO blend as photoabsorbent layer and advanced optical engineering using DBR materials (Figure 9b,c).<sup>[38]</sup> IEICO played a leading role in enhancing  $J_{sc}$  and minimizing the amount of heat that passed through the device by absorbing NIR photons up to 900 nm, whereas insertion of four-layered LiF/MoO<sub>3</sub> type DBR on the Ag electrode facilitated good transmittance in the visible region while maintaining high reflectance of NIR wavelengths. Moreover, the authors also verified the heat insulation property of these devices by capturing thermal images of metal objects that were heated through a glass substrate or an ST-OSCs, as shown in Figure 9d. Intriguingly, ST-OSC devices with an IRR of 75% resulted in lower temperatures than opaque glass (30.7 vs 34.4 °C), thereby emphasizing the reliability of this study.

Through optical simulation and the introduction of an effective photonic reflector layer, Li and co-workers developed multifunctional ST-OSC devices based on a ternary PBDB-TF:Y6:PBDB-TF blend.<sup>[35]</sup> Although these optimized devices showed slightly lower PCEs of 12% (AVT: 23%) than devices without reflectors, but they showed a remarkable IRR of 90% (vs 77%) in the 780–2500 nm and perfect coordination of the visible transmittance peak (555 nm) in the photo-response

region of the human eye with color coordinates (0.292, 0.369). Moreover, optical properties of devices were superior to commercially available heat-insulation films, such as 3M P-18ARL (AVT of 16% and IRR of 90%) without power generation ability and thus providing future perspectives for smart windows in BIPV.

Later, Li et al. also reported ST-OSCs for energy generation and heat-control functions by rational selection of active layer materials (PTB7-Th:IFIC-i-4 F), electron transport material (Bis-FIMG) and IR reflectors.<sup>[37]</sup> These devices displayed an AVT of 30%, PCE of 7.3% and IRR > 93% in the 780–2500 nm region. Thus, synergistic material and optical engineering approaches paved the way for these multifunctional ST-OSCs, which have a huge amount of potential for energy-saving BIPVs.

### 5.4. ST-OSCs for Floating Photovoltaic Applications

Relative to conventional large-scale PV solar projects, which are commonly mounted on urban areas or roof-tops, floating photovoltaic (FPV) will provide valuable alternatives for commercial solar power generation, particularly in densely populated countries having enormous competition for the use of lands.<sup>[165,167–169]</sup> A schematic diagram of this concept and its function is shown in Figure 9e. In addition to power generation, FPVs offer diverse advantages such as lower land usage, preventing water evaporation by cutting off the heat from the sun, enhancing the PCEs of FPVs in a warm atmosphere through passive cooling effect and lowering the algae blooms via shading effect, etc.<sup>[165,167–169]</sup> However, current FPV systems are mainly based on silicon-based PV arrays and they have negative effects on the ecological balance by completely blocking the essential solar light necessary to maintain aquatic flora and fauna. Therefore, various groups have recently been exploring the possibility of regulating aquatic environments and organisms by using the light transmitted through the ST-OSCs.

Along with the development of ST-OSCs for power-generation, Yu and co-workers carried out preliminary feasibility trials to assess the use of these cells in FPVs.<sup>[165]</sup> They fabricated three different ST-OSCs by employing PTB7-Th:PC<sub>71</sub>BM, PTB7-Th:ITIC and PTB7-Th:PNDI-T5 blends and systematically characterized the power generation, AVT and color perception of the corresponding devices.<sup>[165]</sup> Among these, devices based on the PTB7-Th:PC<sub>71</sub>BM blend produced a superior trade-off between PCE and AVT (6.7% and 30%, respectively) along with neutral color perception. To test their compatibility to use in FPVs, they placed large-area devices on these blends on top of a beaker containing water at 0° and 30° angles and then quantitatively analyzed the water evaporation and heat insulation capacity of these devices with the help of high-precision electronic balance and IR camera, respectively as shown in Figure 9f. Excitingly, all ST-OSCs devices placed on water beaker simultaneously reduced the rate of water evaporation (24–35%), surface temperature of the water (by 25–38%) and photothermal translation efficiency of steam formation (by 24–36%) compared to a control cell consisting of bare ITO glass placed on top of the beaker (Figure 9g,h). Thus, this was the first report which discovered the potential of ST-OSCs for FPV application.

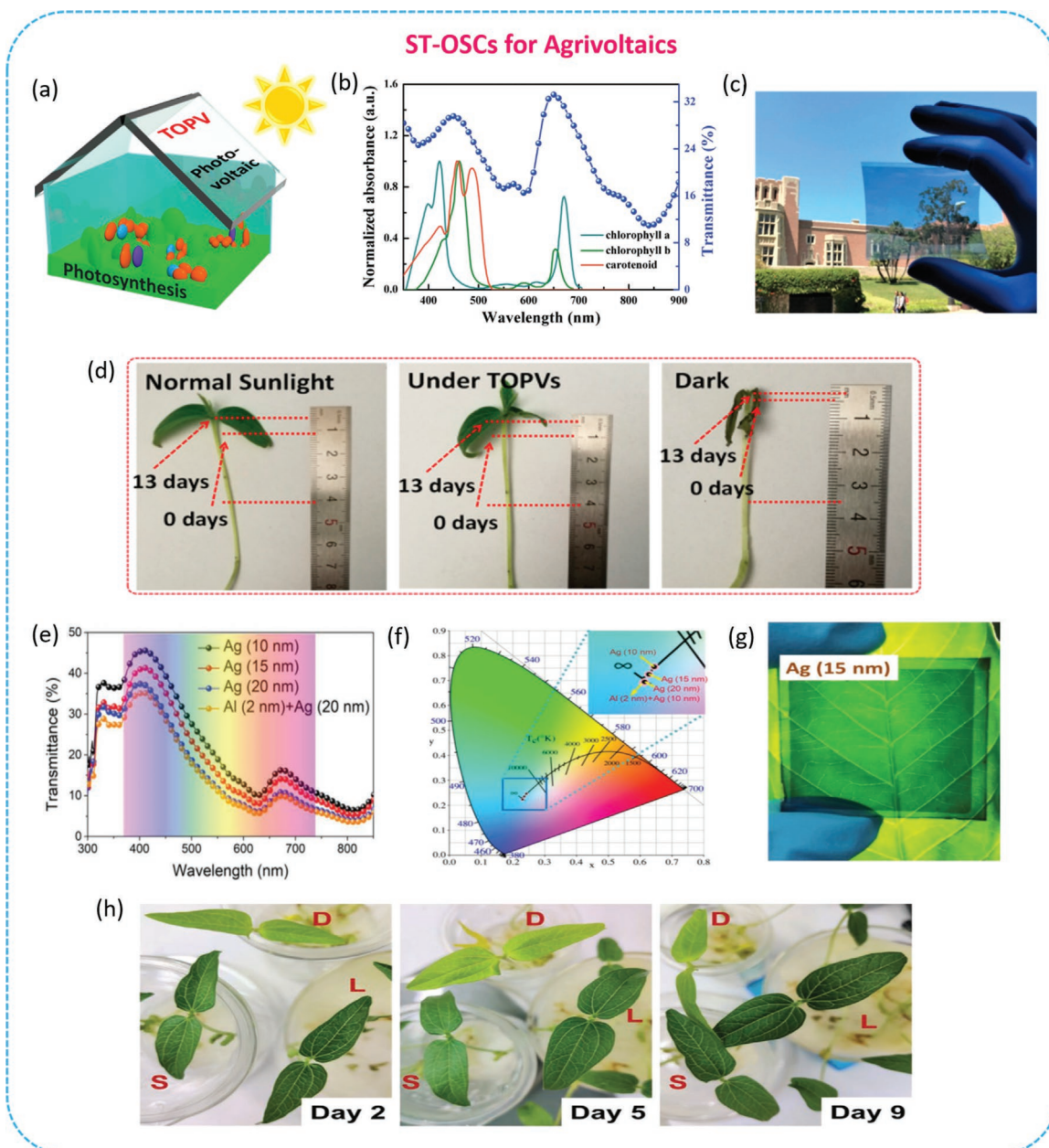


**Figure 8.** a) Illustration of flexible ST-OSCs for self-powered greenhouse applications; b) Comparison of transmission spectra of the J52:IEICO-4F:PC<sub>71</sub>BM-based (1:0.9:0.6) ST-OSC with optical absorption spectra of chlorophyll a, chlorophyll b, and carotenoid. b) Reproduced with permission.<sup>[26]</sup> Copyright 2019, Wiley-VCH; c) Illustration of flexible ST-OSCs for self-powered greenhouse applications; c) Photograph of a demo flexible ST-OSCs based on device structure of PET/Ag mesh/PH 1000/ZnO/active layer/MoO<sub>3</sub>/Au/Ag (size of 6 cm × 6 cm); d) Photographs of the length change of mung beans under different light conditions after 13 days (the original length was 3 cm). Reproduced with permission.<sup>[27]</sup> Copyright 2019, American Chemical Society; e) Transmission spectra of fabricated ST-OSCs based on PBDB-T-2F:Y6 blend; corresponding f) color coordinates on a CIE 1931xy chromaticity diagram and g) Photograph of ST-OSCs taken through green leaves, respectively and h) Photograph of mung bean leaves changing in 9 days under various light conditions (direct sunlight (L), direct sunlight with ST-OSCs roof (S), and dark (D)). Reproduced with permission.<sup>[50]</sup> Copyright 2020, Wiley-VCH.

Along the same lines, Xu and co-workers reported ternary ST-OSCs featuring PBDB-TF:Y6:PC<sub>71</sub>BM (PC<sub>71</sub>BM used as the third component) for FPV applications.<sup>[166]</sup> Interestingly, three different types (conventional, inverted and inverted with top MoO<sub>3</sub> layer (35 nm) as a photonic crystal) of ST-OSCs were fabricated by changing the device structure. Of these three types, the devices with conventional architecture achieved the highest

PCE of 13.0% (AVT: 21.4%) than the PCE of the inverted (PCE/AVT = 11.1/18%) and inverted + top MoO<sub>3</sub> layer (9.2/21.5%) devices. In-depth characterization revealed that broad EQE profiles, high and well-balanced charge carrier mobilities and negligible charge recombination, which emerged as a key factor, resulted in this superior PCE. To test these devices in FPV-like applications, the authors first investigated the influence of the

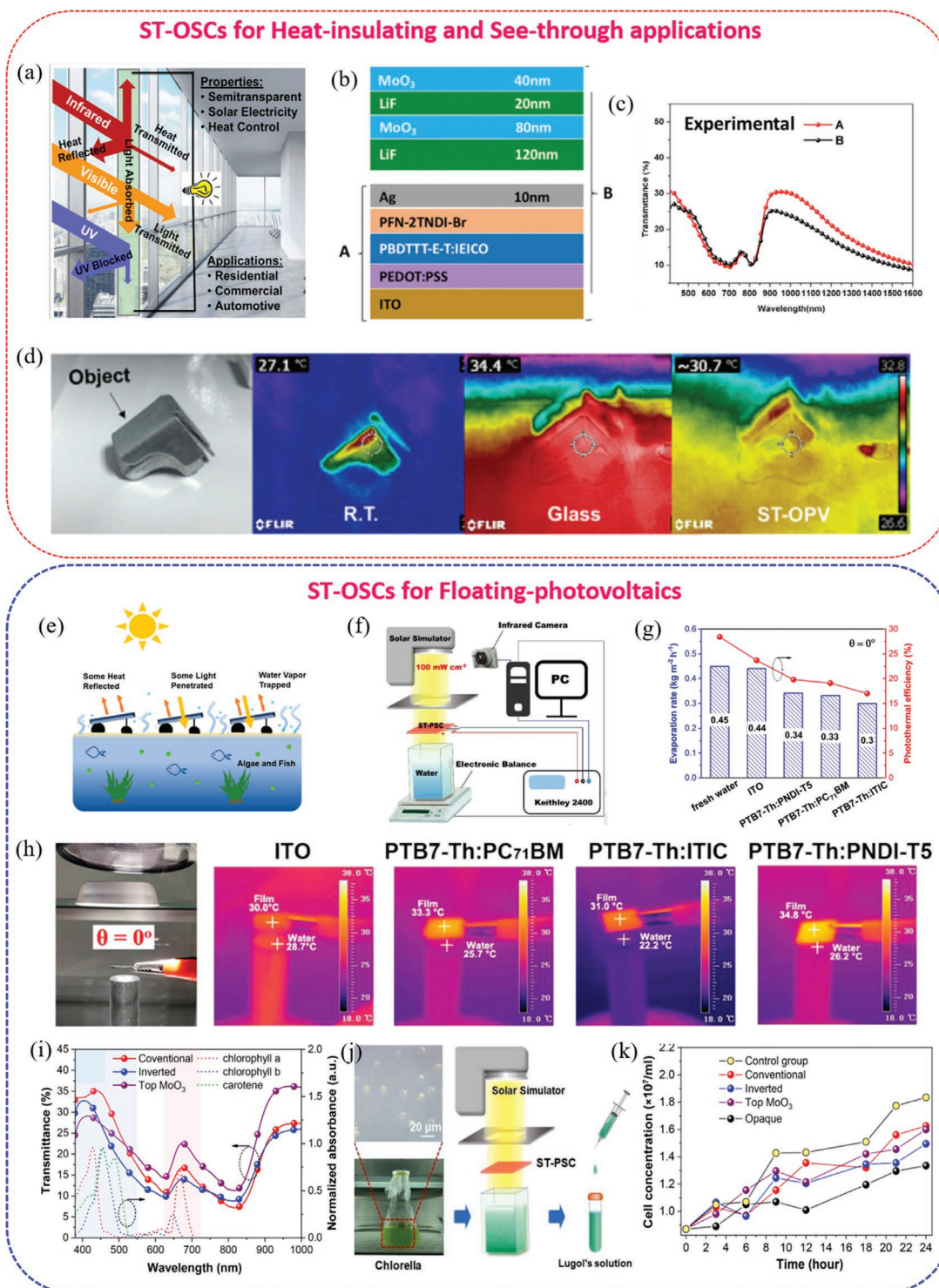


**Figure 9.** a) Illustration of multifunctional ST-OSCs for power generation, heat-insulation and see-through applications; b) Device structures of ST-OSCs based on PBDTTT-ET:IEICO active layer and without and with photonic reflector (device A and B, respectively); c) transmission spectra for the ST-OPVs with or without distributed Bragg reflectors and d) Thermal images taken with an IR camera for comparing heat-rejection properties of glass and ST-OSCs. Reproduced with permission.<sup>[38]</sup> Copyright 2018, Elsevier Inc.; e) Schematic illustration of floating photovoltaic concept; f) Setup of water evaporation and temperature measurement; g) Water evaporation rates and photothermal conversion efficiencies under AM1.5G when neat ITO glass and PTB7-Th:PC<sub>71</sub>BM, PTB7-Th:ITIC, and PTB7-Th:PNDI-T5-based ST-OSCs were angled at 0°; h) Photographs, IR images, and temperature profiles of the freshwater and corresponding ST-OSCs. e.g. and h) Reproduced with permission.<sup>[165]</sup> Copyright 2019, American Chemical Society and i) Comparison of Transmittance spectra of the ternary ST-OSCs based on PBDB-TF:Y6:PC<sub>71</sub>BM blend and absorbance spectra of common light-absorbing pigments in algal cells; j) Schematic of the setup for *Chlorella* proliferation characterization and k) variations on cell concentration of *Chlorella* over 24 h illumination. f,i–k) Reproduced with permission. Copyright 2020,<sup>[166]</sup> Elsevier Inc.



ST-OSCs on water evaporation by placing large-area ST-OSCs (active area of 0.97 cm<sup>2</sup> with 6.8% PCE and encapsulated by UV-cured resin/glass) on top of a square tube containing water and recorded changes in mass and temperature of the water with a high-precision electronic balance and IR camera, respectively. Indeed, the setup with the ST-OSC device showed slower water evaporation and lower temperature compared to the setup with bare water or that covered by ITO glass, indicating that the ST-device can effectively suppress water evaporation by selectively absorbing the photons in the longer wavelength. Next, the authors also studied the influence of ST-OSCs on growth and photosynthesis by exposing a tube containing green algae (*Chlorella*) to light transmitted through an ST-OSCs because of the overlap of the transmittance spectra of the ST-OSC and the absorbance spectra of common photosynthetic pigments in plants (Figure 9i–k). Gratifyingly, the algal growth rate in these conditions was superior to the growth rate in a similar setup with an opaque device, indicating that the ST-OSC did not negatively impact the photosynthetic process in the plants. In summary, these works suggest that the current problems associated with the silicone-based FPVs could be overcome by replacing them with the ST-OSCs and the scale-up of FPVs using ST-OSCs could be realistic in the near future.

### 5.5. ST-OSC-Based Solar Glasses

In 2017, Colsmann and co-workers reported the first representative wearable ST-OSCs, “solar-powered sunglasses”.<sup>[29]</sup> The ST-OSCs incorporated into the lenses generated enough power to run two display units and a microelectronic circuit that was used to provide information about the local temperature and the illumination intensity of solar light (Figure 10a). The photoabsorbent layer of these ST-OSCs was based on a ternary blend comprising PBTZT-stat-BDIT-8:PC<sub>61</sub>BM:PC<sub>71</sub>BM. The optimized devices based on the device structure of ITO/ZnO/active layer/PEDOT:PSS produced the best PCE of 4.8% for an active area of 0.24 cm<sup>2</sup>. To fit the lens frame, a larger substrate was prepared and, subsequently, the photoactive area was increased by 15.5 cm<sup>2</sup>. However, these devices showed a poor PCE of 0.06% due to a significant enhancement of the series resistances of the electrode. Later, by employing a modified PEDOT:PSS with lower resistance, the authors improved the PCEs of these devices to 2.4% (0.01 sun) or 6.7% (500 lux, LED luminaire) by minimizing power loss (detailed output power vs voltage graphs of these devices are shown in Figure 10b). They also studied color perception using the transmission profiles of the lens-fitted solar cells, and found that these devices yielded CIE 1931 color coordinates of (0.32, 0.37), CCT = 5933 K and CRI = 93, emphasizing the color-neutrality of these devices (Figure 10c). Thus, this study, which highlighted the self-powered and consumer-friendly wearables applications of ST-OSCs, which have enormous potential in the current digital world.

### 5.6. ST-OSCs for Automobile Sunroof Applications

Recently, Yao et al. developed ST-OSCs with switchable color and AVT functions, which are promising for use in photovoltaic vehicles (Figure 10d).<sup>[28]</sup> These ST-OSCs were fabricated using

PTB7-Th:FOIC as a photosensitive layer and the inverted device structure of ITO/PFN/active layer/MoO<sub>3</sub>/Ag/gasochromic WO<sub>3</sub>/platinum (Pt), where a WO<sub>3</sub>/Pt layer was used as a back reflector (Figure 10e). These devices realized impressive color switchability (between colored and bleached states, from now termed as “on” and “off” states, respectively) via introduction of evenly dispersed Pt nanoparticles (acts as a catalyst) on WO<sub>3</sub> thin film, which can easily be reduced/oxidized by hydrogen or oxygen exposure at ultrafast sub-second speeds (Figure 10f). By synergistically optimizing the device conditions, these devices produced a remarkable PCE of 10.2% (AVT: 25.4%) and 9.13% (AVT: 33.8%) in the “on” and “off” states, respectively (Figure 10g,h). The higher PCEs of ST-OSCs in the “on” state was due to the improved J<sub>sc</sub> of the devices, which is caused by the reflection of partial light back to the devices by the gasochromic WO<sub>3</sub> layer, as revealed by an optical adjustment study. Moreover, these devices showed excellent stability, including the reversibility of the gasochromic process and signifying their potential as semitransparent power-generating windows.

### 5.7. ST-OSCs for Indoor Photovoltaics

Due to the remarkable progress in the internet of things (IoT) (which includes low-power household products, sensors, wireless electronic devices, etc.), the notion of power generation using low-light indoor sources has recently gained considerable attention.<sup>[170–175]</sup> To maximize the PCEs of indoor ST-OSCs, a photoabsorbent material must have an absorbance, complementary to emission spectra of the indoor light source. The commonly used indoor light sources (such as fluorescent bulbs or light-emitting diodes (LEDs) emit light in the 400–800 nm range; hence, most of the photoabsorbent materials discussed in this report are not suitable for indoor ST-OSCs. Moreover, compared to the 1 Sun condition, the intensity of indoor light sources is much weaker. Hence, indoor cells with large areas are preferable to extract appreciable energies.

Recently, So and co-workers reported a series of indoor ST-OSCs that employ various novel porphyrin-based small molecule donors and a PC<sub>71</sub>BM acceptor.<sup>[39]</sup> The porphyrin donors exhibit unique absorption profiles; they display intense absorption at the blue or red ends of the spectrum, with the main peak in the visible or near-UV region and another peak in the IR region, along with poor absorption in the visible region (~550–700 nm, Figure 10i–k). The authors constructed ST-OSCs with a device structure of ITO/PEDOT:PSS/active layer/LiF/Al (25 nm). Devices based on four different photoabsorbent blends exhibited notable performance (PCEs of 8.2–11.0%) with corresponding extraordinary AVT values (63.0% to 68.3%) under 300 lx illumination from a 3000 K LED tube. The promising results of indoor ST-OSCs under low light intensity open the new concept of developing the ST-OSCs that can be used for indoor photovoltaic applications.

## 6. Conclusions and Future Perspectives

Because of the unique, adaptable features of ST-OSCs, such as enhanced transparency, color tunability, and multifunctional

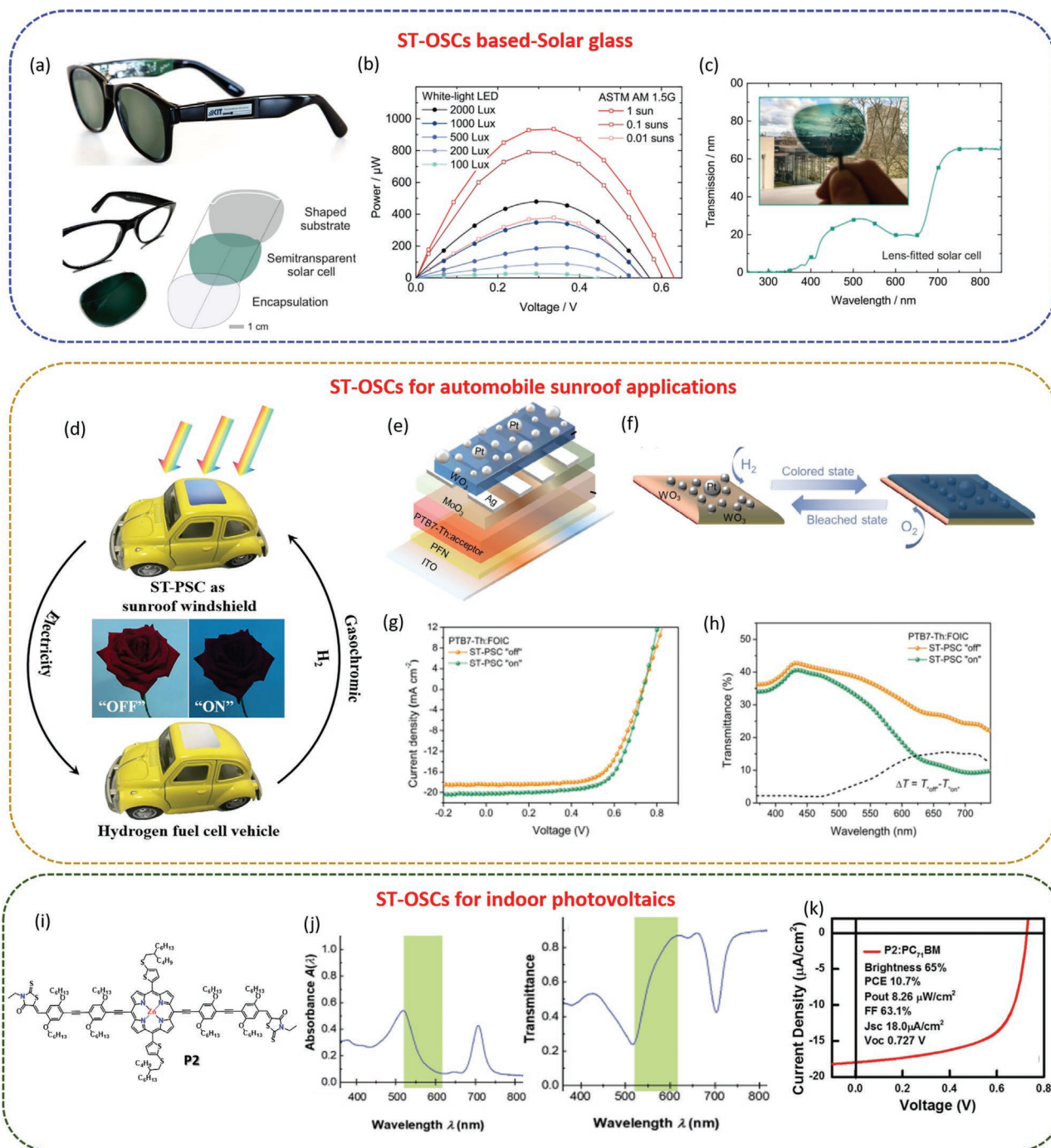


**Figure 10.** a) Photograph of solar glasses based on PBTZT-stat-BD TT-8:PC<sub>61</sub>BM:PC<sub>71</sub>BM blend in operation and its schematic representation of the solar glasses assembly; b) Output power of a typical lens-fitted solar cell measured under different illumination spectra and intensities; c) Representative transmission spectrum and photo of a lens-fitted solar cell. Reproduced with permission.<sup>[29]</sup> Copyright 2017, Wiley-VCH; d) Schematic showing that the working principle of a hydrogen fuel cell vehicle using a color-switchable ST-OSC as a sunroof windshield.; e) Device structure of the color and transparency-switchable ST-OSC; f) Working principle of gasochromic WO<sub>3</sub>/Pt layer; g)  $J-V$  characteristics of ST-OSCs based on PTB7-Th:FOIC in "off" and "on" states and h) corresponding transmission spectra. Reproduced with permission.<sup>[28]</sup> Copyright 2020, Elsevier Inc.; i) Chemical structure of porphyrin donor P2; j) Absorbance and transmittance spectra of P2:PC<sub>71</sub>BM-based blend (the highlighted green region of 520–617 nm indicates the region within the full width at half maximum (FWHM) of the incident illuminance in which human vision perceives most light) and k)  $J-V$  curve of the P2:PC<sub>71</sub>BM based optimized indoor ST-OSCs under a 300 lx illumination from a 3000 K LED tube. Reproduced with permission.<sup>[39]</sup> Copyright 2020, Wiley-VCH.

applications beyond power generation, they are considered an emerging horizon in photovoltaic technology, although the trade-off between PCE, optical transparency and appearance has yet to be resolved. In this progress report, we summarized the recent progress which has been made in this field, especially in the development of a range of highly efficient photoabsorbent materials for ST-OSCs, which have been instrumental in the enhancement of PCE from <3% in 2013 to ≈14% in 2020. The examples used in this study demonstrate the explicit link between molecular design and device performance, which greatly contributes to the commercial implementation of multifunctional ST-OSCs. Based on the examples presented herein, we will give our perspectives on the current challenges and provide guidelines that may help to push this field forward.

Undoubtedly, the use of LBG semiconductors will remain a preferred way to satisfy the strict absorption condition required by ST-OSCs through effectively harvesting photons in NIR wavelengths and without affecting transparency in the visible region. However, in most of these cases, the PCEs of ST-OSCs were still lower than those of opaque OSCs based on the same blends due to their limited light absorption. Hence, the future discovery of novel photo-harvesting materials with high molar absorptivity specifically compatible with ST-OSCs, along with device engineering, is essential to achieve PCEs beyond 15%.

- 1) Rational design of acceptor: i) Tailoring the optoelectronic properties of the “A–D–A”/ “A–DA’D–A-type” or “A–( $\pi$ -spacer)–D–( $\pi$ -spacer)–A” type FREAs through molecular engineering (by varying central “D” units/ $\pi$ -spacers, side chains and terminal “A” groups) is the most well-tested and desirable method of enhancing the absorption profiles of these FREAs. Thus, novel NFAs employing these methods must be developed to further decrease the bandgap of NFAs. ii) Most of the efficient NIR-NFAs reported so far have a strong intermolecular packing. Therefore, molecular structures involving planar and rigid molecular backbone must be considered to further lower the  $E_g$  of NFAs in the film state. iii) Despite the availability of many NIR-absorbing NFAs, only a few of these acceptors have been employed in ST-OSCs. Moreover, as discussed in this review, most of these NFAs use only DCI-based on electron-withdrawing “A” groups as terminal units. Currently, a wide variety of new “A” units become available, designing novel FREAs that employ these new “A” units will be an interesting research topic in the future. iv) Compared to symmetric NFAs, NFAs with asymmetric structures also exhibits additional advantages such as higher intermolecular binding energy and dipole moment and thus demonstrated their worth as excellent acceptors for OSCs.<sup>[90]</sup> Testing these NFAs for ST-OSCs could be an interesting research topic and v) Finally, the cost of FREAs is still not very economical to lower the overall cost of the final commercial products. In particular, the synthesis of highly rigid fused ring donor cores or fluorinated DCI units involves complex processes and produces low yields, leading to an increase in cost. Hence, the development of state-of-the-art FREAs with easily scalable molecular designs using cheaper precursors must be explored to further reduce their cost.
- 2) Rational design of donor: i) Relative to the development of NFAs, the progress of PDs specially tailored for ST-OSC applications is rather limited. To date, LBG PTB7-Th remains the preferred choice of “ED” in highly efficient ST-OSCs, suggesting that the rational design of ideal donors that match the appropriate NFAs is vital for further growth. As most NFAs have intense NIR absorption at 800–1050 nm, novel “ED” molecules must be designed with an eye toward good compatibility with available NFAs in terms of absorption profile, energy level matching, crystalline features, and charge mobility. ii) Also, small molecule donors, which constitute an important class of donor molecules for OSCs, are being completely ignored in ST-OSC applications despite their unique merits in comparison to their polymer counterparts, such as simple purification methods, well-defined structures with specific molecular weights and remarkable reproducibility; they are worth pursuing. iii) A recent report of efficient porphyrin-based indoor ST-OSCs<sup>[39]</sup> revealed that suggesting that porphyrin-based donors have the potential to deliver an excellent balance between PCE and AVT, and are worthy of further exploration.
- 3) The long-term stability, optimization of processing solvent and fabrication conditions are the main obstacles hindering the commercialization of ST-OSCs. For example, more studies using non-toxic halogen solvents<sup>[176]</sup> as well as those that employ large-scale fabrication methods like roll-to-roll or inkjet printing for device processing must be carried out. The performance and stability of ST-OSCs under realistic and harsh outdoor/testing conditions were also rarely reported upon, so particular attention must be paid to designing and developing active layer materials with a good photo and chemical stability and reliable encapsulation methods that increase the lifetime of such devices in the real-world applications.
- 4) Furthermore, new approaches from the device perspective, such as using the ternary or quaternary blend approach to effectively enhance the NIR-photo harvesting region or tailoring the absorption with the help of varying D-A ratio, active layer thickness and use of bilayer strategy must be tested for enhancing the AVT in ST-OSCs.
- 5) Along with active layer materials, transparent electrodes and interfacial layers also have significant effects on the PCE and transparency of ST-OSCs. Currently, ITO, an ultrathin film made up of Au or Ag nanowire,<sup>[177]</sup> graphene,<sup>[177]</sup> conducting polymers and carbon nanotubes,<sup>[178–181]</sup> is being used as an electrode material due to its high conductivity; however, there are some intrinsic drawbacks to the use of ITOs in large-scale ST-OSCs. For example, traditional ITOs are very brittle and easily broken, and thus cannot be used in flexible ST-OSCs. Metal electrodes, such as Au and Ag electrodes, are expensive and must often be deposited via vacuum deposition, making them less than ideal for mass production. Despite the advantages of electrodes based on graphene,<sup>[177]</sup> conducting polymers and carbon nanotubes,<sup>[178–182]</sup> such as solution processability and good stability, they show lower conductivity. Moreover, apart from the color tunability, flexibility is also a point of focus to meet the demands of smart ST-OSCs. As a result, the development of new transparent electrodes and, hole transport and electron transport layer with favorable optoelectronic, flexibility and processing properties should be explored further.

**Table 4.** Futuristic roadmap for the development of multifunctional ST-OSCs.

Type of ST-OSCs	Benefits	Current challenges	Possible solutions	Ref.
ST-OSCs for BIPVs	<ul style="list-style-type: none"> <li>– Power generation</li> <li>– Visual comfort</li> <li>– Lowering incident heat gain</li> </ul>	<ul style="list-style-type: none"> <li>– Low PCE</li> <li>– Poor trade-off between PCE and AVT</li> <li>– Small area devices</li> <li>– Stability issues</li> </ul>	<ul style="list-style-type: none"> <li>– Development of novel photovoltaic materials</li> <li>– Replacing top metal electrodes with emerging graphene and CNTs</li> <li>– Prototype or large-scale area devices must be tested</li> <li>– Developing new encapsulation techniques</li> </ul>	[43,48,56,61,79,127,133–134,140,147]
Colorful ST-OSCs	<ul style="list-style-type: none"> <li>– Various colors</li> <li>– aesthetic appeal</li> <li>– Generating power (electricity)</li> <li>– Diverse applications</li> </ul>	<ul style="list-style-type: none"> <li>– Low PCE with variable performances</li> <li>– Complex and high cost of the device with optical structures</li> </ul>	<ul style="list-style-type: none"> <li>– Designing new photovoltaic materials with different bandgaps</li> <li>– Exploring the new optical design strategies</li> </ul>	[27,30–34]
ST-OSCs with dual functionalities for thermochromic functions windows facades and solar sunroof.	<ul style="list-style-type: none"> <li>– Power generation</li> <li>– Privacy protection</li> <li>– Improving the power efficacy</li> <li>– Smart windows</li> <li>– Lowering incident heat gain</li> </ul>	<ul style="list-style-type: none"> <li>– These energy models still in the testing phase</li> <li>– Trade-off between PCE and functionalities is poor</li> <li>– Stimuli-response must be optimized depending upon the functionalities</li> </ul>	<ul style="list-style-type: none"> <li>– Development of new materials with NIR absorption and good stability</li> <li>– Using new optical design strategies and anti-reflecting layers</li> <li>– Using carbon top electrodes and device encapsulation</li> </ul>	[35–39]
ST-OSCs with dual functionalities for agrivoltaics/floating photovoltaics	<ul style="list-style-type: none"> <li>– Generating power/food production or preserving aquatic flora and fauna</li> <li>– Minimizing habitable land usage</li> <li>– Reduce cooling/heating costs</li> <li>– Reducing the water evaporation</li> <li>– Lowering the algae booms</li> </ul>	<ul style="list-style-type: none"> <li>– These energy models still in the testing phase</li> <li>– Trade-off between PCE and functionalities is poor</li> <li>– No complete feasibility studies were reported</li> </ul>	<ul style="list-style-type: none"> <li>– Development of efficient STOSCs based on new materials with NIR and UV light-harvesting</li> <li>– Feasibility of these energy models must be exclusively evaluated</li> <li>– Detailed study on optimization of the device structure, the effect of supplemental lighting, and plant growth optimization is necessary</li> </ul>	[24–27,50] and [165–169]
ST-OSCs for indoor photovoltaics	<ul style="list-style-type: none"> <li>– Power generation under lowlight indoor sources</li> <li>– Remote off-grid wireless charging</li> <li>– Self-powered household systems such as remote, smartwatch, wireless sensors, etc.</li> </ul>	<ul style="list-style-type: none"> <li>– Limited study</li> <li>– Lack of suitable photo-harvesting materials</li> <li>– Trade-off between PCE and functionalities is low for real applications</li> </ul>	<ul style="list-style-type: none"> <li>– Development of novel photovoltaic materials with photon absorption that are uneven with the emission spectra of indoor light sources</li> <li>– Detailed assessment criteria to realize high PCE, good transparency, and chromaticity must be evaluated</li> </ul>	[39,175]

- 6) In most of the previous reports, photovoltaic performances and AVT in ST-OSCs are discussed alone. As reported by Hou and co-workers<sup>[68]</sup> more unified measuring standards like light utilization efficiency (LUE) = performance × average photopic transmission (APT) must be implemented to accurately appraise the true potentials of ST-OSCs for practical applications.
- 7) Lastly, the cutting edge-multifunctional ST-OSCs field is yet in the initial stage and its device structure and requirement of the photoabsorbent layer will be dependent on the requirement of different scenarios. **Table 4** recapitulates the benefits, current challenges, and future directions for multifunctional ST-OSCs. Thus, appropriate active layer materials, optimization of such devices using different device fabrication methods, ternary or tandem structures and effective light management via microcavities, photonic crystals and reflection modulation is necessary to meet their demand.<sup>[54–55,163,183]</sup> Moreover, low-temperature processing techniques must be developed for the deposition of different layers in flexible ST-OSCs.

Finally, we strongly believe that most of these glitches will get resolved soon by technological advances and ST-OSCs will make life more colorful.

## Acknowledgements

This research was supported by the New & Renewable Energy Core Technology Program (No. 20193091010110) and Human Resources program in Energy Technology (No. 20194010201790) of the Korean Institute of Energy Technology Evaluation and Planning (KETEP) grant funded by the Ministry of Trade, Industry & Energy, Republic of Korea. This work was supported by the National Research Foundation of Korea (NRF) grant funded by the Korea government (MSIT) (NO. 2020R1A2C201091611). This research was supported by the 2020 KU Brain Pool of Konkuk University, Korea.

## Conflict of Interest

The authors declare no conflict of interest.

## Keywords

building-integrated photovoltaics, floating photovoltaics, heat-resistant ST-OSCs, low-bandgap materials, semitransparent OSCs, solar-powered greenhouses

Received: September 17, 2020

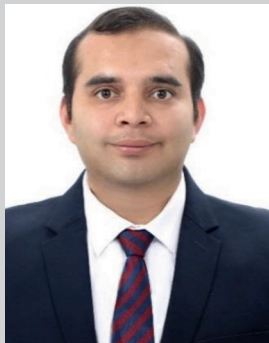
Revised: December 1, 2020

Published online:

- [1] Q. Xue, R. Xia, C. J. Brabec, H.-L. Yip, *Energy Environ. Sci.* **2018**, *11*, 1688.
- [2] F. C. Krebs, N. Espinosa, M. Hösel, R. R. Søndergaard, M. Jørgensen, *Adv. Mater.* **2014**, *26*, 29.
- [3] A. J. Heeger, *Adv. Mater.* **2014**, *26*, 10.
- [4] L. Lu, T. Zheng, Q. Wu, A. M. Schneider, D. Zhao, L. Yu, *Chem. Rev.* **2015**, *115*, 12666.
- [5] Y. Lin, Y. Jin, S. Dong, W. Zheng, J. Yang, A. Liu, F. Liu, Y. Jiang, T. P. Russell, F. Zhang, F. Huang, L. Hou, *Adv. Energy Mater.* **2018**, *8*, 1701942.
- [6] R. Xue, J. Zhang, Y. Li, Y. Li, *Small* **2018**, *14*, 1801793.
- [7] Y. Li, G. Xu, C. Cui, Y. Li, *Adv. Energy Mater.* **2018**, *8*, 1701791.
- [8] T. Yan, W. Song, J. Huang, R. Peng, L. Huang, Z. Ge, *Adv. Mater.* **2019**, *31*, 1902210.
- [9] J. Lee, Y.-H. Seo, S.-N. Kwon, D.-H. Kim, S. Jang, H. Jung, Y. Lee, H. Weerasinghe, T. Kim, J. Y. Kim, D. Vak, S.-I. Na, *Adv. Energy Mater.* **2019**, *9*, 1901805.
- [10] Y. Cui, H. Yao, J. Zhang, T. Zhang, Y. Wang, L. Hong, K. Xian, B. Xu, S. Zhang, J. Peng, Z. Wei, F. Gao, J. Hou, *Nat. Commun.* **2019**, *10*, 2515.
- [11] R. Yu, H. Yao, Y. Cui, L. Hong, C. He, J. Hou, *Adv. Mater.* **2019**, *31*, 1902302.
- [12] X. Xu, K. Feng, Z. Bi, W. Ma, G. Zhang, Q. Peng, *Adv. Mater.* **2019**, *31*, 1901872.
- [13] L. Hong, H. Yao, Z. Wu, Y. Cui, T. Zhang, Y. Xu, R. Yu, Q. Liao, B. Gao, K. Xian, H. Y. Woo, Z. Ge, J. Hou, *Adv. Mater.* **2019**, *31*, 1903441.
- [14] B. Fan, D. Zhang, M. Li, W. Zhong, Z. Zeng, L. Ying, F. Huang, Y. Cao, *Sci. China: Chem.* **2019**, *62*, 746.
- [15] L. Meng, Y. Zhang, X. Wan, C. Li, X. Zhang, Y. Wang, X. Ke, Z. Xiao, L. Ding, R. Xia, H.-L. Yip, Y. Cao, Y. Chen, *Science* **2018**, *361*, 1094.
- [16] L. Zhan, S. Li, T.-K. Lau, Y. Cui, X. Lu, M. Shi, C.-Z. Li, H. Li, J. Hou, H. Chen, *Energy Environ. Sci.* **2020**, *13*, 635.
- [17] W. Zhang, J. Huang, J. Xu, M. Han, D. Su, N. Wu, C. Zhang, A. Xu, C. Zhan, *Adv. Energy Mater.* **2020**, *10*, 2001436.
- [18] Y. Cui, H. Yao, J. Zhang, K. Xian, T. Zhang, L. Hong, Y. Wang, Y. Xu, K. Ma, C. An, C. He, Z. Wei, F. Gao, J. Hou, *Adv. Mater.* **2020**, *32*, 1908205.
- [19] R. J. Yang, P. X. W. Zou, *Int. J. Constr. Manage.* **2016**, *16*, 39.
- [20] E. Biyik, M. Araz, A. Hepbasli, M. Shahrestani, R. Yao, L. Shao, E. Essah, A. C. Oliveira, T. del Caño, E. Rico, J. L. Lechón, L. Andrade, A. Mendes, Y. B. Atli, *Eng. Sci. Technol. Int. J.* **2017**, *20*, 833.
- [21] D. E. Attoye, T. O. Adekunle, K. A. Tabet Aoul, A. Hassan, S. O. Attoye, *Sustainability* **2018**, *10*, 3781.
- [22] B. Zhong, Y. Hei, L. Jiao, H. Luo, J. Tang, *Int. J. Low-Carbon Technol.* **2019**, *15*, 241.
- [23] M. Batmunkh, Y. L. Zhong, H. Zhao, *Adv. Mater.* **2020**, *32*, 2000631.
- [24] C. J. M. Emmott, J. A. Röhr, M. Campoy-Quiles, T. Kirchartz, A. Urbina, N. J. Ekins-Daukes, J. Nelson, *Energy Environ. Sci.* **2015**, *8*, 1317.
- [25] E. Ravishanker, R. E. Booth, C. Saravitz, H. Sederoff, H. W. Ade, B. T. O'Connor, *Joule* **2020**, *4*, 490.
- [26] H. Shi, R. Xia, G. Zhang, H.-L. Yip, Y. Cao, *Adv. Energy Mater.* **2019**, *9*, 1803438.
- [27] Y. Liu, P. Cheng, T. Li, R. Wang, Y. Li, S.-Y. Chang, Y. Zhu, H.-W. Cheng, K.-H. Wei, X. Zhan, B. Sun, Y. Yang, *ACS Nano* **2019**, *13*, 1071.
- [28] M. Yao, T. Li, Y. Long, P. Shen, G. Wang, C. Li, J. Liu, W. Guo, Y. Wang, L. Shen, X. Zhan, *Sci. Bull.* **2020**, *65*, 217.
- [29] D. Landerer, D. Bahro, H. Röhm, M. Koppitz, A. Mertens, F. Manger, F. Denk, M. Heindinger, T. Windmann, A. Colsmann, *Energy Technol.* **2017**, *5*, 1936.
- [30] Y. Cui, C. Yang, H. Yao, J. Zhu, Y. Wang, G. Jia, F. Gao, J. Hou, *Adv. Mater.* **2017**, *29*, 1703080.
- [31] Y. Bai, C. Zhao, X. Chen, S. Zhang, S. Zhang, T. Hayat, A. Alsaedi, Z. a. Tan, J. Hou, Y. Li, *J. Mater. Chem. A* **2019**, *7*, 15887.
- [32] J. Zhong, Z. Xiao, W. Liang, Y. Wu, Q. Ye, H. Xu, H. Deng, L. Shen, X. Feng, Y. Long, *ACS Appl. Mater. Interfaces* **2019**, *11*, 47992.
- [33] S. Wang, J. Chen, L. Li, L. Zuo, T.-Y. Qu, H. Ren, Y. Li, A. K. Y. Jen, J.-X. Tang, *ACS Nano* **2020**, *14*, 5998.
- [34] X. Li, R. Xia, K. Yan, J. Ren, H.-L. Yip, C.-Z. Li, H. Chen, *ACS Energy Lett.* **2020**, *5*, 3115.
- [35] D. Wang, R. Qin, G. Zhou, X. Li, R. Xia, Y. Li, L. Zhan, H. Zhu, X. Lu, H.-L. Yip, H. Chen, C.-Z. Li, *Adv. Mater.* **2020**, *32*, 2001621.
- [36] N. C. Davy, M. Sezen-Edmonds, J. Gao, X. Lin, A. Liu, N. Yao, A. Kahn, Y.-L. Loo, *Nat. Energy* **2017**, *2*, 17104.
- [37] X. Li, R. Xia, K. Yan, H.-L. Yip, H. Chen, C.-Z. Li, *Chin. Chem. Lett.* **2020**, *31*, 1608.
- [38] C. Sun, R. Xia, H. Shi, H. Yao, X. Liu, J. Hou, F. Huang, H.-L. Yip, Y. Cao, *Joule* **2018**, *2*, 1816.
- [39] H. Yin, J. K. W. Ho, V. Piradi, S. Chen, X. Zhu, S. K. So, *Small Methods* **2020**, *4*, 2000136.
- [40] T. Ameri, G. Dennler, C. Waldauf, H. Azimi, A. Seemann, K. Forberich, J. Hauch, M. Scharber, K. Hingerl, C. J. Brabec, *Adv. Funct. Mater.* **2010**, *20*, 1592.
- [41] S.-Y. Chang, P. Cheng, G. Li, Y. Yang, *Joule* **2018**, *2*, 1039.
- [42] V. V. Brus, J. Lee, B. R. Luginbuhl, S.-J. Ko, G. C. Bazan, T.-Q. Nguyen, *Adv. Mater.* **2019**, *31*, 1900904.
- [43] K.-S. Chen, J.-F. Salinas, H.-L. Yip, L. Huo, J. Hou, A. K. Y. Jen, *Energy Environ. Sci.* **2012**, *5*, 9551.
- [44] M. Zhang, X. Guo, W. Ma, H. Ade, J. Hou, *Adv. Mater.* **2015**, *27*, 4655.
- [45] H. Shi, R. Xia, C. Sun, J. Xiao, Z. Wu, F. Huang, H.-L. Yip, Y. Cao, *Adv. Energy Mater.* **2017**, *7*, 1701121.
- [46] P. Meredith, W. Li, A. Armin, *Adv. Energy Mater.* **2020**, *10*, 2001788.
- [47] Z. Hu, Z. Wang, Q. An, F. Zhang, *Sci. Bull.* **2020**, *65*, 131.
- [48] T. Wang, R. Sun, S. Xu, J. Guo, W. Wang, J. Guo, X. Jiao, J. Wang, S. Jia, X. Zhu, Y. Li, J. Min, *J. Mater. Chem. A* **2019**, *7*, 14070.
- [49] Y. Xie, Y. Cai, L. Zhu, R. Xia, L. Ye, X. Feng, H.-L. Yip, F. Liu, G. Lu, S. Tan, Y. Sun, *Adv. Funct. Mater.* **2020**, *30*, 2002181.
- [50] W. Song, B. Fanady, R. Peng, L. Hong, L. Wu, W. Zhang, T. Yan, T. Wu, S. Chen, Z. Ge, *Adv. Energy Mater.* **2020**, *10*, 2000136.
- [51] Y. Wang, Y. Chang, J. Zhang, G. Lu, Z. Wei, *Chem. Res. Chin. Univ.* **2020**, *36*, 343.
- [52] Z. Hu, J. Wang, X. Ma, J. Gao, C. Xu, K. Yang, Z. Wang, J. Zhang, F. Zhang, *Nano Energy* **2020**, *78*, 105376.
- [53] C.-Y. Chen, G.-H. Tan, H.-L. Hsu, C.-P. Chen, H.-W. Lin, *Adv. Energy Sustainability Res.* **2020**, *1*, 2000035, <https://doi.org/10.1002/aesr.2020000352000035>
- [54] P. Shen, G. Wang, B. Kang, W. Guo, L. Shen, *ACS Appl. Mater. Interfaces* **2018**, *10*, 6513.
- [55] G. Xu, L. Shen, C. Cui, S. Wen, R. Xue, W. Chen, H. Chen, J. Zhang, H. Li, Y. Li, Y. Li, *Adv. Funct. Mater.* **2017**, *27*, 1605908.
- [56] M. B. Upama, M. Wright, N. K. Elumalai, M. A. Mahmud, D. Wang, C. Xu, A. Uddin, *ACS Photonics* **2017**, *4*, 2327.
- [57] C. J. Traverse, R. Pandey, M. C. Barr, R. R. Lunt, *Nat. Energy* **2017**, *2*, 849.
- [58] C.-C. Chueh, S.-C. Chien, H.-L. Yip, J. F. Salinas, C.-Z. Li, K.-S. Chen, F.-C. Chen, W.-C. Chen, A. K.-Y. Jen, *Adv. Energy Mater.* **2013**, *3*, 417.
- [59] W. Yu, X. Jia, M. Yao, L. Zhu, Y. Long, L. Shen, *Phys. Chem. Chem. Phys.* **2015**, *17*, 23732.
- [60] A. Colsmann, A. Puetz, A. Bauer, J. Hanisch, E. Ahlswede, U. Lemmer, *Adv. Energy Mater.* **2011**, *1*, 599.

- [61] J. Mescher, S. W. Kettlitz, N. Christ, M. F. G. Klein, A. Puetz, A. Mertens, A. Colsmann, U. Lemmer, *Org. Electron.* **2014**, *15*, 1476.
- [62] D. H. Shin, S.-H. Choi, *Coatings* **2018**, *8*, 329.
- [63] N. Lynn, L. Mohanty, S. Wittkopf, *Build. Environ.* **2012**, *54*, 148.
- [64] W. Yu, X. Jia, Y. Long, L. Shen, Y. Liu, W. Guo, S. Ruan, *ACS Appl. Mater. Interfaces* **2015**, *7*, 9920.
- [65] C.-C. Chen, L. Dou, J. Gao, W.-H. Chang, G. Li, Y. Yang, *Energy Environ. Sci.* **2013**, *6*, 2714.
- [66] R. Xia, H. Gu, S. Liu, K. Zhang, H.-L. Yip, Y. Cao, *Sol. RRL* **2019**, *3*, 1800270.
- [67] Y. Li, C. Ji, Y. Qu, X. Huang, S. Hou, C.-Z. Li, L.-S. Liao, L. J. Guo, S. R. Forrest, *Adv. Mater.* **2019**, *31*, 1903173.
- [68] Y. Li, X. Guo, Z. Peng, B. Qu, H. Yan, H. Ade, M. Zhang, S. R. Forrest, *Proc. Natl. Acad. Sci. USA* **2020**, *117*, 202007799.
- [69] R. Ganesamoorthy, G. Sathiyam, P. Sakthivel, *Sol. Energy Mater. Sol. Cells* **2017**, *161*, 102.
- [70] L. Dou, Y. Liu, Z. Hong, G. Li, Y. Yang, *Chem. Rev.* **2015**, *115*, 12633.
- [71] J. Hou, H.-Y. Chen, S. Zhang, G. Li, Y. Yang, *J. Am. Chem. Soc.* **2008**, *130*, 16144.
- [72] L. Huo, S. Zhang, X. Guo, F. Xu, Y. Li, J. Hou, *Angew. Chem., Int. Ed.* **2011**, *50*, 9697.
- [73] Y. Q. Wong, H.-F. Meng, H. Y. Wong, C. S. Tan, C.-Y. Wu, P.-T. Tsai, C.-Y. Chang, S.-F. Horng, H.-W. Zan, *Org. Electron.* **2017**, *43*, 196.
- [74] C.-C. Chen, L. Dou, R. Zhu, C.-H. Chung, T.-B. Song, Y. B. Zheng, S. Hawks, G. Li, P. S. Weiss, Y. Yang, *ACS Nano* **2012**, *6*, 7185.
- [75] L. Dou, W.-H. Chang, J. Gao, C.-C. Chen, J. You, Y. Yang, *Adv. Mater.* **2013**, *25*, 825.
- [76] Y. Zhang, J. Zou, C.-C. Cheuh, H.-L. Yip, A. K. Y. Jen, *Macromolecules* **2012**, *45*, 5427.
- [77] C.-Y. Chang, L. Zuo, H.-L. Yip, Y. Li, C.-Z. Li, C.-S. Hsu, Y.-J. Cheng, H. Chen, A. K.-Y. Jen, *Adv. Funct. Mater.* **2013**, *23*, 5084.
- [78] A. R. b. M. Yusoff, S. J. Lee, F. K. Shneider, W. J. da Silva, J. Jang, *Adv. Energy Mater.* **2014**, *4*, 1301989.
- [79] C.-Y. Chang, L. Zuo, H.-L. Yip, C.-Z. Li, Y. Li, C.-S. Hsu, Y.-J. Cheng, H. Chen, A. K.-Y. Jen, *Adv. Energy Mater.* **2014**, *4*, 1301645.
- [80] Z. He, B. Xiao, F. Liu, H. Wu, Y. Yang, S. Xiao, C. Wang, T. P. Russell, Y. Cao, *Nat. Photonics* **2015**, *9*, 174.
- [81] C. Liu, C. Yi, K. Wang, Y. Yang, R. S. Bhatta, M. Tsige, S. Xiao, X. Gong, *ACS Appl. Mater. Interfaces* **2015**, *7*, 4928.
- [82] T. Ameri, N. Li, C. J. Brabec, *Energy Environ. Sci.* **2013**, *6*, 2390.
- [83] J. You, L. Dou, Z. Hong, G. Li, Y. Yang, *Prog. Polym. Sci.* **2013**, *38*, 1909.
- [84] D. Di Carlo Rasi, R. A. J. Janssen, *Adv. Mater.* **2019**, *31*, 1806499.
- [85] Z. Zhang, J. Yuan, Q. Wei, Y. Zou, *Front. Chem.* **2018**, *6*, 414.
- [86] S. Dey, *Small* **2019**, *15*, 1900134.
- [87] G. Zhang, J. Zhao, P. C. Y. Chow, K. Jiang, J. Zhang, Z. Zhu, J. Zhang, F. Huang, H. Yan, *Chem. Rev.* **2018**, *118*, 3447.
- [88] S. A. Lopez, B. Sanchez-Lengeling, J. de Goes Soares, A. Aspuru-Guzik, *Joule* **2017**, *1*, 857.
- [89] Z.-Q. Jiang, T.-T. Wang, F.-P. Wu, J.-D. Lin, L.-S. Liao, *J. Mater. Chem. A* **2018**, *6*, 17256.
- [90] C. Li, H. Fu, T. Xia, Y. Sun, *Adv. Energy Mater.* **2019**, *9*, 1900999.
- [91] H. Wang, J. Cao, J. Yu, Z. Zhang, R. Geng, L. Yang, W. Tang, *J. Mater. Chem. A* **2019**, *7*, 4313.
- [92] J.-L. Wang, K.-K. Liu, L. Hong, G.-Y. Ge, C. Zhang, J. Hou, *ACS Energy Lett.* **2018**, *3*, 2967.
- [93] H. Feng, Y. Q. Q. Yi, X. Ke, J. Yan, Y. Zhang, X. Wan, C. Li, N. Zheng, Z. Xie, Y. Chen, *Adv. Energy Mater.* **2019**, *9*, 1803541.
- [94] X. Shi, J. Chen, K. Gao, L. Zuo, Z. Yao, F. Liu, J. Tang, A. K.-Y. Jen, *Adv. Energy Mater.* **2018**, *8*, 1702831.
- [95] J. Qu, Q. Zhao, J. Zhou, H. Lai, T. Liu, D. Li, W. Chen, Z. Xie, F. He, *Chem. Mater.* **2019**, *31*, 1664.
- [96] G. P. Kini, S. J. Jeon, D. K. Moon, *Adv. Mater.* **2020**, *32*, 1906175.
- [97] Y. Lin, J. Wang, Z.-G. Zhang, H. Bai, Y. Li, D. Zhu, X. Zhan, *Adv. Mater.* **2015**, *27*, 1170.
- [98] W. Wang, C. Yan, T.-K. Lau, J. Wang, K. Liu, Y. Fan, X. Lu, X. Zhan, *Adv. Mater.* **2017**, *29*, 1701308.
- [99] G. Sun, M. Shahid, Z. Fei, S. Xu, F. D. Eisner, T. D. Anthopoulos, M. A. McLachlan, M. Heeney, *Mater. Chem. Front.* **2019**, *3*, 450.
- [100] Q. Zhang, M. A. Kelly, N. Bauer, W. You, *Acc. Chem. Res.* **2017**, *50*, 2401.
- [101] Q. Fan, U. A. Méndez-Romero, X. Guo, E. Wang, M. Zhang, Y. Li, *Chem. - Asian J.* **2019**, *14*, 3085.
- [102] H. Yao, Y. Cui, R. Yu, B. Gao, H. Zhang, J. Hou, *Angew. Chem., Int. Ed.* **2017**, *56*, 3045.
- [103] F. Zhao, S. Dai, Y. Wu, Q. Zhang, J. Wang, L. Jiang, Q. Ling, Z. Wei, W. Ma, W. You, C. Wang, X. Zhan, *Adv. Mater.* **2017**, *29*, 1700144.
- [104] J. Yuan, Y. Zhang, L. Zhou, G. Zhang, H.-L. Yip, T.-K. Lau, X. Lu, C. Zhu, H. Peng, P. A. Johnson, M. Leclerc, Y. Cao, J. Ulanski, Y. Li, Y. Zou, *Joule* **2019**, *3*, 1140.
- [105] G. P. Kini, H. S. Park, S. J. Jeon, Y. W. Han, D. K. Moon, *Sol. Energy* **2020**, *207*, 720.
- [106] G. P. Kini, J. Y. Choi, S. J. Jeon, I. S. Suh, D. K. Moon, *Polymer* **2018**, *148*, 330.
- [107] J. Yang, M. A. Uddin, Y. Tang, Y. Wang, Y. Wang, H. Su, R. Gao, Z.-K. Chen, J. Dai, H. Y. Woo, X. Guo, *ACS Appl. Mater. Interfaces* **2018**, *10*, 23235.
- [108] S. Chen, H. Yao, Z. Li, O. M. Awartani, Y. Liu, Z. Wang, G. Yang, J. Zhang, H. Ade, H. Yan, *Adv. Energy Mater.* **2017**, *7*, 1602304.
- [109] G. P. Kini, Q. V. Hoang, C. E. Song, S. K. Lee, W. S. Shin, W.-W. So, M. A. Uddin, H. Y. Woo, J.-C. Lee, *Polym. Chem.* **2017**, *8*, 3622.
- [110] W. Zhao, S. Li, H. Yao, S. Zhang, Y. Zhang, B. Yang, J. Hou, *J. Am. Chem. Soc.* **2017**, *139*, 7148.
- [111] S. Dai, F. Zhao, Q. Zhang, T.-K. Lau, T. Li, K. Liu, Q. Ling, C. Wang, X. Lu, W. You, X. Zhan, *J. Am. Chem. Soc.* **2017**, *139*, 1336.
- [112] S. M. Swick, J. M. Alzola, V. K. Sangwan, S. H. Amsterdam, W. Zhu, L. O. Jones, N. Powers-Riggs, A. Facchetti, K. L. Kohlstedt, G. C. Schatz, M. C. Hersam, M. R. Wasielewski, T. J. Marks, *Adv. Energy Mater.* **2020**, *10*, 2000635.
- [113] T. Li, S. Dai, Z. Ke, L. Yang, J. Wang, C. Yan, W. Ma, X. Zhan, *Adv. Mater.* **2018**, *30*, 1705969.
- [114] Y. Xie, R. Xia, T. Li, L. Ye, X. Zhan, H.-L. Yip, Y. Sun, *Small Methods* **2019**, *3*, 1900424.
- [115] B. Jia, S. Dai, Z. Ke, C. Yan, W. Ma, X. Zhan, *Chem. Mater.* **2018**, *30*, 239.
- [116] X. Zhang, D. Zhang, Q. Zhou, R. Wang, J. Zhou, J. Wang, H. Zhou, Y. Zhang, *Nano Energy* **2019**, *56*, 494.
- [117] R. Ma, Y. Chen, T. Liu, Y. Xiao, Z. Luo, M. Zhang, S. Luo, X. Lu, G. Zhang, Y. Li, H. Yan, K. Chen, *J. Mater. Chem. C* **2020**, *8*, 909.
- [118] Y. Wu, H. Yang, Y. Zou, Y. Dong, J. Yuan, C. Cui, Y. Li, *Energy Environ. Sci.* **2019**, *12*, 675.
- [119] W. Su, Q. Fan, X. Guo, J. Wu, M. Zhang, Y. Li, *Phys. Chem. Chem. Phys.* **2019**, *21*, 10660.
- [120] Z. Hu, Z. Wang, F. Zhang, *J. Mater. Chem. A* **2019**, *7*, 7025.
- [121] Y. Dong, H. Yang, Y. Wu, Y. Zou, J. Yuan, C. Cui, Y. Li, *J. Mater. Chem. A* **2019**, *7*, 2261.
- [122] J. Zhu, Y. Xiao, J. Wang, K. Liu, H. Jiang, Y. Lin, X. Lu, X. Zhan, *Chem. Mater.* **2018**, *30*, 4150.
- [123] J. Wang, J. Zhang, Y. Xiao, T. Xiao, R. Zhu, C. Yan, Y. Fu, G. Lu, X. Lu, S. R. Marder, X. Zhan, *J. Am. Chem. Soc.* **2018**, *140*, 9140.
- [124] T. Xiao, J. Wang, S. Yang, Y. Zhu, D. Li, Z. Wang, S. Feng, L. Bu, X. Zhan, G. Lu, *J. Mater. Chem. A* **2020**, *8*, 401.
- [125] W. Liu, J. Zhang, Z. Zhou, D. Zhang, Y. Zhang, S. Xu, X. Zhu, *Adv. Mater.* **2018**, *30*, 1800403.
- [126] H. Zhang, H. Yao, J. Hou, J. Zhu, J. Zhang, W. Li, R. Yu, B. Gao, S. Zhang, J. Hou, *Adv. Mater.* **2018**, *30*, 1800613.

- [127] Y. Li, J. D. Lin, X. Che, Y. Qu, F. Liu, L. S. Liao, S. R. Forrest, *J. Am. Chem. Soc.* **2017**, *139*, 17114.
- [128] P. Chao, L. Liu, J. Zhou, J. Qu, D. Mo, H. Meng, Z. Xie, F. He, Y. Ma, *ACS Appl. Energy Mater.* **2018**, *1*, 6549.
- [129] S. Zhang, Y. Qin, J. Zhu, J. Hou, *Adv. Mater.* **2018**, *30*, 1800868.
- [130] X. Li, H. Meng, F. Shen, D. Su, S. Huo, J. Shan, J. Huang, C. Zhan, *Dyes Pigment.* **2019**, *166*, 196.
- [131] C.-K. Wang, B.-H. Jiang, J.-H. Lu, M.-T. Cheng, R.-J. Jeng, Y.-W. Lu, C.-P. Chen, K.-T. Wong, *ChemSusChem* **2020**, *13*, 903.
- [132] Y. Wang, B. Jia, F. Qin, Y. Wu, W. Meng, S. Dai, Y. Zhou, X. Zhan, *Polymer* **2016**, *107*, 108.
- [133] F. Liu, Z. Zhou, C. Zhang, J. Zhang, Q. Hu, T. Vergote, F. Liu, T. P. Russell, X. Zhu, *Adv. Mater.* **2017**, *29*, 1606574.
- [134] J. Lee, H. Cha, H. Yao, J. Hou, Y.-H. Suh, S. Jeong, K. Lee, J. R. Durrant, *ACS Appl. Mater. Interfaces* **2020**, *12*, 32764.
- [135] Y. Song, K. Zhang, S. Dong, R. Xia, F. Huang, Y. Cao, *ACS Appl. Mater. Interfaces* **2020**, *3*, 7689.
- [136] J. Chen, G. Li, Q. Zhu, X. Guo, Q. Fan, W. Ma, M. Zhang, *J. Mater. Chem. A* **2019**, *7*, 3745.
- [137] H. Huang, X. Li, L. Zhong, B. Qiu, Y. Yang, Z.-G. Zhang, Z. Zhang, Y. Li, *J. Mater. Chem. A* **2018**, *6*, 4670.
- [138] Y. Cho, T. H. Lee, S. Jeong, S. Y. Park, B. Lee, J. Y. Kim, C. Yang, *ACS Appl. Energy Mater.* **2020**, *3*, 7689.
- [139] M. Luo, C. Zhao, J. Yuan, J. Hai, F. Cai, Y. Hu, H. Peng, Y. Bai, Z. a. Tan, Y. Zou, *Mater. Chem. Front.* **2019**, *3*, 2483.
- [140] E. Pascual-San-José, G. Sadoughi, L. Lucera, M. Stella, E. Martínez-Ferrero, G. E. Morse, M. Campoy-Quiles, I. Burgués-Ceballos, *J. Mater. Chem. A* **2020**, *8*, 9882.
- [141] L. Zhan, S. Li, S. Zhang, X. Chen, T. K. Lau, X. Lu, M. Shi, C. Z. Li, H. Chen, *ACS Appl. Mater. Interfaces* **2018**, *10*, 42444.
- [142] L. Zhan, S. Li, H. Zhang, F. Gao, T.-K. Lau, X. Lu, D. Sun, P. Wang, M. Shi, C.-Z. Li, H. Chen, *Adv. Sci.* **2018**, *5*, 1800755.
- [143] S. Li, L. Zhan, F. Liu, J. Ren, M. Shi, C.-Z. Li, T. P. Russell, H. Chen, *Adv. Mater.* **2018**, *30*, 1705208.
- [144] S. Li, L. Zhan, W. Zhao, S. Zhang, B. Ali, Z. Fu, T.-K. Lau, X. Lu, M. Shi, C.-Z. Li, J. Hou, H. Chen, *J. Mater. Chem. A* **2018**, *6*, 12132.
- [145] Y. Wu, H. Bai, Z. Wang, P. Cheng, S. Zhu, Y. Wang, W. Ma, X. Zhan, *Energy Environ. Sci.* **2015**, *8*, 3215.
- [146] X. Ma, Z. Xiao, Q. An, M. Zhang, Z. Hu, J. Wang, L. Ding, F. Zhang, *J. Mater. Chem. A* **2018**, *6*, 21485.
- [147] J. Zhang, G. Xu, F. Tao, G. Zeng, M. Zhang, Y. Yang, Y. Li, Y. Li, *Adv. Mater.* **2019**, *31*, 1807159.
- [148] Y. Cui, H. Yao, L. Hong, T. Zhang, Y. Tang, B. Lin, K. Xian, B. Gao, C. An, P. Bi, W. Ma, J. Hou, *Natl. Sci. Rev.* **2020**, *7*, 1239.
- [149] R. Qin, D. Wang, G. Zhou, Z.-P. Yu, S. Li, Y. Li, Z.-X. Liu, H. Zhu, M. Shi, X. Lu, C.-Z. Li, H. Chen, *J. Mater. Chem. A* **2019**, *7*, 27632.
- [150] S. Li, C.-Z. Li, M. Shi, H. Chen, *ACS Energy Lett.* **2020**, *5*, 1554.
- [151] L. Yang, L. Yan, W. You, *J. Phys. Chem. Lett.* **2013**, *4*, 1802.
- [152] T. Ameri, P. Khoram, J. Min, C. J. Brabec, *Adv. Mater.* **2013**, *25*, 4245.
- [153] P. Bi, X. Hao, *Sol. RRL* **2019**, *3*, 1800263.
- [154] Q. An, J. Zhang, W. Gao, F. Qi, M. Zhang, X. Ma, C. Yang, L. Huo, F. Zhang, *Small* **2018**, *14*, 1802983.
- [155] N. Gasparini, A. Salleo, I. McCulloch, D. Baran, *Nat. Rev. Mater.* **2019**, *4*, 229.
- [156] H. Huang, L. Yang, B. Sharma, *J. Mater. Chem. A* **2017**, *5*, 11501.
- [157] K. Li, Y. Wu, Y. Tang, M.-A. Pan, W. Ma, H. Fu, C. Zhan, J. Yao, *Adv. Energy Mater.* **2019**, *9*, 1901728.
- [158] S. Langner, F. Häse, J. D. Perea, T. Stubhan, J. Hauch, L. M. Roch, T. Heumueller, A. Aspuru-Guzik, C. J. Brabec, *Adv. Mater.* **2020**, *32*, 1907801.
- [159] M. Nam, J.-h. Kang, J. Shin, J. Na, Y. Park, J. Cho, B. Kim, H. H. Lee, R. Chang, D.-H. Ko, *Adv. Energy Mater.* **2019**, *9*, 1901856.
- [160] Y. Xie, L. Huo, B. Fan, H. Fu, Y. Cai, L. Zhang, Z. Li, Y. Wang, W. Ma, Y. Chen, Y. Sun, *Adv. Funct. Mater.* **2018**, *28*, 1800627.
- [161] C. Zhu, H. Huang, Z. Jia, F. Cai, J. Li, J. Yuan, L. Meng, H. Peng, Z. Zhang, Y. Zou, Y. Li, *Sol. Energy* **2020**, *204*, 660.
- [162] Z. Hu, J. Wang, Z. Wang, W. Gao, Q. An, M. Zhang, X. Ma, J. Wang, J. Miao, C. Yang, F. Zhang, *Nano Energy* **2019**, *55*, 424.
- [163] R. Betancur, P. Romero-Gomez, A. Martínez-Otero, X. Elias, M. Maymó, J. Martorell, *Nat. Photonics* **2013**, *7*, 995.
- [164] H. Yao, J. Wang, Y. Xu, S. Zhang, J. Hou, *Acc. Chem. Res.* **2020**, *53*, 822.
- [165] N. Zhang, G. Chen, Y. Xu, X. Xu, L. Yu, *ACS Appl. Energy Mater.* **2019**, *2*, 6060.
- [166] N. Zhang, T. Jiang, C. Guo, L. Qiao, Q. Ji, L. Yin, L. Yu, P. Murto, X. Xu, *Nano Energy* **2020**, *77*, 105111.
- [167] K. Trapani, M. Redón Santafé, *Prog. Photovoltaics* **2015**, *23*, 524.
- [168] R. S. Spencer, J. Macknick, A. Aznar, A. Warren, M. O. Reese, *Environ. Sci. Technol.* **2019**, *53*, 1680.
- [169] R. Cazzaniga, M. Cicu, M. Rosa-Clot, P. Rosa-Clot, G. M. Tina, C. Ventura, *Renewable Sustainable Energy Rev.* **2018**, *81*, 1730.
- [170] H. K. H. Lee, J. Wu, J. Barbé, S. M. Jain, S. Wood, E. M. Speller, Z. Li, F. A. Castro, J. R. Durrant, W. C. Tsoi, *J. Mater. Chem. A* **2018**, *6*, 5618.
- [171] S. Kim, M. Jahandar, J. H. Jeong, D. C. Lim, *Curr. Altern. Energy* **2019**, *3*.
- [172] Y. Cui, Y. Wang, J. Bergqvist, H. Yao, Y. Xu, B. Gao, C. Yang, S. Zhang, O. Inganäs, F. Gao, J. Hou, *Nat. Energy* **2019**, *4*, 768.
- [173] M. Mainville, M. Leclerc, *ACS Energy Lett.* **2020**, *5*, 1186.
- [174] M. Li, F. Igbari, Z.-K. Wang, L.-S. Liao, *Adv. Energy Mater.* **2020**, *10*, 2000641.
- [175] F.-C. Chen, *Adv. Opt. Mater.* **2019**, *7*, 1800662.
- [176] W. Li, Q. Liu, Y. Zhang, C. a. Li, Z. He, W. C. H. Choy, P. J. Low, P. Sonar, A. K. K. Kyaw, *Adv. Mater.* **2020**, *32*, 2001591.
- [177] D. S. Hecht, L. Hu, G. Irvin, *Adv. Mater.* **2011**, *23*, 1482.
- [178] M. W. Rowell, M. A. Topinka, M. D. McGehee, H.-J. Prall, G. Dennler, N. S. Sariciftci, L. Hu, G. Gruner, *Appl. Phys. Lett.* **2006**, *88*, 233506.
- [179] X. Xia, S. Wang, Y. Jia, Z. Bian, D. Wu, L. Zhang, A. Cao, C. Huang, *J. Mater. Chem.* **2010**, *20*, 8478.
- [180] I. Jeon, C. Delacou, A. Kaskela, E. I. Kauppinen, S. Maruyama, Y. Matsuo, *Sci. Rep.* **2016**, *6*, 31348.
- [181] L. Yu, C. Shearer, J. Shapter, *Chem. Rev.* **2016**, *116*, 13413.
- [182] I. Jeon, C. Delacou, A. Kaskela, E. I. Kauppinen, S. Maruyama, Y. Matsuo, *Sci. Rep.* **2016**, *6*, 31348.
- [183] Y. Zhang, Z. Peng, C. Cai, Z. Liu, Y. Lin, W. Zheng, J. Yang, L. Hou, Y. Cao, *J. Mater. Chem. A* **2016**, *4*, 11821.



**Gururaj P. Kini** completed his B.Sc. (2006) and M.Sc. (2008) degree at Karnatak University, Dharwad, Karnataka, India. After working at a pharmaceutical company as a Research Associate during 2008–2012, he began his Ph.D. study at the University of Science and Technology, KRICT, Daejeon, Korea. He completed his Ph.D. in 2017 and then worked as a postdoctoral fellow at Konkuk University, Seoul, Korea (2017–2018). Now he is working as an Assistant professor at Konkuk University, Seoul, Korea (2018–present). His research interests include the design and synthesis of photoactive materials for organic electronics.



**Sung Jae Jeon** received his B.S. and Ph.D. degree from the Department of Materials and Chemistry Engineering, Konkuk University, Republic of Korea in 2013 and 2019. He worked as postdoctoral researcher at in the Nano & Information Materials Laboratory (NIMs), Department of Chemical Engineering, Konkuk University, Korea, under the supervision of Prof. Doo Kyung Moon (2019–2020). He is currently working as an assistant professor at Konkuk University (2020–present). His research focuses on designing and synthesizing conjugated materials for highly efficient organic electronics



**Doo Kyung Moon** received his Ph.D. from Tokyo Institute of Technology, Japan in 1993, and had post-doc experience at the University Arizona in USA (1993–1994) and the Korea Institute of Science and Technology (KIST, 1994–1995). Now, he is a professor of the Department of Chemical Engineering, Konkuk University, Republic of Korea. He was an adjunct professor of Advanced Industrial Science and Technology (AIST, 2009–2010). His research group works on the development of organic materials and organic electronic devices for organic solar cells, organic light emitting diodes and piezoelectric nanogenerators. For details please see the lab website: <http://nanoscience.or.kr>